論文 / 著書情報
Article / Book Information

題目(和文)	表面修飾ポリマー基板上におけるZnO薄膜の結晶成長と物性に関する研究
Title(English)	Study on crystal growth and properties of ZnO thin films on surface-modified polymer substrates
著者(和文)	大賀友瑛
Author(English)	Tomoaki Oga
出典(和文)	学位:博士(工学), 学位授与機関:東京工業大学, 報告番号:甲第12403号, 授与年月日:2023年3月26日, 学位の種別:課程博士, 審査員:吉本 護,舟窪 浩,真島 豊,和田 裕之,松田 晃史
Citation(English)	Degree:Doctor (Engineering), Conferring organization: Tokyo Institute of Technology, Report number:甲第12403号, Conferred date:2023/3/26, Degree Type:Course doctor, Examiner:,,,,
学位種別(和文)	博士論文
Type(English)	Doctoral Thesis

Doctoral Thesis

Study on crystal growth and properties of ZnO thin films on surface-modified polymer substrates

Department of Materials Science and Engineering

School of Materials and Chemical Technology

Tokyo Institute of Technology

Tomoaki Oga

March 2023

APPROVAL BY THESIS DIRECTOR

SUPERVISOR

Professor Mamoru Yoshimoto

CERTIFIED BY

Professor Hiroshi Funakubo

Professor Yutaka Majima

Associate Professor Hiroyuki Wada

Associate Professor Akifumi Matsuda

“Study on crystal growth and properties of ZnO thin films on surface-modified polymer substrates”

Tomoaki Oga

Contents

Accomplishment

Acknowledgments

Chapter 1
General introduction

1.1 Flexible electronic devices using polymer substrates

The development of science and technology has led to the use of advanced electronic devices in various fields of social life [1]. As typified by smartphones, we are now in an advanced information society in which a great deal of information is aggregated through the constant use of electronic devices by many people, and the optimum environment using this information is provided [2-4]. Flexible devices are actively being developed for further information and energy applications. Metal oxides, organic materials, carbon nanotubes (CNTs), and two-dimensional (2D) materials such as graphene and transition metal dichalcogenides (TMDs) are candidates for next-generation flexible device materials after amorphous silicon [5-7]. The characteristics of each material are as follows,

- Oxide semiconductors such as n-type ZnO and amorphous indium gallium zinc oxide (IGZO) have wide bandgap and show high performance with mobility of more than 10 $cm^2V^{-1}s^{-1}$, a high on/off ratio and stability. however, an optimal p-type oxide semiconductor has not yet been realized [8,9].
- Organic semiconductors are attractive because of their flexibility, relatively low process temperature, ease of deposition, and large area. Although remarkable progress has been made in recent years, there were reports that the mobility exceeded 1 $cm^2V^{-1}s^{-1}$, but compared to amorphous silicon and oxide, improvement is still desired in terms of performance [10,11].
- CNTs are cylindrical materials with a two-dimensional, six-membered ring network of carbon, and are excellent materials that provide excellent mechanical properties and high mobility [12,13].
- 2D materials, especially TMDs, exhibit metallic, semi-metallic, semiconducting, insulating, and superconducting based on their chemical composition and structural configuration, resulting in unique electrical and optical properties such as strong photoluminescence, high mobility, and on/off ratio. They also exhibit high resistance to mechanical deformation and flexibility. [14,15].

Among flexible device materials, metal oxide semiconductors are most promising as next-generation flexible device materials not only because of their high optical transparency, electron mobility, and excellent mechanical properties, but also because of

their cost, processability, and scalability, which are not inferior to those of organic materials [16-18].

Figure 1.1 shows typical flexible oxide electronics and their applications [19]. A variety of electronic devices are expected to become flexible, including solar cells, displays, and memory [20-23]. Sensors that grasp the movement of the shape are also fabricated via flexible devises. Especially in the medical field, the use of detailed and constant information will increasingly contribute to society. The development of wearable self-powered devices and timely sensors that can be operated in environments that conventional electronics cannot handle would be accelerated by the fabrication of flexible devices [24,25].

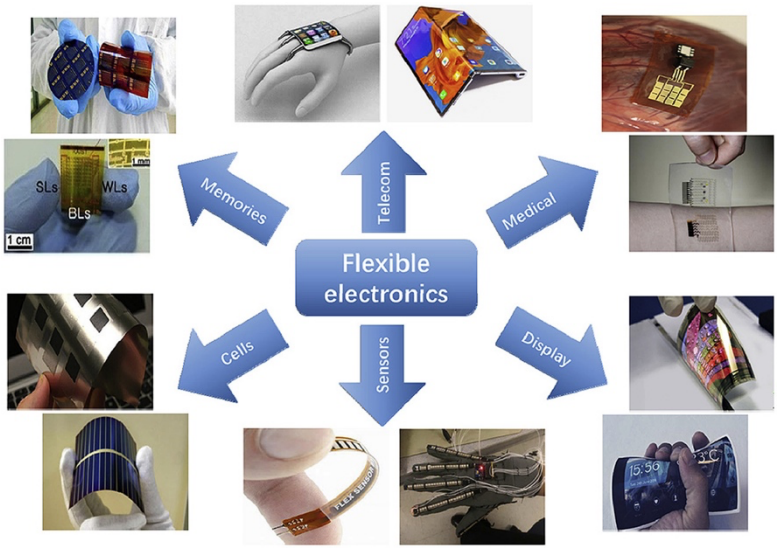

Figure 1.1 Typical flexible electronics and their applications [19].

Traditionally, inorganic material substrates such as silicon and glass have been exclusively used for such electronic devices, with crystalline oxide thin films being employed in terms of required characteristics and stability [26,27]. On the other hand, flexibility is strongly dependent on the substrate for flexible devices [28]. Ultra-thin glass, cleaved films of layered inorganic compounds such as a mica, metal foils, and polymer films are considered flexible as substrates [29-31]. Glass and single-crystal oxide films are able to be bent by making them ultra-thin and have advantage in term of the enough qualities and thermal stability in production process, but they are brittle and expensive to manufacture [32,33]. Metal foils have properties such as stability at relatively high temperatures, flexibility, and gas barrier properties. However, metal does not transmit

light, which may limit its applications [34]. Polymers are promising substrates for flexible devices because they are visible light transparent, lightweight, flexible, and robust [31,35]. They are also being actively used as an alternative to glass substrates. Therefore, polymeric materials are often suitable as substrates for flexible devices [36-38]. On the other hand, the variable surface roughness of the as-received polymer substrate before surface treatment would result in not enough performance and irregular crystal growth during thin film formation.

1.2 Surface modification of polymer substrates

Compared to ceramics and metal materials, polymer materials as electronic device substrates have the advantages of flexibility and light weight, but they also present stability issues [39-41]. In response, engineering polymers such as Polyimides (PI) and cyclo-olefin polymers (COP) have been developed to improve mechanical strength and chemical and heat resistance [42-44]. On the other hand, these highly stable polymer materials are designed to have low reactivity with surrounding materials as well as the surface, which is derived from van der Waals bonds between molecular chains [45,46]. Therefore, for device applications, it is necessary to impart different properties only to the surface while maintaining the bulk properties [47-49].

Physical and chemical surface treatment are used to form new functions to polymer materials shown in Figure 1.2 [50,51].

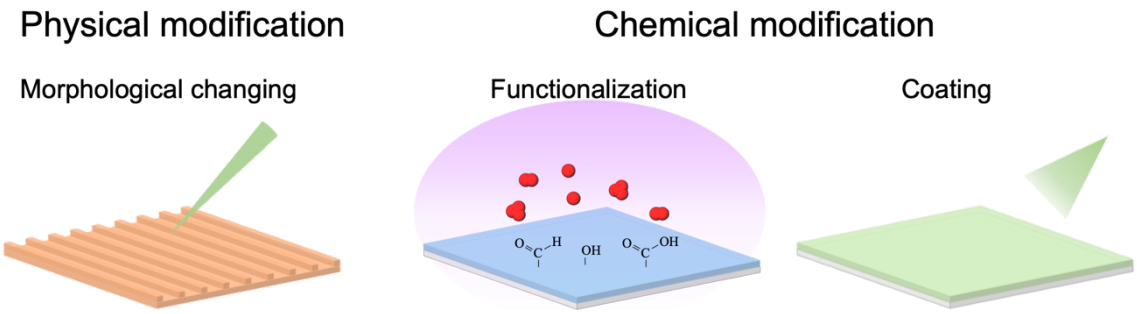

Figure 1.2. Schematic diagram of physical and chemical modification onto polymer surface.

Physical surface modification is a method of modifying a surface by changing its morphology without changing its chemical composition and is performed with electron beam and nanoimprint lithography techniques [52,53]. The formation of pattern at the nano- and sub-nano-level not only has a structural impact on physical properties but can also induce a specific ordered structure in the material, allowing for dominant crystal growth [54-56]. From the viewpoint of crystal growth, the increase in specific surface area due to substrate patterning increases surface free energy and nucleation sites. On the other hand, a flat surface improves orientation by promoting uniform crystal growth [57].

Chemical surface modification is a method of modifying a surface by introducing elements that differ from the original chemical composition. The chemical state of the polymer surface is modified by forming functional groups on the polymer surface through oxidation treatments such as solution, plasma, corona discharge, and ultraviolet

irradiation, or by coating the polymer surface with a film having a different function through vapor deposition, casting, or plasma polymerization. [58-62]. They are often used because they are more effective than physical modification. Many of them also involve effects where the morphology of the surface is simultaneously modified [63,64].

Surface modification is also used to advance the crystal growth of oxide thin films on polymer substrates. Table 1.1 shows the polymer substrate surface modifications that have an effect on the crystal growth of ZnO thin films [65-74]. There are two main approaches to modifying substrate surfaces: the first is to directly modify the morphology and chemical state of the polymer substrate; the second is to coat the substrate surface with a so-called buffer layer or seed layer. Direct modification of polymer substrates involves the addition of polar functional groups to the surface of the polymer substrate to improve adhesion and nucleation site of oxide thin film and the associated changing of the surface morphology. Most of the reports use plasma treatment, which increases surface roughness at the same time. Polymer surfaces with increased surface energy and surface area are expected to improve the crystallinity or crystallite size of ZnO thin films. On the other hand, few studies have attempted to control the nucleation and orientation of oxide thin films by modifying only the surface morphology of the polymer substrate. In the technique of coating on polymer substrates, weather-resistant oxide thin films such as silica and alumina are mainly prepared. Oxides have a large surface free energy relative to polymer materials and are expected not only to nucleate the target thin film and improve adhesion, but also to serve as a protective layer against inter-diffusion and plasma damage during thin film formation [72,73]. It has been reported that surface modification with amorphous oxide buffer films improves the crystallinity of ZnO thin films. In addition to that, when an oriented oxide films were prepared as a buffer, not only the crystallinity but also the orientation of the ZnO thin film was controlled [74].

Table 1.1 Polymer substrate surface modifications that have an effect on the crystal growth of ZnO thin films.

Treatment	Changes to polymers	Effects on films	Ref.
O_2 plasma	Increase surface roughness Decrease contact angle	Crystallinity	[65]
O_2 plasma	Increase surface roughness	Crystallinity	[66]
O_2 plasma	Increase surface roughness Decrease contact angle	Mobility	[67]
O_2 plasma	Decrease contact angle	Crystallinity	[68]
Ar plasma	Improvement of the crystallinity Increase the surface energy	Crystallinity	[69]
Corona discharge	Decrease contact angle	-	[70]
UV/ Self-assembled monolayers	Surface dipole modulation to electron donating group	Crystallinity	[71]
Al_2O_3 buffer	Formation of Al_2O_3 buffer layer	Crystallinity	[72]
SiO_2 buffer	Formation of SiO_2 buffer	Crystallinity	[73]
2D nanosheet coating	Introduction of buffer or seed layers such as single crystal sheets	Crystallinity Orientation	[74]

1.3. Crystal growth of oxide thin films on polymer substrate

The growth modes of thin films are understood as the Frank-van der Merwe (FM) mode, which is a layered two-dimensional growth, the Stranski-Krastanov (SK) mode, which is an island-like three-dimensional growth after two-dimensional growth, and the Volmer-Weber (VW) mode, which is an island-like three-dimensional growth from the beginning, based on the relative surface energies before and after the growth [75,76]. That is, when the surface free energy formed by the adatoms is larger than the original surface free energy of the substrate, the growth proceeds as an island-like VW-mode.

On the other hand, it has been suggested that the structure of a sputtered film can be understood in terms of the melting point and the temperature at which the thin film is formed [77,78]. Growth on oxide substrates deposited at high temperatures results in the growth of columnar grains over the full thickness of the growing thin film due to migration and recrystallization of grain boundaries with high adatom mobility at the surface, whereas polymer substrates have limited deposition temperatures, resulting in low adatom mobility at the surface and the initial nuclei are likely to be a dense array of tapered crystals or fibrous grains that have grown in the direction of the available precursor and have begun to self-diffuse slightly [77].

Regarding the temperature dependence of nucleation density and crystal growth rate, it is known that nucleation is more dominant at low temperatures. Since surface migration is suppressed in growth near room temperature where the deposition temperature is limited, it is expected that many crystal nuclei are generated on the substrate and the crystal grain size becomes smaller. Thus, crystal growth of oxide thin films is not enough on polymer substrates. Even in case of ITO thin film, which is promising as a transparent conducting film, requires thermal treatment at approximately 200°C or higher for sufficient crystallization to obtain low resistivity [79]. Figure 1.3 shows the Crystal growth of oxide thin films grown on a polymer substrate [80,81]. Because of the limited growth temperatures on polymer substrates, the thin films are often amorphous or polycrystalline with small grain size and non-orientation, especially in the initial stages [73,80].

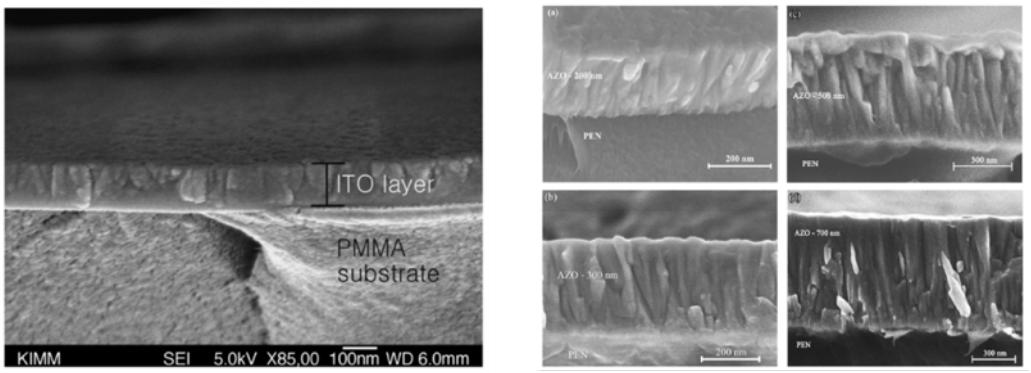

Figure 1.3 Crystal growth of oxide thin films grown on a polymer substrate [80,81].

During the nucleation and crystal growth process of ZnO thin films, many studies have reported that the ZnO thin films often grow in a self-oriented crystal growth. While these phenomena have been attributed to several stochastic processes acting during the nucleation and growth stages to dictate the final orientation of the ZnO thin film, the most commonly used explanation for this is surface energy minimization [82]. This involves the preferential nucleation on the substrate of initial nuclei with a particular crystallographic orientation perpendicular to the substrate and a process whereby particles with the fastest growth rate perpendicular to the substrate envelop other particles and ultimately dominate the film [83]. Several studies have reported that dense nucleation promotes grain growth along planes with the lowest surface energy and improves crystallinity by growing equiaxed columnar grains from the interface [84]. The crystallinity of the ZnO thin film on the polymer substrate also depends on the film thickness [85]. In order to grow high-quality oxide thin films, it is necessary to improve the crystallinity and orientation, especially at the nucleation and initial stage of crystal growth.

1.4 Crystal growth of ZnO thin films on various substrates

Zinc oxide (ZnO) has a predominantly hexagonal wurtzite-type crystal structure as shown in Figure 1.4 [86]. The lattice parameter is a= b= 0.32 nm and c = 0.52 nm, with Zn at the center and O around it in a tetrahedrally coordinated unit [87,88]. The upper and lower planes are not equivalent, and there are Zn-face (+c) and O- (-c) face shown in figure 1.4 [89].

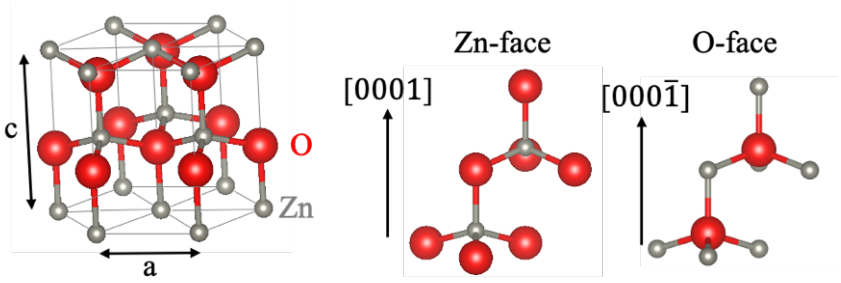

Figure 1.4 Crystal structure and polar surface of wurtzite-type ZnO.

ZnO is a direct transition semiconductor with a band gap of about 3.37 eV. In ZnO, the valence band (V.B.) consists mainly of oxygen 2p orbitals and the conduction (C.B.) band consists mainly of Zn 4s orbitals [90]. Intercalation Zn and oxygen defects are mainly donor defects, which are considered to be donors that provide electrons to the conduction band due to their low ionization energy. It also has a high exciton binding energy of about 60 meV [91,92]. These characteristics make it an attractive material for many applications, especially thin-film transistors, transparent conducting films, ultraviolet light devices such as lasers and LEDs, and piezoelectric devices as shown in Figure 1.5 [93-96].

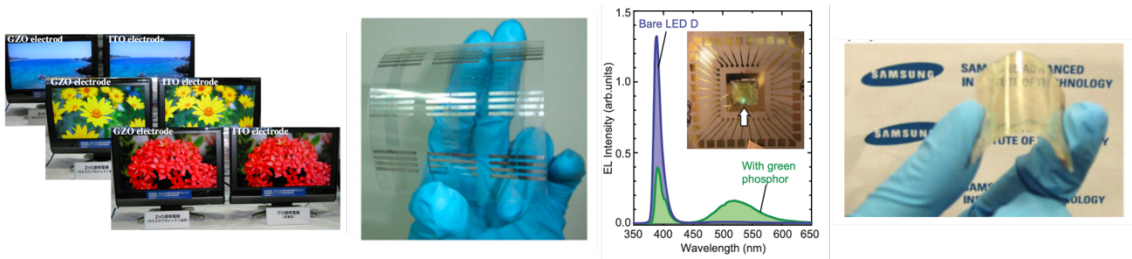

Figure 1.5 Various applications using ZnO thin films [93-96].

Crystalline ZnO thin films have been reported to have been prepared by various deposition techniques such as sputtering, chemical vapor deposition, solution method, and molecular beam epitaxy [97-102]. In particular, ZnO thin films prepared in a vacuum atmosphere are n-type semiconductors with a degenerate carrier density in the range of 10^{20}-10^{21} cm^{-3} due to donors and impurity dopants such as Al and Ga resulting from oxygen depletion [103,104]. Table 1.2 shows previously reported crystal growth and electrical properties of pure, and impurity doped ZnO films ZnO thin films prepared by various techniques [105-121]. ZnO thin films have been prepared on substrates of many materials, including polymer substrates as well as oxide substrates, because of their excellent properties and relatively easy formation of crystalline layers. High quality ZnO thin films were prepared by epitaxial growth on single crystal substrates such as sapphire, and regardless of the method, the rocking curve was obtained less than 0.1 degree. The impurity doped ZnO films had carrier concentrations above 10^{21} and mobility about 40, resulting in resistivity in the 10^{-5} range. These were quite excellent values for an oxide transparent conducting film, and demonstrated to be comparable to ITO thin films. The growth on ZnO thin films was c-axis orientation even on amorphous glass substrates, resulting in highly crystalline and oriented ZnO thin films were fabricated at particularly high temperatures.

However, compared to epitaxially grown ZnO thin films, the orientation of self-oriented ZnO thin films was lower. The crystallinity was also lower for the as well. Nevertheless, a carrier concentration of about 1.54×10^{21}, a mobility of 47.6, and a resistivity in the 10^{-5} range were achieved for the Al-doped ZnO thin film, indicating that ZnO thin films on glass substrates have good potential as transparent conducting films.

Although crystal growth of ZnO thin films on polymer substrates is limited by deposition temperature, it has been reported that ZnO thin films on polymer substrates were also crystallized and showed oriented growth, similar to films on glass substrates. Nevertheless, their quality was still somewhat unsatisfactory compared to that on oxide substrates. There are few studies on degree of c-axis orientation of ZnO thin films on amorphous substrates, the results of XRD rocking-curves suggest that orientation growth is disrupted in crystal growth. The FWHM value in $2\theta/\theta$-scans also increased 3-times, was suggesting that only a third of the crystallite size was achieved in terms of estimation of by Scherrer's formula [122]. Usually, although electrical properties are often estimated the carrier transport in parallel to the film surface and crystallite size is estimated in perpendicular to the film surface, it is thought that the crystallite size estimated in the direction perpendicular to the film surface is correlated with the crystallite size in the direction parallel to the film surface, resulting that the crystallite size and Hall mobility

are closely related [103]. Thus, ZnO thin films fabricated on polymer substrates show a decrease in mobility, probably due to grain boundary scattering caused by crystallinity degradation. The lowest range of reported resistivity is 2-3 × 10^{-4}, which is high compared to films on single crystal and oxide glass substrates, which are grown at high temperatures. Fabrication of ZnO thin films with crystalline growth on polymer substrates at the same level as on oxide substrates leads to further development of flexible devices. Thus, it is necessary to develop deposition techniques that improve the crystallinity and orientation of ZnO films on polymer substrates at low temperatures.

Table 1.2 shows the results of XRD measurement and electrical properties of ZnO thin films prepared on various substrates.

Method	Film	Substrate	Rocking-curve FWHM [º]	2θ/θ FWHM [º]	Resistivity [Ωcm]	Carrier concentration [cm^{-3}]	Mobility [$cm^2V^{-1}s^{-1}$]	Ref.
rf-magnetron sputtering	ZnO	α-Al_2O_3	0.078	-	-	-	-	[105]
CVD	ZnO	YSZ	0.0367	-	-	-	20-25	[106]
PLD	ZnO	α-Al_2O_3	0.042	0.011	-	-	74	[107]
PLD	GZO	α-Al_2O_3	-	-	5.1×10^{-5}	2.8×10^{21}	41.9	[108]
PLD	AZO/GZO	α-Al_2O_3	-	-	8.4×10^{-5}	1.6×10^{21}	45	[109]
PLD	ZnO	Glass	1.23	0.110	-	-	-	[110]
rf-magnetron sputtering	ZnO	Glass	-	0.23	0.5	1.7×10^{20}	1.0	[111]
rf-magnetron sputtering	ZnO	Glass	4.0	0.346	10^9-10^{10}	-	-	[112]
CVD	ZnO	Glass	-	0.205	-	2×10^{19}	68	[113]
PLD	AZO	Glass	-	0.344	8.54×10^{-5}	1.54×10^{21}	47.6	[114]
Pulsed-DC sputtering	AZO	Glass	-	-	1.7×10^{-4}	1.2×10^{21}	40	[115]
Ion-plating	GZO	Glass	-	0.16	2.1×10^{-4}	1.1×10^{21}	27.6	[116]
CVD	ZnO	PI	-	0.339	-	-	-	[117]
CAPD	ZnO	PI	-	0.343	6.68×10^{-3}	1.32×10^{20}	11.24	[118]
PLD	ZnO	COP	-	0.38	1.5×10^{2}	-	-	[119]
PLD	ZnO	Nanosheet PEN	4.92 20.79	-	3×10^{-2}	-	-	[74]
rf-magnetron sputtering	GZO	PES	-	0.3797	2.3×10^{-4}	3.39×10^{21}	7.97	[120]
PLD	AZO	PES	-	-	2.349×10^{-4}	-	17.18	[67]
Ion-plating	GZO	COP	-	0.37	5.9×10^{-4}	-	-	[121]

Scattering mechanisms in degenerate semiconductors such as tin-doped indium oxide (ITO) and impurity-doped ZnO films have been investigated to realize transparent conducting films with low resistivity [123]. In ZnO thin films with carrier concentrations on the order of 10^{20}-10^{21} cm^{-3}, Hall mobility is thought to be dominated primarily by ionized impurity scattering [103]. Minami et al. report that the relationship between Hall

mobility and carrier concentration experimental results for ZnO films with carrier concentrations on the order of 10^{19}-10^{21}cm^{-3} prepared using various deposition methods can be explained by combining Brooks-Herring-Dingle (B-H-D) theory and mobility dominated by ionized impurity scattering modified by considering conduction band degeneracy and nonparabolicity, and mobility dominated by grain boundary scattering given by Seto [124,125]. It is also known that in polycrystalline ZnO films, the Hall mobility is strongly affected by the crystallinity of the films. An understanding of these scattering mechanisms is necessary for the preparation of low-resistivity ZnO thin films.

1.5 Objective of this study

The combination of polymer substrates and oxide thin films is expected to be applied to flexible and wearable devices because of the electrical and optical properties based on the crystal structure of oxides and the light weight and flexibility of polymer substrates. In particular, ZnO thin films are promising materials in many fields because of their electrical and optical properties.

In general, crystal-oriented growth is important for to formation devices using oxide semiconductors including ZnO thin films, to control the physical properties, and they have been fabricated at high temperature on single-crystal or oxide glass substrates. Low-temperature nucleation and growth orientation control techniques are required to realize such highly crystalline and oriented thin films on polymer substrates with low thermal stability that exhibit glass transition at relatively low temperatures. The use of surface-modified polymer substrates and oxide buffer layers have been investigated in this regard, but not much is known about the effect of the surface morphology and chemical state of the polymer substrate surface on the crystal growth of ZnO thin films. There are also few studies on the effect of surface modification on mosaicity of crystal growth and properties, especially on modified polymer substrates surfaces.

The object of this Dr thesis study is to clarify the effect of physical and chemical surface modification of polymer substrates on the crystal growth of ZnO thin films on polymer substrates, which affects the crystallinity and orientation, and to verify the surface modifying conditions for the preparation of highly crystalline and oriented ZnO thin films to achieve high electrical and optical properties. The control of crystal growth of ZnO thin films grown by room temperature pulsed laser deposition using morphological and chemical surface pretreatment as a modification of polymer surfaces was investigated. In addition, crystal growth of ZnO thin films on polymer substrates pretreated with a combination of physical and chemical surface modification techniques was clarified, and methods for fabricating high-quality ZnO thin films on composite surface-modified polymer substrates were discussed.

This thesis consists of seven chapters, including a general introduction and individual chapters.

In Chapter 1, the background and objective of this thesis were described in the general introduction. In particular, materials for flexible devices, the effect of surface modification of polymer substrates, crystal growth of oxide thin films on polymer substrates, and previous studies of ZnO thin films on various substrates are mentioned.

In Chapter 2, the basic surface modification and thin film deposition and analysis techniques used in this study are presented.

In Chapter 3, the crystal growth, and properties of ZnO thin films on ultra-flat polymer substrate surfaces with atomic-step pattern prepared by thermal nanoimprinting were discussed.

In Chapter 4, the surface morphology and chemical state of polymer substrates were modified by vacuum ultraviolet light irradiation, and the crystal growth and properties of ZnO thin films on those substrates were discussed.

In Chapter 5, the growth, and properties of ZnO thin films on oxide buffer layers with various crystal structures and crystallinity were investigated.

In Chapter 6, the crystal growth and properties of ZnO thin films grown on surface modified COP substrates with a combination of physical and chemical surface modification was investigated. The combination of surface modification techniques was performed by thermal nanoimprinting and oxide buffer insertion. Impurity-doped ZnO thin films on surface modified polymer substrates were also investigated for the producing highly conductive ZnO thin films using these techniques.

In Chapter 7, general conclusions, and a summary of the results obtained in this study are mentioned.

Reference

[1] J. Wu, S. Guo, H. Huang, IEEE Commun. Surv. Tutor., 20 (2018) 2389–2406.

[2] R.K. Ganti, F. Ye, H. Lei, IEEE Commun. Mag., 49 (2001) 32–39.

[3] E. Borgi, Comput. Commun., 54 (2014) 1–31.

[4] D. boyd, K. Crawford, Inf. Commun. Soc., 15 (2011) 662–67.

[5] X. Wang, X. Lu, B. Liu, D. Chen, Y. Tong, G. Shen, Adv.Mater., 26, (2014) 4763–478.

[6] X. Wang, Z. Liu, T. Zhang, Small, 13, 1602790 (2017).

[7] A. Nathan, A. Ahnood, M.T. Cole, S. Lee, Y. Suzuki, P. Hiralal, F. Bonaccorso, T. Hasan, L. Garcia-Gancedo, A. Dyadyusha, S. Haque, P. Andrew, S. Hofmann, J. Moultrie, D. Chu, A.J. Flewitt, A.C. Ferrari, M.J. Kelly, J. Robertson, G.A.J. Amaratunga, W.I. Milne, Proc. IEEE Inst. Electr. Electron. Eng., 100 (2012) 1486 –1517.

[8] L. Petti, N. Münzenrieder, C. Vogt, H. Faber, L. Büthe, G. Cantarella, F. Bottacchi, T. D. Anthopoulos, G. Tröster, Appl. Phys. Rev., 3, 021303 (2016).

[9] K. Nomura, H. Ohta, A. Takagi, T. Kamiya, M. Hirano, H. Hosono, Nature volume 432 (2004) 488–492.

[10] A.A. Virkar, S. Mannsfeld, Z. Bao, N. Stingelin, Adv.Mater., 22 (2010), 3857–387.

[11] S.E. Root, S. Savagatrup, A.D. Printz, D. Rodriquez, Chem. Rev., 117 (2017) 6467–6499.

[12] H. Zhu, E.-S. Shin, A. Liu, D. Ji, Y. Xu, Y.-Y. Noh, Adv. Funct. Mater., 30, 1904588 (2020).

[13] S. Park, M. Vosguerichian, Z. Bao, Nanoscale, 5 (2013) 1727–1752.

[14] D. Jariwala, V.K. Sangwan, L.J. Lauhon, T.J. Marks, M.C. Hersam, ACS nano, 8 (2014) 1102–1120.

[15] W. Choi, N. Choudhary, G.H. Han, J. Park, D. Akinwande, Y.H. Lee, Mater. Today, 20, 3 (2017).

[16] H. Hosono, J. Non. Cryst. Solids, 352 (2006) 851–858.

[17] J.K. Jeong, Semicond. Sci. Technol. 26, 034008 (2011).

[18] G. Cantarella, J. Costa, T. Meister, K. Ishida, C. Carta, F. Ellinger, P. Lugli, N. Münzenrieder, L. Petti, Flex. Print. Electron. 5, 033001 (2020).

[19] W. Gao, Y. Zhu, Y. Wang, G. Yuan, J.-M. Liu, J. Materiomics, 6 (2020) 1–16.

[20] Y.-H. Kim, J.-S. Heo, T.-H. Kim, S. Park, M.-H. Y, J. Kim, M.S. Oh, G.-R. Yi, Y.-Y. Noh, S.K. Park, nature, 489 (2012) 128–132.

[21] M. Abdelfatah, J. Ledig, A. El-Shaer, A. Wagner, A. Sharafeev, P. Lemmens, M.M.

Mosaad, A. Waag, A. Bakin, Sol. Energy 122 (2015) 1193–1198.
[22] J.K. Jeong, Semicond. Sci. Technol. 26, 034008 (2011).
[23] S. Kim, H. Moon, D. Gupta, S. Yoo, Y.-K. Choi, IEEE Electron Device Lett., 56 (2009) 696–699.
[24] B. Wang, A. Thukral, Z. Xie, L. Liu, X. Zhang, W. Huang, X. Yu, C. Yu, T.J. Marks, A. Facchetti, Adv. Funct. Mater., 30, 1907437 (2020).
[25] J.H. Lee, S.P. Park, K. Park, H.J. Kim, Adv. Funct. Mater., 30, 1907437 (2020).
[26] L. Liu, J.H. Edgar, Mater. Sci. Eng. R, 37 (2002) 61–127.
[27] J.H. Choi, A. Zoulkarneev, S.Il Kim, C.W. Baik, M.H. Yang, S.S. Park, H. Suh, U. Kim, H.B. Son, J.S. Lee, M. Kim, J.M. Kim, K. Kim, Nat. Photonics, 5, (2011) 763–769.
[28] W.A. MacDonald, M.K. Looney, D. MacKerron, R. Eveson, R. Adam, K. Hashimoto, K. Rakos, J. Soc. Inf. Disp., 15 (2007) 1075–1083.
[29] V. Zardetto, T.M. Brown, A. Reale, A.D. Carlo, J. Polym. Sci. B Polym. Phys., 49 (2011) 638–648.
[30] J.H. Souk, W. Lee, J. Soc. Inf. Disp., 18 (2010) 258–265.
[31] G.Zhong, J. Li, J. Materiomics., 6 (2020) 455–457.
[32] M.D.J. Aucha, O.K. Soob, G. Ewaldb, C. Soo-Jina, Thin Solid Films, 417 (2002) 47–50.
[33] S. Park, H. Park, S. Seong, Y. Chung, Sci. Rep., 10, 7660 (2020).
[34] J.-S. Park, H. Chae, H.K. Chung, S.I. Lee, Semicond. Sci. Technol. 26, 034001 (2011).
[35] X. Fanga, T. Maa, M. Akiyama, G. Guan, S. Tsunematsu, E. Abe, Thin Solid Films 472 (2005) 242–245.
[36] Y.S. Rim, S.-H. Bae, H. Chen, N.D. Marco, Y. Yang, Adv. Mater., 28 (2016) 4415–4440.
[37] J.S. Lewis, M.S. Weaver, IEEE J. Sel. Top. Quantum Electron., 10 (2004) 45–57.
[38] M. Kaltenbrunner, M.S. White, E.D. Głowacki, T. Sekitani, T. Someya, N. Serdar sariciftci, S. Bauer, Nat. Commun., 3, 770 (2012).
[39] M.-C. Choi, Y. Kim, C. -S. Ha, Prog. Polym. Sci. 33 (2008) 581–630.
[40] V. Zardetto, T, M. Brown, A. Reale, A. D. Carlo, J. Polym. Sci. B Polym. Phys., 49, (2011) 638–648.
[41] C. Pang, C. Lee, K.-Y. Suh, J. Appl. Polym. Sci., 130, (2013) 1429–1441.
[42] M. Yamazaki, J. Mol. Catal. A Chem., 213, (2004) 81–87.
[43] C. E. Sroog, Prog. Polym. Sci., 16, (1991) 561–694.
[44] W. A. MacDonald, J. Mater. Chem., 14, (2004) 4–10.

[45] P. S. Nunes, P. D. Ohlsson, O. Ordeig, J.P. Kutter, Microfluid Nanofluid, 9 (2010) 145–161.
[46] S. Feng, Z. Zhong, Y. Wang, W. Xing, E. Drioli, J. Membr. Sci., 549, (2018) 332–349.
[47] C.-M. Chan, T.-M. Ko, H. Hiraoka, Surf. Sci. Rep., 24 (1996) 1–54.
[48] J.M. Goddard, J.H. Hotchkiss, Prog. Polym. Sci. 32 (2007) 698–725.
[49] P.K. Chu, J.Y. Chen, L.P Wang, N Huang, Mater. Sci. Eng. R, 36 (2002) 143–206.
[50] S.K. Nemani, R.K. Annavarapu, B. Mohammadian, A. Raiyan, J. Heil, M.A. Haque, A. Abdelaal, H. Sojoudi, Adv. Mater. Interfaces, 5, 1801247, (2018).
[51] E.M. Liston, L. Martinu, M.R. Wertheimer, J. Adhesion Sci. Technol., 7, (1993) 1091–1127.
[52] S. Aksu, M. Huang, A. Artar, A.A. Yanik, S. Selvarasah, M.R. Dokmeci, H. Altug, Adv. Mater., 23, (2011) 4422–4430.
[53] H.-J. Choi, S. Choo, J.-H. Shin, K.-I. Kim, H. Lee, J. Phys. Chem. C, 117 (2013) 24354–24359.
[54] E.I. Givargizov, J. Cryst. Growth, 310 (2008) 1686–1690.
[55] S. Ikeda, K. Saiki, Appl. Phys. Lett. 88, 251905 (2006).
[56] A. Ismach, D. Kantorovich, E. Joselevich, J. Am. Chem. Soc., 127, 11554 (2005).
[57] Y. Akita, Y. Miyake, H. Nakai, H. Oi, M. Mita, S. Kaneko, M. Mitsuhashi, M. Yoshimoto, Appl. Phys. Express, 4, 035201 (2011).
[58] G.J. Ross, J.F. Watts, M.P. Hill, P. Morrissey, Polymer 41 (2000) 1685–1696.
[59] N. Inagaki, S. Tasaka, K. Hibi, J. Polym. Sci. A Polym. Chem., 30, (1992) 1425–1431.
[60] Y.-J. Kim, Y. Taniguchi, K. Murase, Y. Taguchi, H. Sugimura, Appl. Surf. Sci., 255 (2009) 3648–3654.
[61] A.u. Haq, A. Boyd, J. Acheson, J. McLaughlin, B.J. Meenan, Surf. Coat. Technol., 362 (2019) 185–190
[62] Y. Ikada, Biomater., 15(1994) 725–736.
[63] A. Vesel, I. Junkar, U. Cvelbar, J. Kovac, M. Mozetic, Surf. Interface Anal., 40 (2008) 1444–1453.
[64] T. N Murakami, Y. Fukushima, Y. Hirano, Y. Tokuoka, M. Takahashi, N. Kawashima., Colloids Surf. B, 29 (2003) 171–179.
[65] B.G. Kim, J.Y., Kim, S.J. Lee, J.H. Park, D.G. Lim, M.G. Park, Appl. Surf. Sci., 257 (2010) 1063–1067.
[66] J.H. Heo, H. Ryu, W.J Lee, J. Ind. Eng. Chem., 19 (2013) 1638–1641.
[67] J. P. Kim, S. A. Lee, J. S. Bae, S. K. Park, U. C. Choi, C. R. Cho, Thin Solid Films,

516 (2008) 5223–5226.
[68] C. C. Chen, F. H. Wang, S. C. Chang, C. F. Yang, Materials, 11, 1501 (2018).
[69] S. Fernández, J. D. Santos, C. Munuera, M. G. Hernández, F. B. Naranjo, Sol. Energy Mater Sol. Cells, 133 (2015) 170–179.
[70] C.Y. Tsay, K.C. Pai, Thin Solid Films, 654, (2018) 11–15.
[71] T.T.T. Vo, K.P.O. Mahesh, P. H. Lin, Y. Tai, Appl. Surf. Sci., 403 (2017) 356–361.
[72] Z.L. Pei, X.B. Zhang, G.P. Zhang, J. Gong, C. Sun, R.F. Huang, L.S. Wen, Thin Solid Films, 497 (2006) 20–23.
[73] E. Fortunato, A. Gonçalves, V. Assunção, A. Marques, H. Águas, L. Pereira, I. Ferreira, R. Martins, Thin Solid Films, 442 (2003) 121–126.
[74] T. Shibata, T. Ohnishi I. Sakaguchi, M. Osada, K. Takada, T. Kogure, T. Sasaki, J. Phys. Chem. C, 113 (2009) 19096–19101.
[75] J.A. Venables, Surf. Sci., 1 (1994) 798-817.
[76] M. Copel, M.C. Reuter, E. Kaxiras, R.M. Tromp, Phys. Rev. Lett., 63 (1989) 632–635.
[77] J.A. Thornton, J. Vac. Sci. Technol., 11 (1974) 666–670.
[78] O. Kluth, G. Schöpe, J. Hüpkes, C. Agashe, J. Müller, B. Rech, Thin Solid Films 442 (2003) 80–85.
[79] U. Betz, M.K. Olsson, J. Marthy, M.F. Escolá, F. Atamny, Surf. Coat. Technol., 200 (2006) 5751–5759.
[80] D.-H. Kim, M.-R. Park, H.-J. Lee, G.-H. Lee, Appl. Surf. Sci., 253 (2006) 409–411.
[81] S. Hamrit, K. Djessas, N. Brihi, B. Viallet, K. Medjnoun, S.E. Grillo, Ceram. Int., 42 (2016) 16212–16219.
[82] J.R.R. Bortoleto, M. Chaves, A.M. Rosa, E.P. da Silva, S.F. Durrant, L.D. Trino, P.N. Lisboa-Filho, Appl. Surf. Sci., 334 (2015) 210–215.
[83] Y. Kajikawa, J. Cryst. Growth, 289 (2006) 387–394.
[84] T. Yamada, A. Miyake, S. Kishimoto, H. Makino, N. Yamamoto, T. Yamamoto, Appl. Phys. Lett. 91, 051915 (2007).
[85] K.-H. Bang, D.-K. Hwang, J-M. Myoung, Appl. Surf. Sci., 207 (2003) 359–364.
[86] A. Janotti, C.G.V.d. Walle, Rep. Prog. Phys., 72, 126501 (2009).
[87] Ü. Özgür, Y.I. Alivov, C. Liu, A. Teke, M.A. Reshchikov, S. Doğan,c V. Avrutin, S.-J. Cho, H. Morkoçd, J. Appl. Phys., 98, 041301 (2005).
[88] A.D. Corso, M. Posternak, R. Resta, A. Baldereschi, Phys. Rev. B, 50, 10715 (1994).
[89] G. Heiland, P. Kunstmann, Surf. Sci., 13, (1969) 72–84.
[90] P.S. Xu, Y.M. Sun, C.S. Shi, F.Q. Xu, H.B. Pan, Nucl. Instr. and Meth. in Phys. Res. B, 199 (2003) 286–290.

[91] L. Schmidt-Mende, J.L. MacManus-Driscoll, Mater. Today, (2007) 40–48.
[92] D.C. Look, Mater. Sci. Eng., B80 (2001) 383–387.
[93] N. Yamamoto, H. Makino, S. Osone, A. Ujihara, T. Ito, H. Hokari, T. Maruyama, T. Yamamoto, Thin Solid Films, 520 (2012) 4131–4138.
[94] C.Y. Lee, M.Y. Lin, W.H. Wu, J.Y. Wang, Y. Chou, W.F. Su, Y.F. Chen, C.F. Lin, Semicond. Sci. Technol. 25, 105008 (2010).
[95] K. Nakahara, S. Akasaka, H. Yuji, K. Tamura, T. Fujii, Y. Nishimoto, D. Takamizu, A. Sasaki, T. Tanabe, H. Takasu, H. Amaike, T. Onuma, S. F. Chichibu, A. Tsukazaki, A. Ohtomo, and M. Kawasaki, Appl. Phys. Lett., 97, 013501 (2010).
[96] M.-Y. Choi, D. Choi, M.-J Jin, I. Kim, S.-H. Kim, J.-Y. Choi, S.Y. Lee, J.M. Kim, S.-W. Kim, Adv. Mater., 21 (2009) 2185–2189.
[97] J. Mass, P. Bhattacharya, R.S. Katiyar, Mater. Sci. Eng. B, 103 (2003) 9–15.
[98] P. F. Carcia, R.S. McLean, M.H. Reilly, G. Nunes, Jr., Appl. Phys. Lett., 82 (2003) 117–119.
[99] M. Puricaa, E. Budianua, E. Rusub, M. Danilaa, R. Gavrilaa, Thin Solid Films, 403–404 (2002) 485–488.
[100] Y. W. Heo, D. P. Norton, S. J. Pearton, J. Appl. Phys., 98, 073502 (2005).
[101] L. Znaidi, Mater. Sci. Eng. B, 174 (2010) 18–30.
[102] K. Iwataa, T. Sakemi, A. Yamada, P. Fons, K. Awai, T. Yamamoto, M. Matsubara, H. Tampo, S. Niki, Thin Solid Films, 445 (2003) 274–277.
[103] T. Minami, Semicond. Sci. Technol., 20 (2005) S35–S44.
[104] Ü. Özgür, D. Hofstetter, Hadis Morkoç, Proc. IEEE Inst. Electr. Electron. Eng., 98 (2010) 1255–1268.
[105] Il-S. Kim, S.-H. Jeong, S.S. Kim, B.-T. Lee, Semicond. Sci. Technol., 19 (2004) L29–L31.
[106] Y.-C. Chao, C.-W. Lin, D.-J. Ke, Y.-H. Wu, H.-G. Chen, L. Chang, Y.-T. Ho, M.-H. Liang, J. Cryst. Growth, 298 (2007) 461–463.
[107] E.M. Kaidashev, M. Lorenz, H. von Wenckstern, A. Rahm, H.-C. Semmelhack, K.-H. Han, G. Benndorf, C. Bundesmann, H. Hochmuth, M. Grundmann, Appl. Phys. Lett., 82, 3901 (2003).
[108] R.S. Ajimsha, A.K. Das, P. Misra, M.P. Joshi, L.M. Kukreja, R. Kumar, T.K. Sharma, S.M. Oak, J. Alloys Compd., 638 (2015) 55–58.
[109] Z. Zhang, C. Bao, S. Ma, S. Hou, Appl. Surf. Sci., 257 (2011) 7893–7899.
[110] S.L. King, J.G.E. Gardeniers, I.W. Boyd, Appl. Surf. Sci., 96-98 (1996) 811–818.
[111] S. Cho, Trans. Electr. Electron. Mater., 10 (2009) 185–188.
[112] Y. Yoshino, K. Inoue, M. Takeuchi, K. Ohwada, Vacuum, 51 (1998) 601–607.

[113] K.T. Roro, J.K. Dangbegnon, S. Sivaraya, A.W.R. Leitch, J.R. Botha, J. Appl. Phys. 103, 053516 (2008).
[114] H. Agura, A. Suzuki, T. Matsushita, T. Aoki, M. Okuda, Thin Solid Films 445 (2003) 263–267.
[115] B.K. Sarma, P. Rajkumar, Mater. Today Commun., 23, 100870 (2020).
[116] T. Yamada, A. Miyake, S. Kishimoto, H. Makino, N. Yamamoto, T. Yamamoto, Surf. Coat. Technol., 202 (2007) 973–976.
[117] M. Kim, J.-Y. Leem, J.-S. Son, J. Korean Phys. Soc., 68 (2016) 705–709.
[118] C.-T. Pan, R.-Y. Yang, M.-H. Weng, C.-W. Huang, Thin Solid Films 539 (2013) 290–293.
[119] S. Inguva, R.K Vijayaraghavan, E. McGlynn, J.P. Mosnier, Mater. Res. Express, 2, 096401 (2015).
[120] J.-L. Wu, H.-Y. Lin, Y.-C. Chen, S.-Y. Chu, C.-C. Chang, C.-J. Wu, Y.-D. Juang, ECS J. Solid State Sci. Techno., 2 (2013) 115–119.
[121] A. Miyake, T. Yamada, H. Makino, N. Yamamoto, T. Yamamoto, Thin Solid Films 517 (2009) 3130–3133.
[122] B.D. Cullity, Elements of X-ray Diffraction, 2nd ed., Addison Wesley, Reading, MA, 1978, p. 102.
[123] K Ellmer, J. Phys. D: Appl. Phys. 34 (2001) 3097–3108.
[124] T. Minami, S. Suzuki, T. Miyata, Mat. Res. Soc. Symp. Proc., 666 (2001) F1.3.1–F1.3.7
[125] J.Y.W. Seto, J. Appl. Phys., 46 (1975) 5247–5254.

Chapter 2
Experiment

2.1. Sample preparation

2.1.1. Thermal nanoimprint

The nanoimprint method is a technique to transcribe the surface shape of a material used as a mold to a glass material such as a polymer, as in stamping [1]. Once a mold is made, the shape can be transcribed to a large area at once [2]. In addition, being able to use it repeatedly is economical [3]. Figure 2.1 shows schematics of the thermal nanoimprinting process. First, the mold and substrate are placed, and then the mold is heated to a temperature above the glass transition temperature of to lower the viscosity of substrate, which is then pressed to transcribe the mold shape to the substrate. The mold is then cooled, and the pressure is removed to release the mold. This simple process can be used to modify the surface shape.

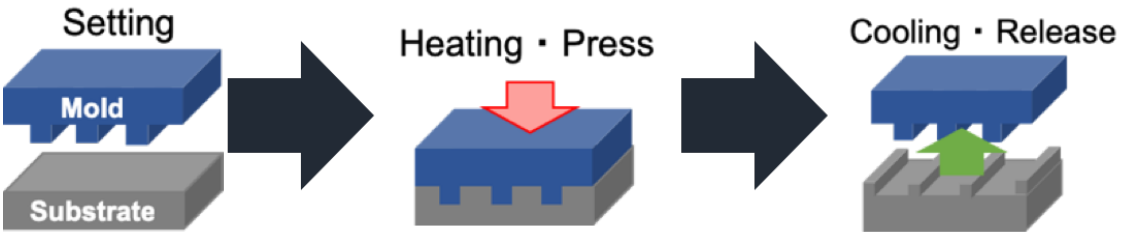

Figure 2.1 Schematic of the thermal nanoimprint process

Thermal nanoimprinting on thermoplastics is generally performed at temperatures about 40ºC above T_g and under conditions of several to several hundred MPa [4]. In this experiment, thermal nanoimprinting was performed using a nanoimprint system (X300, SCIVAX corp.). Double side polished glassy carbon sheets which are high specific heat property to avoid thermal shock and aluminum foil to enhance adhesion were inserted between the sample and the heating/pressure stage.

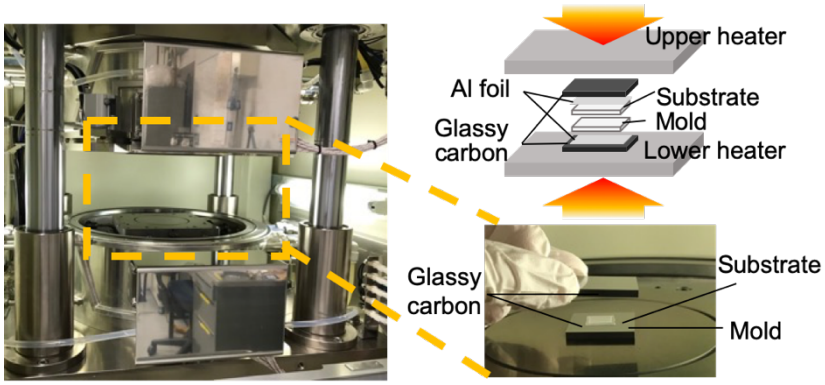

Figure 2.2 Appearance of the nanoimprinting system and the sample setup for this experiment.

An atomic step structure of a single crystal of inorganic material ordered at sub-nanometer height surface was employed as the molds [5,6]. The atomic step shape of the surface of a single-crystal substrate is obtained by the misalignment between the crystal orientation of the substrate and the substrate surface miscut. The rearrangement of atoms in such a way as to decrease the surface free energy creates a step-terrace shape [7]. The width of the terrace W is determined from the angle θ between the substrate orientation and the miscut surface and the step height h, which is determined by the crystallography of the substrate material is determined by the following equation.

$$H = W \cdot \tan\theta$$

The step height is specific to each crystallographic surface of the material, and the terrace width can be arbitrarily changed by changing the angle of the miscut. It is possible to impart atomic step to single-crystal substrates by using acid etching or heat treatment as a method to induce self-assembly [8,9]. Even in materials that exhibit cleavage with low interlayer binding energy, an atomic step can be obtained by displacing the cleavage angle from the cleaved crystalline plane [10,11].

2.1.2. Vacuum ultraviolet (VUV) light irradiation

Surface modification and treatment using light such as lasers and lamps are very widely used [12,13]. Surface modification of polymer materials is also performed using light irradiation at various wavelengths. Among them, ultraviolet (UV) light, which has a short wavelength and large photon energy, is expected to have a greater surface modification effect because it corresponds to the binding energy of the polymer material [14]. Excimer light sources are used as UV light sources for surface modification because of their intensity and convenience [15]. Excimer, in which excited atoms combine to form molecules, decomposes in a short-lived manner, emitting photons corresponding to the excitation energy. The wavelength varies depending on the discharge gas, but in particular, those by Xe gas have a wavelength of 172 nm [15]. This corresponds to what is called "Vacuum Ultraviolet (VUV) light", since light under 200 nm is absorbed especially in the atmosphere. At this wavelength, not only does it have a large photon energy, but also when irradiated with excimer light in the atmosphere, absorption of oxygen and following reactions was occurred [16].

$$O_2 + h\nu \rightarrow O(^3P) + O(^1D)$$

The dissociated oxygen atoms then generate oxygen radicals and ozone through the following reactions.

$$O_2 + O(^3P) \rightarrow O_3$$

From the above, it must be noted that when VUV light is used in air, the actual intensity of the light up to the sample surface is reduced due to absorption of oxygen in the air and the generation of ozone and oxygen-active species that are generated. Figure 2.3 shows an attenuation curve for a wavelength of 172 nm calculated from the absorption coefficient of oxygen versus wavelength and the partial pressure of oxygen in the atmosphere [17]. It is estimated that the exponential decrease in irradiation intensity and the generation of ozone and other substances increase with irradiation distance.

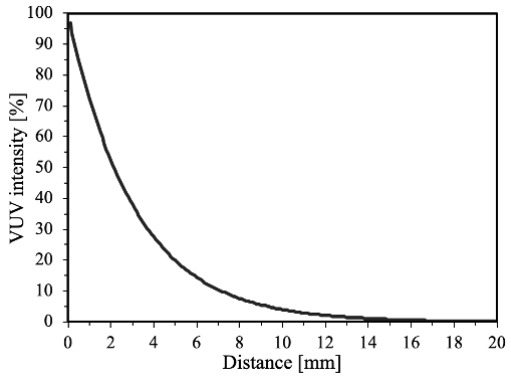

Figure 2.3 Attenuation curve of light at 172 nm in air calculated from the absorption coefficient and partial pressure of oxygen.

Among VUV light sources using excimer, surface modification using excimer lamps has been attracting attention in recent years. Compared to conventional modification methods using laser or plasma treatment, excimer lamps enable surface modification by uniformly and continuously irradiating a large area under mild conditions [15]. In addition, compared to the conventionally used low-mercury lamps, excimer lamps have higher photon energy and can generate monochromatic light. For excimer lamp light sources, radio frequency (RF) discharge of flat lamps was adopted to ensure uniform, flicker-free, and stable irradiation of large areas (FLAT EXCIMER EX-mini, Hamamatsu Photonics K.K., Japan). A schematic diagram of the excimer lamp used in this study is shown in Figure 2.4. Samples were located by adjusting the stage position from the lamp surface. Irradiation atmospheres are available in air and inert gas substituted, as well as a vacuum chamber in which the sample is sealed. Air in the equipment is always exhausted except when it is replaced by an inert gas.

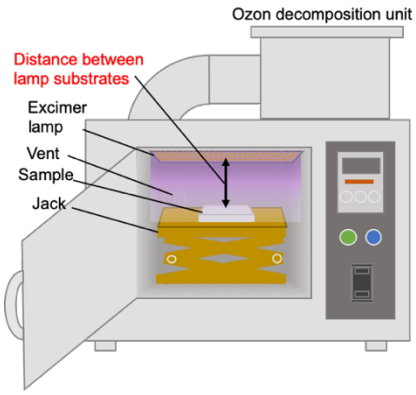

Figure 2.4 Schematic diagram of the excimer lamp used in this experiment.

2.1.3. Pulsed Laser Deposition (PLD)

While chemical vapor deposition (CVD) is a thin film deposition method that utilizes chemical reactions, physical vapor deposition (PVD) is a thin film deposition method in which the target material is evaporated to form a thin film with its original composition. PVD methods include vacuum evaporation, which forms a thin film by evaporating a target material in a vacuum chamber by heating, laser, or electron beam and depositing it on an opposing substrate [18-20], and sputtering, which uses the phenomenon that atoms or molecules constituting a solid are released into space when accelerated particles strike a solid surface [21]. In this study, the pulsed laser deposition (PLD) method was employed as a thin film deposition technique on polymer substrates. The PLD method uses laser light as the evaporation source of solid target materials. The target materials are ablated into electronic, photochemical, and thermal energy are ablated on the solid surface when irradiated with laser light above a threshold value, and neutral atoms, molecules, positive and negative ions, radicals, clusters, electrons, and photons are emitted, which fly in and form a thin film on the opposing substrate [22]. KrF excimer at a wavelength of 248 nm was used in this experiment. This wavelength corresponds to a relatively large photon energy of about 5 eV, which is suitable for the formation of wide bandgap oxide materials including ZnO. The PLD method, which can obtain relatively high-energy precursors without intentionally heating the substrate, makes it possible to form highly crystalline thin films at low temperature [23]. In PVD methods such as sputtering, the substrate temperature usually rises considerably without actually heating it intentionally [24]. In contrast, the increase in substrate temperature during thin film formation by the PLD method, as measured by thermocouples, is limited to a rise of only a few degrees [25]. A schematic of the PLD system used in this study is shown in Figure 2.5.

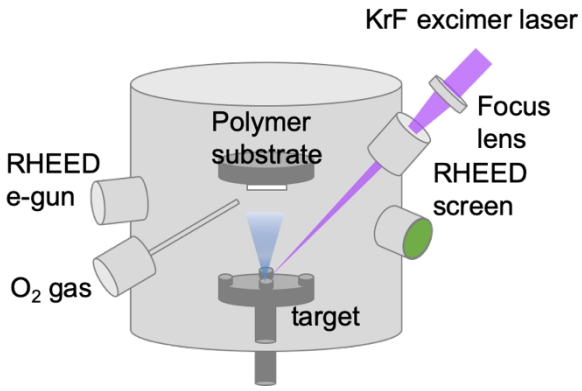

Figure 2.5 Schematic diagram of PLD system in this experiment.

The KrF excimer laser light (λ=248 nm, pulse width ~20 ns) was focused onto the target surface through a synthetic quartz window. The energy value to be introduced was adjusted at front of the introduction window. The base pressure in the chamber was set to an ultrahigh vacuum of about 7×10^{-6} Pa by a turbo molecular pump, and oxygen gas was introduced through a nozzle. RHEED electron gun and a fluorescent screen were installed, and the sample after deposition was observed while being held in vacuum.

2.2. Analysis and Characterization

2.2.1. Atomic Force Microscope (AFM)

Atomic force microscopy (AFM) is classified as a scanning probe microscope (SPM), which is a method of scanning a sample surface using a probe [26]. The signal is based on the interaction between the tip and the sample, i.e., the interatomic force and the resulting leverage deflection. The deformation of the cantilever due to the atomic force is determined by detecting the position of the change in the reflection direction of the laser light emitted from the back of the cantilever using a photodiode and is output as a change in the distance from the sample surface. Because it uses atomic forces, it is also suitable for observing the surface topography of insulating materials. To avoid the influence of the cohesive force between the cantilever and the sample, there is a tapping method in which the cantilever is vibrated near its resonance frequency and the interaction is detected as a change in its vibration characteristics. This is expected to be applied to the measurement of soft or soft samples.[27]

2.2.2. Contact angle measurement

The contact angle method is generally used to evaluate the surface energy of solids. The contact angle is the angle between the solid surface and the tangent line drawn to the droplet at the intersection of the solid surface and the droplet surface on the solid as shown in Figure 2.6.

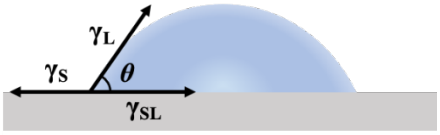

Figure 2.6 Schematic diagram of Contact angle between solid surface and liquid.

The relationship between the contact angle on the solid is as follows [28],

$$\gamma^{S} = \gamma^{SL} + \gamma^{L}\cos\theta$$

where γ^{L} is the liquid, γ^{S} is the solid, and γ^{SL} corresponds to the surface free energy

(surface tension) of the liquid/solid.

γ^{SL} is the surface energy per unit area, a scalar quantity with units [Jcm^{-2}], which can be balanced by the surface tension and has the same dimension as the surface free energy with units [Nm^{-1}]. Wettability is defined by the magnitude of the contact angle θ. The smaller θ is, the better the wettability (hydrophilic), and the larger θ is, the worse the wettability (hydrophobic) [29]. In this experiment, 2 μL of liquid was dropped and the contact angle was estimated by the *θ/2* method [30]. Surface free energy can also be classified by the same mechanism as intermolecular forces [31]. The components of surface free energy γ are classified into dispersive components γ^d and γ^h based on hydrogen bonding and dipole-dipole interactions by the Owens-Wendt formula [32].

$$\gamma = \gamma^d + \gamma^h$$

From the above equation, the surface free energy of the film can be determined by finding the respective contact angles at two liquid and solid surfaces with known surface free energies.

2.2.3. Reflection High Energy Electron Diffraction (RHEED)

Reflection high-energy electron diffraction (RHEED) is a method of examining the crystal structure and surface topography of a sample from the diffraction pattern of accelerated electron beams incident on the sample surface at a small angle and diffracted by a crystal lattice and projected onto a fluorescent plate [33]. Diffraction is obtained by the wave nature of the electrons, and its wavelength is expressed by the acceleration voltage as follows,

$$\lambda = \frac{h}{\sqrt{2meV}}$$

In this study, the accelerating voltage was set to 25 kV, which corresponds to a wavelength of about 0.076 Å. Grazing incident angles allow the electron beam to penetrate only a few atomic layers from the sample surface, making the near-surface structure sensitive. However, due to the effect of the Laue function for finite sample sizes when the surface consists of out-of-phase domains smaller than the coherence length of the electron beam, the width of the reciprocal rod becomes wider, and the intersection of the Ewald sphere and the reciprocal rod is a large ellipse. The RHEED pattern projects a long, narrow diffraction spot (streak) [34].

2.2.4. X-ray diffraction (XRD)

X-ray diffraction (XRD) is a method for identifying crystal structures using the diffraction phenomenon that occurs when X-rays with wavelengths close to the lattice spacing are incident on a sample. When the lattice spacing is d, the path difference of X-rays scattered between the lattice planes is given by the following Bragg's equation [35]

$$2d\sin\theta = n\lambda$$

When the path difference is an integer multiple of the incident X-ray wavelength λ, the phases match and show a high intensity ratio. θ is the Bragg angle, and 2θ (the angle between the incident and diffracted X-ray directions) is the diffraction angle. X-ray diffraction profiles can be obtained by incident x-rays of known wavelength λ on a material and measuring the diffraction angle 2θ and its diffraction intensity. The intensity and width of the peaks depend on the strain of the constituent crystal lattice and the degree

of crystallization, revealing the crystal structure of the sample. In this study, the characterization of crystal planes and the evaluation of crystallinity were employed by XRD system with Bragg-Brentano optics (RINT-2100V, Rigaku Corp.) and parallel beam optics (Smart lab, Rigaku Corp.).

XRD measurements were also used to assess the degree of orientation of the samples. Although the degree of orientation may indicate the degree to which a particular crystal plane has grown in alignment, the degree of orientation in an oriented thin film is generally considered to represent the degree of dispersion of a particular crystal orientation. Rocking-curve measurement is a method of evaluating the degree of dispersion by measuring the change in diffraction intensity as the sample is rocked with respect to a certain diffraction plane of the thin film [36]. It is also used to evaluate the in-plane orientation of a sample by scanning it extensively in the direction of crystal rotation, and to identify the symmetry of a crystal plane and epitaxial growth. In this study, the orientation of the thin films was evaluated by XRD measurements with a two-dimensional (2D) detector (Pilatus, Rigaku Corp,). The 2D-detector is a device that has the ability to simultaneously acquire intensities in two-dimensional space and analyze them as two-dimensional diffraction data, while the scintillation counter measures only the intensities [37]. A schematic diagram of the intensity acquisition in reciprocal lattice space using the rectangular 2D-detector used in this experiment is shown in Figure 2.7. Since the obtained data are spatially separated, the intensity distribution corresponding to the intersection of the Ewald sphere and the reciprocal lattice point of the scattering vector $Q = k_o - k_i$, which satisfies Laue's condition, is recorded for each incidence angle [38]. The two-dimensional spatial arrangement of the diffracted X-ray intensities shows the spread of the lattice width and arrangement at a glance, i.e., the crystallinity and orientation can be evaluated at once.

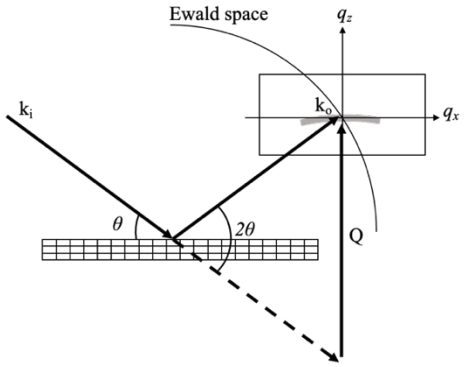

Figure 2.7 Schematic diagram of reciprocal space mapping using a two-dimensional detector.

2.2.5. Scanning Electron Microscope (SEM) and Transmission Electron Microscope (TEM)

Electron microscopy is a technique for observing microscopic features by irradiating electrons with wavelengths much shorter than those of visible light [39]. Electron microscopes are classified into transmission electron microscope (TEM) and scanning electron microscope (SEM) based on differences in principle [40]. TEM is a technique to obtain a transmission image of a sample by irradiating the sample with electrons accelerated by high voltage and magnifying the transmitted electron image. The principle of TEM image magnification is that the interference image of electrons transmitted through the sample is magnified and observed, the same way that the lens of an optical microscope magnifies the image. Therefore, the transmitted electrons are magnified and observed by forming an image with a magnetic field lens [41]. Although the sample to be observed must be very thin, it can be observed on the order of an atomic level, making it possible to evaluate arrangement of atoms. The samples were thinned by a focused ion beam and observed by a TEM (JEM-2100F, JEOL Ltd., Japan) with an acceleration voltage of 200 kV in this study.

SEM is a technique to obtain an image by detecting secondary electrons emitted from the sample surface while irradiating and scanning a sample with electrons (electron beam) focused by an objective lens [42]. FE-SEM is equipped with a field emission electron gun that can narrow down the electron beam to obtain an image with higher resolution [43]. SEM is widely used for its relatively simple observation of the morphology of the observed sample surface. The sample was cooled and solidified in liquid nitrogen and ruptured by bending, or cut with a blade to form a cross-section, and the surface was observed by FE-SEM (REGULUS 8230, Hitachi High-Tech Corp.).

2.2.6. X-ray Photoelectron Spectroscopy (XPS)

X-ray photoelectron spectroscopy (XPS) is an analytical technique to obtain information on the elements that make up a material and their chemical states by measuring the kinetic energy spectrum of photoelectrons emitted when electrons in atomic orbitals absorb photon energy when a sample is irradiated with light such as soft X-rays. Electrons have the following kinetic energies (E_k) [44].

$$E_k = hv - E_b - \varphi$$

where hv is the electron energy of the incident electron, E_b is the binding energy of the atoms in orbit, and φ, is the work function of the spectrometer. The binding energy can be thought of as the energy difference between the initial and final states of a photoelectron. Since each element has an inherent binding energy, elements can be identified from their spectra, and the chemical shift in the binding energy of an element identifies its chemical state [45]. In this experiment, measurements were performed with an XPS analysis instrument (Kratos Ultra 2, shimadzu Co.) using monochromatized AlKα (1486.6 eV) soft X-ray.

2.2.7. Time-of-Flight Secondary Ion Mass Spectrometry (ToF-SIMS)

Secondary ion mass spectrometry (SIMS) is a method for elemental analysis by mass separation of secondary ions generated by the sputtering phenomenon that occurs when a solid surface is irradiated with primary ions according to the mass-to-charge ratio [46].

Time-of-flight mass spectrometers are separated using the fact that the time it takes for secondary ions to reach the detector varies with mass [47]. The use of a time-of-flight analyzer allows for excellent mass resolution and sensitivity and depth profiling capabilities with good resolution [48]. All elements including hydrogen can be measured [49]. The samples in this experiment were analyzed for depth composition using a ToF-SIMS system (TOF-SIMS 5-100-AD, ION-TOF GmbH).

2.2.8. Ultraviolet-visible spectroscopy (UV-vis)

Ultraviolet-visible spectroscopy (UV-vis) is a method of optical evaluation based on optical absorption spectra by measuring the transmission of UV and visible light irradiated on a sample. When a material is irradiated with ultraviolet or visible light, it exhibits absorption specific to the material associated with the transition from the ground state to the excited state [50]. The following Bouguer-Beer law holds for this absorption and the incident light (I_o) and transmitted light (I), absorption coefficient (α), and film thickness (t) [51].

$$I = I_0 e^{-\varepsilon \alpha t}$$

In this study, optical transmittance was carried out in the wavelength range 190-900 nm by UV/vis (JASCO V-550, deuterium/halogen lamp). The system was employed with a double-beam system, in which the light emitted is divided into two beams by a beam splitter and irradiated to the sample and reference shown in Fig. 2.8.

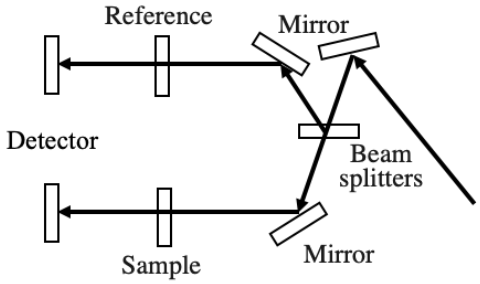

Figure 2.8 Schematic diagram of UV-visible spectrometer with double-beam line.

Transmittance was measured by dividing the light flux into two fluxes while correcting for the drift that occurs during measurement using the following equation.

$$\%T = \frac{\text{Sample}}{\text{Baseline}} \times 100 = \frac{\frac{\text{Sample}}{\text{Reference}} \times 100}{\frac{\text{Baseline}}{\text{Reference}} \times 100} \times 100$$

The double-beam method provides stable measurements with little drift over long periods of time. SEM is widely used for its relatively simple observation of the morphology of the observed sample surface.

2.2.9 Electrical resistivity measurement

Electrical resistance is one of the most important indicators in the application of electronic materials. Various methods are used to measure electrical resistance [52]. Figure 2.9 shows a typical resistance measurement technique.

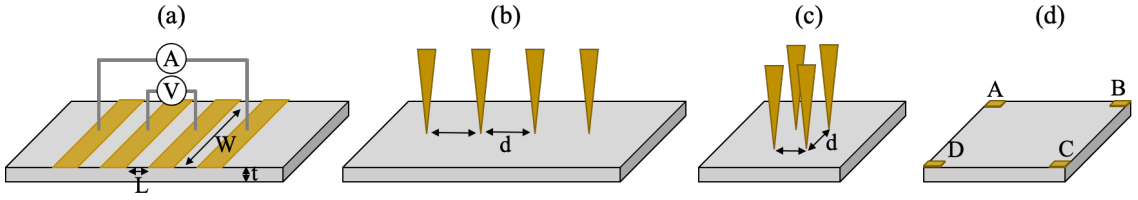

Figure 2.9 Schematics of the resistivity measurement employed in this experiment: (a) 4-terminal method, (b) in-line 4-probe method, (c) square 4-probe method, (d) van der Pauw method.

The 2-terminal method is the simplest measurement method, but it is not appropriate for low-resistance samples because it includes contact resistance. Therefore, in the 4-terminal method shown in Fig. 2.9 (a), current flows through the outer electrode and the potential difference are measured via the inner electrode. This method is suitable for low-resistance and accurate resistance measurements because it eliminates the effect of contact resistance with the sample.

$$\rho = \frac{Wt}{L}\frac{V}{I}$$

where I is the current, V is the potential difference, W is the width of electrode, and L is the distance between each electrode.

Among the 4-terminal methods, the 4-point probe method shown in Fig. 2.9 (b) and (c), is a simple technic for measuring the resistance of a sample. This method is applicable when the distance between probes is small enough for the sample size. The resistivity of a sample measured for a probe arrangement and two-dimensional sample is given by the following equation [53].

$$\rho_{\text{line}} = \frac{\pi t}{\ln 2}\frac{V}{I}$$

$$\rho_{\text{square}} = \frac{2\pi t}{\ln 2}\frac{V}{I}$$

where I is the current and V is the potential difference.

In contrast, the van der Pauw method shown in Fig. 2.9 (d) of measuring resistivity does not limit the sample shape. However, the electrodes must be located on the corner of the sample, they must be small enough for the sample size, ohmic contact must be obtained, and the sample thickness must be uniform, and the sample surface must have a single connection and no isolated holes [54]. As shown in Figure 2.9 (d), the resistance of an arbitrarily shaped sample is given by the following equation from the resistance between each electrode [52-54].

$$\rho = \frac{\pi t}{\ln 2}\left[\frac{R_{\text{AB,CD}} + R_{\text{BC,DA}}}{2}\right] f\left(\frac{R_{\text{AB,CD}}}{R_{\text{BC,DA}}}\right)$$

2.2.10. Hall effect measurement

Hall effect measurement has been an important method for characterization of semiconductors since it was reported by Edwin Hall in 1879, including identification of charge carriers [55]. Hall effect measurements utilize the phenomenon generated by the Lorentz force, in which the application of a magnetic field perpendicular to the current flowing through a sample produces an electric field in the direction perpendicular to the current and the magnetic field. The following relationship is shown between resistivity ρ, carrier density n, and carrier mobility μ [56,57].

$$\rho = \frac{1}{qn\mu}$$

When a perpendicular magnetic field B is applied, the charge carriers in motion are deflected by the Lorentz force. This deflection of charge carriers due to Lorentz force is compensated by the electric field generated by the redistribution of charge carriers. At steady state, the transverse current is zero and a Hall voltage is measured between opposite sides of the sample [56]. This Hall voltage is as shown in the following equation [56,57].

$$V_H = \frac{R_H IB}{d}$$

And the Hall coefficient is as follows [56,57]

$$R_H = \frac{V_H d}{IB} = \frac{1}{qn}$$

q is the carrier charge (holes > 0, electrons < 0). Therefore, if the Hall coefficient is negative, it is an n-type semiconductor or if positive, a p-type semiconductor.

In this study, the electrical properties of the samples were evaluated at RT in air under a magnetic field of 0.4 T using a van der Pauw-type Hall effect measurement system (HEMS-MD-S-30, Seinan Industry Co., Japan). Hall resistance was measured by reversing the direction of the magnetic field and current, respectively.

Reference

[1] H. Schift, J. Vac. Sci. Technol. B, 26 (2008) 458–480.

[2] S. Zankovych, T. Hoffmann, J. Seekamp, J.-U. Bruch, C.M.S. Torres, Nanotechnology 12 (2001) 91–95.

[3] L.J. Guo, Adv. Mater., 19 (2007) 495–513.

[4] Y. Hirai, T. Yoshikawa, N. Takagi, S. Yoshida, K. Yamamoto, J. Photopolym. Sci.Technol., 16 (2003) 615–620.

[5] M. Kawasaki, K. Takahashi, T. Maeda, R. Tsuchiya, M. Shinohara, O. Ishiyama, T. Yonezawa, M. Yoshimoto, H. Koinuma, Science, 266 (1994) 1540–1542.

[6] V.E. Henrich, S.K. Shaikhutdinov, Surf. Sci., 574 (2005) 306–316.

[7] R.L. Schwoebel, E.J. Shipsey, J. Appl. Phys., 37 (1966) 3682–3686.

[8] M. Yoshimoto, T. Maeda, T. Ohnishi, H. Koinuma, O. Ishiyama, M. Shinohara. M. Kubo, R. Miura, and A. Miyamoto, Appl. Phys. Lett., 67 (1995) 2615–2617.

[9] K. Lee, Y.J. Cho, L.J. Schowalter, M. Toita, H.G. Xing, D. Jena, Appl. Phys. Lett., 116, 262102 (2020).

[10] F. Ostendorf, C. Schmitz, S. Hirth, A. Kühnle, J.J. Kolodziej, M. Reichling, Nanotechnology, 19, 305705 (2008).

[11] R. Bennewitz, M. Reichling, E. Matthias, Surf. Sci., 387 (1997) 69–77.

[12] K. Efimenko, W.E. Wallace, J. Genzer, J. Colloid Interface Sci., 254, (2002) 306–315.

[13] J.-Y. Cheng, C.-W. Wei, K.-H. Hsu, T.-H. Young, Sens. Actuators B, 99 (2004) 186–196.

[14] A. Hozumi, T. Masuda, K. Hayashi, H. Sugimura, O. Takai, T. Kameyama, Langmuir, 18 (2002) 9022–9027.

[15] J. Wieser, D.E. Murnick, A. Ulrich, H.A. Huggins, A. Liddle, W.L. Brown, Rev. Sci. Instrum., 68 (1997) 1360–1364.

[16] E.A. Sosnin, T. Oppenländer, V.F. Tarasenko, J. Photochem. Photobiol. C: Photochemistry Reviews, 7 (2006) 145–163.

[17] K. Watanabe, M. Zelikoff, J. Opt. Soc. Am., 43 (1953) 753–755.

[18] Y.W. Heo, D.P. Norton, S.J. Pearton, J. Appl. Phys. 98, 073502 (2005).

[19] X.M. Fan, J.S. Lian, Z.X. Guo, H.J. Lu, Appl. Surf. Sci., 239 (2005) 176–181.

[20] Y. Nakanishi, A. Miyake, H. Kominami, T. Aoki, Y. Hatanaka, G. Shimaoka, Appl. Surf. Sci., 142 (1999) 233–236.

[21] P.F. Carcia, R.S. McLean, M.H. Reilly, G. Nunes, Jr., Appl. Phys. Lett., 82 (2003) 1717–1119.

[22] K. Niemax, Fresenius J. Anal. Chem., 370 (2001) 332–340.
[23] G. Li, W. Wang, W. Yang, Y. Lin, H. Wang, Z. Lin, S. Zhou, Rep. Prog. Phys., 79 056501 (2016).
[24] U. Betz, M.K. Olsson, J. Marthy, M.F. Escolá, Thin Solid Films, 516 (2008) 1334–1340.
[25] A. Suzuki, T. Matsushita, T. Aoki, Y. Yoneyama, M. Okuda, Jpn. J. Appl. Phys., 40 (2001) L401–L403.
[26] G. Binnig, C.F. Quate, C. Gerber, Phys. Rev. Lett., 56 (1986) 930–934.
[27] C.A.J. Putman, K.O.V.d. Wetf, B.G.D. Grooth, N.F.V. Hulst, J. Greve, Appl. Phys. Lett., 64 (1994) 2454–2456.
[28] D.Y. Kwok, A.W. Neumann, Adv. Colloid Interface Sci., 81 (1999) 167–249.
[29] R.J. Good, J. Adhesion Sci. Technol., 6 (1992) 1269–1302.
[30] M.-W. Yang, S.-Y. Lin, Colloids Surf. A Physicochem. Eng. Asp., 220 (2003) 199–210.
[31] F.M. Fowkes, J. Phys. Chem., 67 (1963) 2538–2541.
[32] D.K. Owens, E.I.d.P.d Nemours, J. Appl. Polym. Sci., 13, (1969) 1741–1747.
[33] P.A. Maksym, J.L. Beeby, Surf. Sci., 110 (1981) 423–438.
[34] S. Hasegawa, Electron Technol., 12 (2012) 1925–1938.
[35] W.H. Bragg, W.L. Bragg, Proc. R. Soc. Lond. Ser. A-Contain. Pap. Math. Phys. Character, 88 (1913) 428–438.
[36] R. Chierchia, T. BWttcher, H. Heinke, S. Einfeldt, S. Figge, D. Hommel, J. Appl. Phys., 93 (2003) 8918–8925.
[37] O. Massona, A. Boulle, R. Guinebretière, A. Lecomte, A. Dauger, Rev. Sci. Instrum., 76, 063912 (2005).
[38] M. Meduňa, F. Isa, F. Bressanc, H.v. Känelb, J. Appl. Cryst., 55, (2022) 823–836.
[39] Egerton, R. F. Physical Principles of Electron Microscopy: An Introduction to TEM, SEM, and AEM, 2nd ed, Springer New York, NY, 2005, p. 1–25.
[40] C.T.K.-H. Stadtländer, Scanning electron microscopy and transmission electron microscopy of mollicutes: challenges and opportunities," Modern Research and Educational Topics in Microscopy, Formatex Badajoz, Spain, 2007, p. 122–131.
[41] E. Ruska, Reviews of Modern Physics., 59 (1987) 627–638.
[42] H. Seiler, J. Appl. Phys., 54 (1983) R1–R18.
[43] A.V. Crewe, D.N. Eggenberger, J. Wall, L.M. Welter, Rev. Sci. Instrum., 39 (1968) 576–583.
[44] J. F. Moulder, W. F. Stickle, P. E. Sobol, and K. D. Bomben, Handbook of X-Ray Photoelectron Spectroscopy, Perkin-Elmer Corporation, Eden Prairie, 1992, p. 9–12.

[45] C.S. Fadley, J. Electron Spectros. Relat. Phenomena, 178–179 (2010) 2–32.
[46] B.T. Chait, K.G.Standing, , Int. J. Mass Spectrom. Ion Phys., (1981) 185–193.
[47] A.M. Belu, D.J. Graham, D.G. Castner, Biomaterials, 24 (2003) 3635–3653
[48] R.N.S. Sodhi, Analyst, 129 (2004) 483–487.
[49] Z. Zhu, V. Shutthanandan, M. Engelhard, Surf. Interface Anal., 44 (2012) 232–237.
[50] P. Makuła, M. Pacia, W. Macyk, J. Phys. Chem. Lett., 9 (2018) 6814−6817.
[51] W. Mäntele, E. Deniz, Spectrochim. Acta A Mol. Biomol. Spectrosc., 173 (2017) 965–968.
[52] Y. Singh, Int. J. Mod. Phys.: Conf. Ser., 22 (2013) 745–756.
[53] I. Miccoli, F. Edler, H. Pfnür, C. Tegenkamp, J. Phys.: Condens. Matter., 27, 223201 (2015).
[54] A.A. Ramadan, R.D. Gould, A. Ashour, Thin Solid Films, 239 (1994) 272–275.
[55] E.H. Hall, Am. J. Math., 2 (1879) 287–292.
[56] F. Werner, J. Appl. Phys. 122, 135306 (2017).
[57] R. Green, Hall effect measurements in materials characterization, Keithley White pap., 3111 (2011) p. 1–11.

Chapter 3
Crystal growth and properties of ZnO thin films on nanoimprinted polymer substrates

3.1 Introduction

Oxide thin films, which are high quality are generally prepared by epitaxy technics on single crystal substrates or by high temperature growth on oxide glass substrates [1,2]. However, forming flexible devices on polymer substrates requires deposition techniques that consider glass transition at low temperatures and thermal expansion differences [3]. Among the oxide thin films, ZnO thin films are relatively easy to crystal grow even on amorphous substrates at low temperature [4,5]. However, their properties remain lower than those on single crystal or oxide glass substrates [6]. In order to reduce grain boundary scattering and control of oxygen defects from the viewpoint of TFT and TCO applications, the formation of highly oriented and crystalline thin films contributes to the improvement of their properties. As for the effect of substrate surface roughness on the crystal growth of ZnO thin films, a flatter surface may contribute to better orientation of the ZnO thin film, and a larger specific surface area may lead to more ZnO nucleation sites [7,8]. Polymer substrates exhibit larger surface roughness than polished commercial oxide substrates. However, until now, there have not been many reports on the effect of surface roughness of polymer substrates on the crystal growth of ZnO thin films. The effect of polymer substrates with improved surface roughness from the inherent surface roughness derived from the manufacturing process on the crystal growth of ZnO thin films is also not clear. In this study, crystal growth and properties of ZnO thin films on polymer substrates with improved surface roughness by thermal nanoimprinting was investigated to prepare highly oriented ZnO thin films on polymer substrates.

3.2 Experiment

Prior to deposition of the thin film, the polymer substrates were carried out thermal nanoimprint using α-Al_2O_3 (sapphire) ($10\bar{1}2$) wafer molds with atomic steps. The stepped sapphire molds were obtained via thermal annealing commercial mirror-polished sapphire wafers at 1000 °C for 3 h in air [9]. Cyclo-olefin polymer (COP) sheets (10 mm × 10 mm, 188 μm thick, ZF16-188, Zeon Corp.,) were used as polymer substrate in this experiment. The atomic step and terrace pattern of the sapphire molds were transcribed onto the as-received COP sheets using a thermal nanoimprinting system (X-300S, SCIVAX Corp.) at 180 °C for 5 min under 2.0 MPa pressure in vacuum purged four times with Ar (99.9999%) gas of 3×10^3 Pa. A glassy carbon susceptor (Tokai Carbon Co., Ltd.) with a low thermal conductivity was used to prevent rapid temperature changes [10]. In addition, an aluminum foil was inserted to improve the adhesion between the susceptor and the sample. The thermal nanoimprinting procedure consisted of pressurizing to 2.0 MPa at room temperature, raising and holding the temperature, cooling to room temperature, and finally removing the pressure [11].

The ZnO thin films were deposited on the untreated and nanoimprinted COP substrates via PLD using KrF excimer laser (λ = 248 nm, laser fluence = 1.2 J cm^{-2}) with a sintered ZnO target (99.99%) at RT without intentionally heating. The O_2 gas pressure was fixed at 1.0×10^{-3} Pa, and target-substrate distance was located at 5 cm. The surface morphology of the samples was observed by atomic force microscopy (AFM; Nanocute/Nanonavi, Hitachi High-Tech Science Corp.) operated in the contact mode. The crystal structure of the thin films was characterized by X-ray diffraction (XRD; RINT-2100V, Rigaku Corp.) and reflection high energy electron diffraction (RHEED; Pascal Corp.). The orientation of ZnO thin films was evaluated by reciprocal space mapping (RSM) using point focused Cukα x-rays on an XRD system (Smart Lab, Rigaku) equipped with a two-dimensional detector (PILATUS 100 K/R, Rigaku). The progress of crystal growth of ZnO thin films was also observed by field emission scanning electron microscopy ((FE-SEM; REGULUS 8230, Hitachi High-Tech Corp.) of liquid nitrogen cooled and fractured samples. The optical transmittance of ZnO thin film on the COP sheet was measured using a UV/vis spectrophotometer (V-550, JASCO Corp.). The electrical properties of the samples were evaluated at RT in air under a magnetic field of 0.4 T using a van der Pauw-type Hall effect measurement system (HEMS-MD-S-30, Seinan Industry Co., Japan).

3.3 Results and Discussion

Figure 3.1 shows AFM image of sapphire mold with the atomic step and terrace pattern and cross-sectional profile of the location indicated by white line. A regularly arranged atomic step pattern was observed at approximately 500 nm intervals on the surface of the sapphire substrate used as the mold for nanoimprinting. The cross-sectional profile showed the formation of an atomic step pattern with a height of approximately 0.3 nm and an ultra-flat terrace structure on sapphire surface [9].

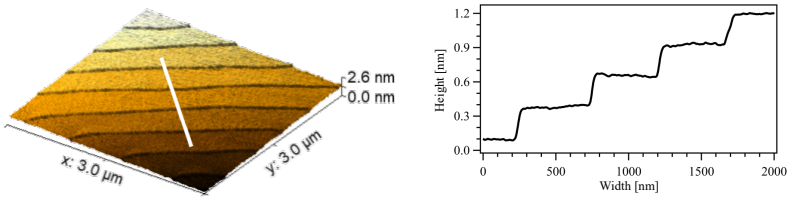

Figure 3.1 AFM images of sapphire mold with the atomic steps and cross-sectional profiles of the locations indicated by white lines.

Figure 3.2 shows AFM images of (a) untreated and (b) nanoimprinted COP substrate**.** The untreated COP substrate exhibited random irregularities, while the nanoimprinted COP substrate was observed to have a flat surface with the same atomic step pattern as the sapphire mold shown in Figure 3.1. The cross-sectional profile was also showed that an atomic step pattern with a height of about 0.3 nm and an ultra-flat terrace structure were formed on the COP substrate surface. The root-means-square (RMS) roughness was 0.8 nm for the untreated COP substrate but was reduced to about 0.2 nm for the nanoimprinted COP substrate.

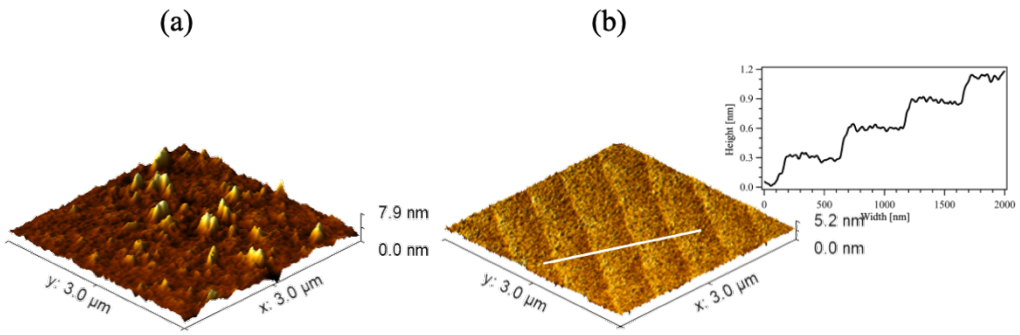

Figure 3.2 AFM images of (a) untreated and (b) nanoimprinted COP substrate and cross-sectional profiles of the locations indicated by white lines.

Figure 3.3 shows AFM images of ZnO thin films grown on (a) untreated and (b) atomic-step-pattern-transcribed (stepped) COP substrates. The surface morphology of the ZnO thin films reflected the topography of the COP substrate. The ZnO thin film grown on stepped COP substrate had a flat surface with a slightly visible atomic-step pattern of the COP substrate, while the ZnO thin film on the untreated substrate had an irregular surface reflecting the unevenness of the substrate. The RMS roughness was 3.0 nm for the untreated COP substrate, but was greatly reduced to about 0.6 nm for the nanoimprinted COP substrate. It has been found that the growth of ZnO on Si substrates is nearly perpendicular to the local plane direction of the substrate and clearly changes from a perpendicular arrangement to a flower-like morphology with increasing substrate surface roughness [10]. The original rough surface morphology of the polymer substrate may have induced crystal growth of the ZnO thin film in random directions, increasing the surface roughness.

On the other hand, we attempted to observe the initial crystal growth of ZnO thin films on the polymer substrates by taking advantage of the ultra-flatness of the stepped COP substrate, but the nuclei generated at RT were small in size and difficult to identify.

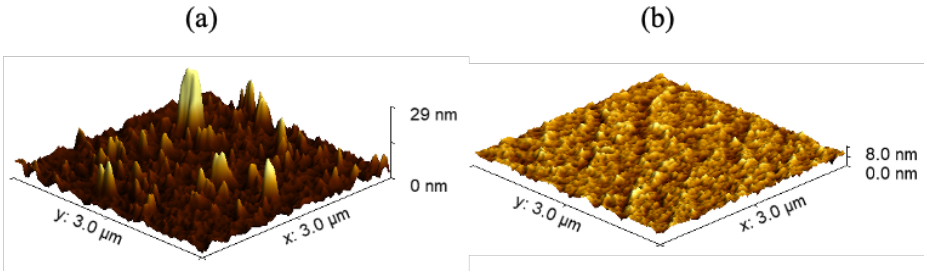

Figure 3.3 AFM images of ZnO thin films grown on (a) untreated and (b) stepped COP substrate.

The crystal structure ZnO thin films on substrates with different surface morphologies was characterized via XRD measurements and RHEED observations. Figure 3.4 shows the XRD 2θ/θ profiles of ZnO thin films grown on untreated and stepped COP substrates. The inset shows the respective RHEED patterns. The XRD profiles show that the ZnO thin films on both COP substrates have only a peak attributed to ZnO (0002) at about 34.0°, indicating oriented growth with a c-axis of about 0.53 nm. This is slightly larger than the stoichiometric bulk ZnO value, was suggested that the unit lattice has expanded due to the inclusion of oxygen vacancies and interstitial zinc [12]. The full width half

maximum (FWHM) value of the ZnO 0002 peak was estimated to be 0.69° for the ZnO thin film on the untreated COP substrate and 0.65° for the that on the stepped COP substrate. The FWHM value was decreased by about 6%, indicating that the crystallinity of the ZnO thin film on the stepped COP substrate was slightly improved. On the other hand, as seen in the RHEED image of the ZnO thin film grown on the stepped COP substrate, a slight streaky pattern was observed, but that of the ZnO thin film grown on the untreated COP substrate was only a ring pattern characteristic of randomly oriented polycrystalline films. Thus, the RHEED results indicate that the ZnO thin film grown on the stepped COP substrate had improved c-axis orientation.

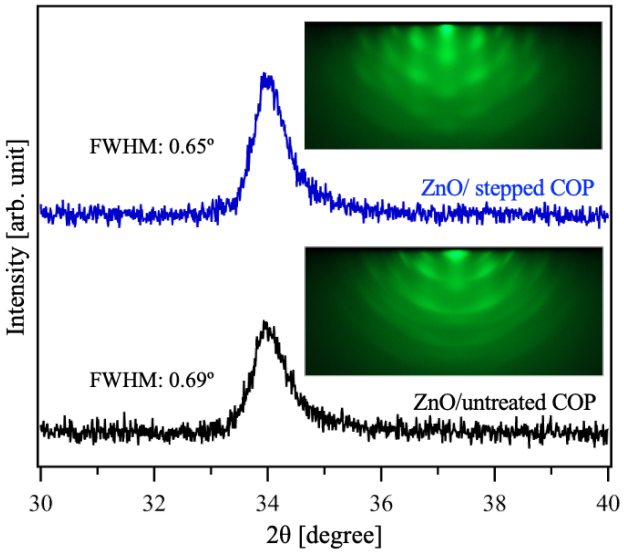

Figure 3.4 XRD 2θ/θ profiles and RHEED patterns (inset) of ZnO thin films grown on untreated and stepped COP substrates.

Reciprocal space mapping by XRD measurement using 2D-detector was performed to investigate of the detailed crystal growth and orientation of c-axis oriented grown ZnO thin films on COP substrates. Figure 3.5 shows the reciprocal space maps (RSMs) of ZnO thin films grown on untreated and stepped COP substrates. The same as the result of 2θ/θ-scan from Figure 3.4, only the peak attributed to ZnO *0002* was observed in both ZnO thin films. This also indicated that the ZnO thin films were grown in a roughly aligned c-axis orientation on the COP substrate. Considering the broadly large *0002* diffraction spread of the RSMs in evaluating the degree of orientation of c-axis oriented ZnO thin films on amorphous substrates, the commonly used θ or ω axis rocking-curve

measurement would not show the entire diffraction of ZnO 0002 from an XRD system arrangement perspective. One-dimensional profiles of the rocking-curves were obtained from each ZnO *0002* diffraction in the χ direction corresponding to the arc-like broadening on the RSMs to evaluate the orientation of the ZnO films on the COP substrate.

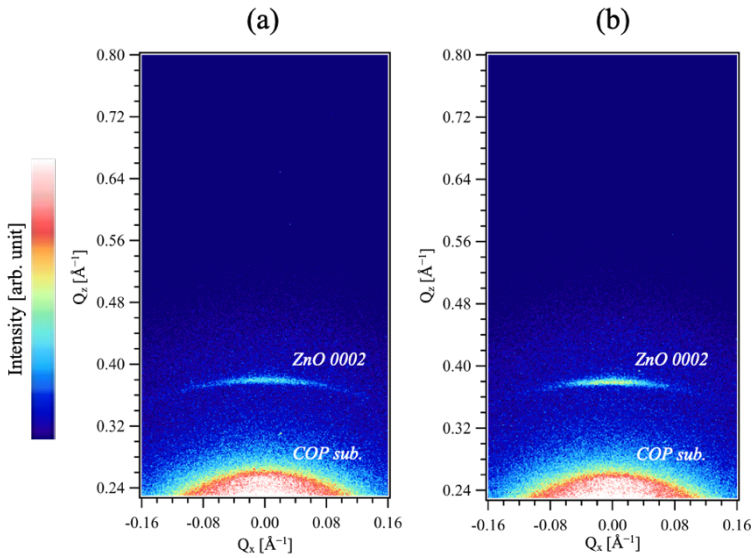

Figure 3.5 Reciprocal space maps of ZnO thin films grown on (a) untreated and (b) stepped COP substrates.

Figure 3.6 shows the χ-rocking curve results for ZnO thin films grown on untreated and stepped COP substrates. The rocking-curves extracted shows that contrasting peaks were obtained. The FWHM value was 17.9º for the ZnO thin film on the untreated COP substrate and 14.5º on the stepped COP substrate. Flattening the surface of the COP substrate would have improved the orientation of the ZnO thin film by about 20%.

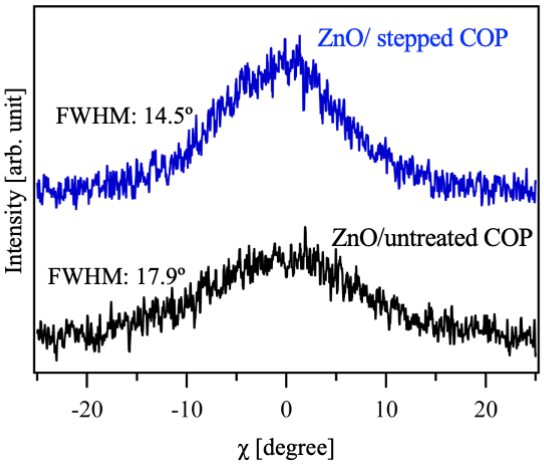

Figure 3.6 XRD rocking-curves of ZnO *0002* diffraction for the films on untreated and stepped COP substrate.

The entire ZnO *0002* diffraction spread in two-dimensional reciprocal lattice space in RSMs was converted to a 2θ/ω profile to investigate the crystallization of ZnO thin films. The range of integrated χ was approximately ±24° from the center of the peak. Figure 3.7 shows 2θ/ω profiles of ZnO thin films grown on the untreated and the stepped COP substrates. The results of general XRD 2θ/θ measurements in Figure 3.4 show that the integrated intensities of ZnO thin films grown on untreated and stepped COP substrates differ by about 20%, but the difference in the broad peak intensities obtained from the RSM was only about 5%. This suggested that the crystal growth of ZnO thin films on a flat COP substrate aligns the growth direction rather than influencing the degree of crystallization.

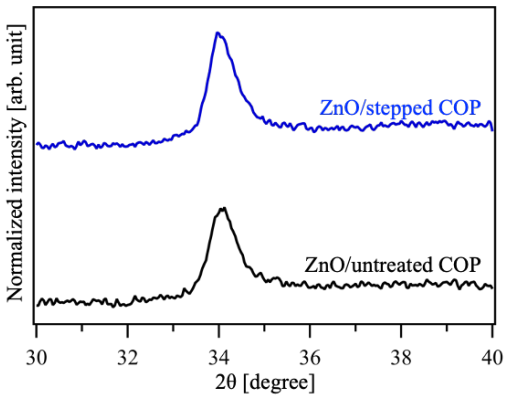

Figure 3.7 XRD 2θ/ω profiles of ZnO thin films grown on the untreated and the stepped COP substrates (the range of integrated χ was ±24°).

The influence of the surface morphology of the COP substrate on the crystal growth process of ZnO thin films was evaluated via cross-sectional observation of FE-SEM. SEM observation samples were immersed in liquid nitrogen to cool and reduce toughness, and the sample was broken by bending as it was, and the cross section was obtained. Figure 3.8 shows cross-sectional FE-SEM images of ZnO thin films grown on untreated and stepped COP substrates. The ZnO thin films on both COP substrates showed columnar growth, which was consistent with previous reports of c-axis oriented growth [13,14]. The ZnO thin film grown on the untreated COP substrate was found to grow in a slightly scattered orientation relative to the vertical of the substrate. The generation of domains in the film thickness direction was also confirmed. On the other hand, the growth of ZnO thin films on the stepped COP substrate was clearly aligned perpendicular to the substrate from the initial stage. The FE-SEM observations indicated that the crystal growth of ZnO thin films on COP substrates proceeds perpendicular to the topography of the COP substrate surface. Flatten surface of the COP substrate promotes vertically oriented growth of ZnO thin films and improves orientation was suggested.

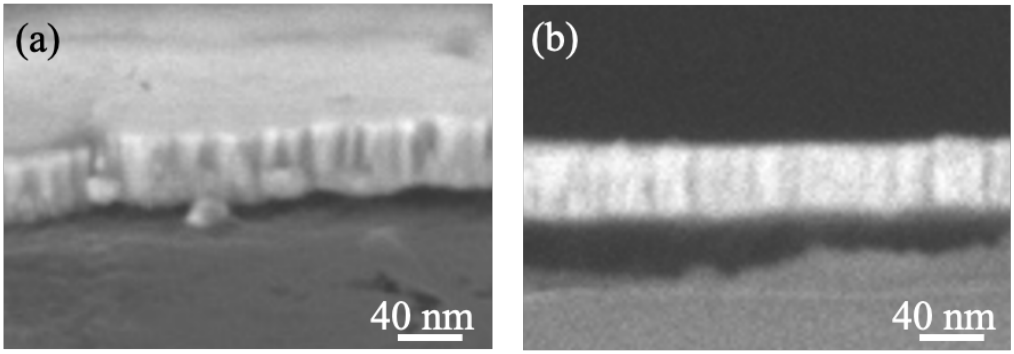

Figure 3.8 Cross-sectional FE-SEM images of ZnO thin films grown on (a) untreated and (b) stepped COP substrates.

Optical properties were characterized by UV/vis transmittance measurements. Figure 3.9 shows the transmittance of ZnO thin films on untreated and stepped COP substrates and the tauc plot results calculated near the band edge. Transmittance in the visible light range on both substrates was approximately 80% or higher. It was slightly higher for the ZnO thin film on the stepped COP substrate. The optical band gap of the ZnO thin films on both substrates was estimated to be about 3.3 eV from the Tauc plots. The ZnO thin film on the stepped COP substrate has slightly higher transmittance in the visible light transmission range, but the estimated optical band gap is almost the same value of that on

untreated COP substrate. This might be due to the fact that the orientation of the ZnO thin film was slightly improved, but the crystallinity was not so much improved, as shown in Figures 3.4 and 3.6.

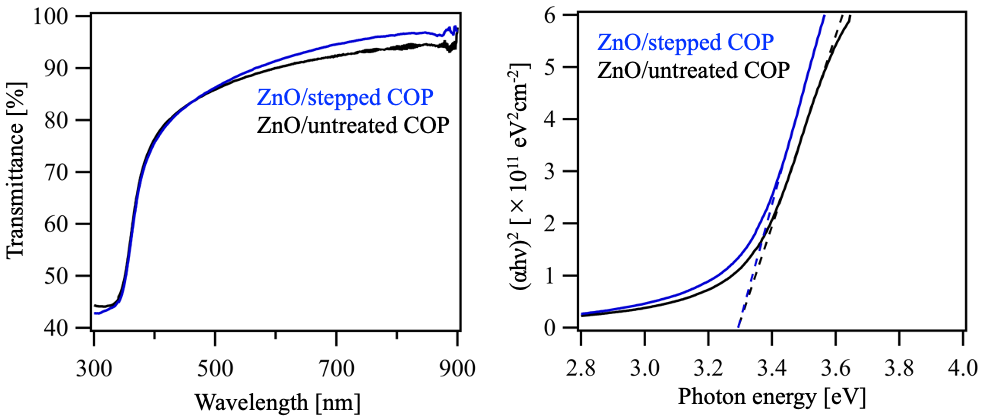

Figure 3.9 Transmittance of ZnO thin films on untreated and stepped COP substrates and the tauc plot results calculated near the band edge.

Table 3.1 shows electric properties of the ZnO thin films grown on the untreated and stepped COP substrates estimated from the van der Pauw-type Hall effect measurements at RT. The resistivity of ZnO thin film grown on the stepped COP substrate was reduced the about 4% from that on the untreated COP substrate. The slight improvement in resistivity was attributed to the increase in carrier concentration. The improvement of orientation of the ZnO thin film might have led to an increased the carrier concentration in the ZnO thin film, as shown in the results in Figure 3.6 where the change in orientation was large relative to the change in crystallinity. The oxygen defects and Zn intercalation act as donors in undoped ZnO films, may have been responsible for the carrier increase [15]. The improved orientation may have reduced the amount of oxygen adsorbed at grain boundaries and surfaces [16]. The slight decrease in Hall mobility might include the effect of ion scattering due to increased carrier concentration. However, further investigation is needed to clarify.

Table 3.1 Electric properties of the ZnO thin films grown on the untreated and stepped COP substrates estimated from the van der Pauw-type Hall effect measurements at RT.

Film sample	Resistivity (Ωcm)	Hall mobility ($cm^2V^{-1}s^{-1}$)	Carrier concentration (cm^{-3})
ZnO thin film on untreated COP	2.86×10^{-3}	14.0	1.55×10^{20}
ZnO thin film on stepped COP	2.75×10^{-3}	12.8	1.78×10^{20}

3.4 Summary

The crystal growth of ZnO thin films on polymer substrates with improved surface morphology was investigated. The ZnO thin films were grown by PLD at RT on a polymer substrate with an ultra-flat surface on which an atomic step pattern of approximately 0.3 nm height was transcribed by thermal nanoimprinting. The surface morphology of the ZnO thin film on the nanoimprinted polymer substrate was flat with an RMS roughness of 0.6 nm on a 3 μm square. XRD and RHEED analysis revealed that ZnO thin film grown on stepped COP substrates was (0001) oriented growth, with a slight crystallinity improvement and a clear orientation improvement. The growth of ZnO thin films on COP substrates was suggested c-axis oriented growth perpendicular to the substrate surface direction via RSM of XRD, and FE-SEM observation. A slight improvement in visible light transmittance and a decrease in resistivity of the ZnO thin film grown on stepped COP substrate was obtained.

Reference

[1] E.M. Kaidashev, M. Lorenz, H. von Wenckstern, A. Rahm, H.-C. Semmelhack, K.-H. Han, G. Benndorf, C. Bundesmann, H. Hochmuth, M. Grundmann, Appl. Phys. Lett., 82, (2003) 3901–3903.

[2] S.L. King, J.G.E. Gardeniers, I.W. Boyd, Appl. Surf. Sci., 96-98 (1996) 811–818.

[3] A.N. Banerjee, C.K. Ghosh, K.K. Chattopadhyay, H. Minoura, A.K. Sarkar, A. Akiba, A. Kamiya, T. Endo, T hin Solid Films, 496 (2006) 112–116.

[4] D.K. Kima, H.B. Kim, J. Alloys Compd, 509 (2011) 421–425.

[5] G. Socola, M. Socol, N. Stefan, E. Axente, G. Popescu-Pelin, D. Craciun, L. Duta, C.N. Mihailescu, I.N. Mihailescu, A. Stanculescu, D. Visan, V. Sava, A.C. Galca, C.R. Luculescu, V. Craciun, App. Surf. Sci., 260 (2012) 42–46.

[6] H.-L. Shen, H. Zhang, L-F Lu, F. Jiang, C. Yang, Prog. Nat. Sci., 20 (2010) 44─48.

[7] A. Artieda, M. Barbieri, C.S. Sandu, P. Muralt, J. Appl. Phys. 105, 024504 (2009).

[8] E.K. Chong, M.G. Stevens, K.E. Nissen, J. Adhes., 79 (2003) 667–681.

[9] M. Yoshimoto, T. Maeda, T. Ohnishi, H. Koinuma, O. Ishiyama, M. Shinohara. M. Kubo, R. Miura, and A. Miyamoto, Appl. Phys. Lett., 67 (1995) 2615–2617.

[10] Q.-H. Wang, C.-L. Tang, C.-M. Jiang, D.-F. Du, F. Wang, J.-H. Song, Acta. Metall. Sin. Engl., 29 (2016) 237–242.

[11] S. Yamada, H. Sato, Nature, 193 (1962) 261–262.

[12] T. Oga, S. Yamada, N. Kaneko, S. Kaneko, A. Matsuda, M. Yoshimoto, Jpn. J. Appl. Phys. 59, 128001 (2020).

[13] Y.-S. Kim, C.H. Park, Phys. Rev. Lett., 102, 086403 (2009).

[14] X. Li, Y. Wang, W. Liu, G. Jiang, C. Zhu, Mater. Lett., 85 (2012) 25–28.

[15] A.D. Mauroa, M.E. Fragalà, V. Privitera, G. Impellizzeri, Mater. Sci. Semicond. Process, 69 (2017) 44–51.

[16] T. Minami, Semicond. Sci. Technol., 20 (2005) S35–S44.

Chapter 4

Crystal growth and properties of ZnO thin films on polymer substrates surface-treated with vacuum UV light irradiation

4.1 Introduction

Formation of flexible devices on polymer substrates requires techniques to improve crystal growth, considering glass transition at low temperatures and thermal expansion differences [1]. Chemical modifications are generally selected because they are highly effective relative to physical modifications [2]. A typical example is the use of oxygen plasma treatment to form oxygen-containing functional groups to the polymer substrate surface in an attempt to increase the surface free energy of the substrate and induce nucleation sites for ZnO thin films [3-5]. On the other hand, such chemical surface modification is accompanied by surface morphological changes, and plasma treatment also has the effect of increasing surface roughness. Although the increase in substrate surface roughness is an advantage in terms of increased nucleation sites and adhesion, it is a negative factor in the oriented growth of ZnO thin films. It is also desirable to have a flat surface because surface roughness can lead to a decrease in performance and reliability during device formation [6].

As a surface modification technique, vacuum ultraviolet (VUV) light irradiation has the advantage of being gentle and highly effective in imparting polar functional groups to the surface in contrast to these chemical treatments [7]. Therefore, irradiation is expected to increase the surface free energy without increasing the roughness of the polymer surface [8]. Crystal growth of ZnO thin films on a flat and active polymer substrate surface is expected to improve orientation and crystallinity. In this study, the effect of VUV light irradiation for surface modification of polymer substrate surface on the crystal growth and properties of ZnO thin films was investigated.

4.2 Experiment

Cyclo-olefin polymer (COP) sheets (10 × 10 mm^2, 188 μm thick, ZF16-188, Zeon, Japan) were pretreated via VUV light irradiation with an Xe_2* excimer lamp light source (wavelength: 172 nm, irradiation intensity: 65 mW/cm^2, FLAT EXCIMER EX-mini, Hamamatsu Photonics, Japan) as a surface modification for the polymer substrate. Since VUV light attenuates during irradiation due to the absorption of oxygen gas in air, the light intensity on the sample surface was calculated from the oxygen partial pressure in the air and the absorption coefficient [9]. As a result, it was confirmed that the light intensity decreased to about 50% of the initial value. The excited oxygen species such as ozone and oxygen radicals in the atmosphere would be also generated around the sample during VUV light irradiation [10].

Subsequently, the ZnO thin films were deposited on the untreated and VUV light pretreated COP substrates by pulsed laser deposition (PLD) using KrF excimer laser (λ = 248 nm, laser fluence = 1.2 Jcm^{-2}) with a sintered ZnO target (99.99%) at room temperature (RT) without intentionally heating. The O_2 gas pressure was fixed at 1.0 × 10^{-3} Pa. The target-substrate distance was located at 5 cm.

The surface morphology of the samples was observed by atomic force microscopy (AFM; Nanocute/Nanonavi, Hitachi High-Tech Science Corp.) operated in the contact mode. The chemical state of the COP substrate surface was determined by determining the contact angle by the θ/2 method using a drop method with approximately 2 μL of liquid. The crystal structure of the thin films was characterized by X-ray diffraction (XRD; RINT-2100V, Rigaku Corp.) and reflection high energy electron diffraction (RHEED; Pascal Corp.). The orientation of ZnO thin films was evaluated by reciprocal space mapping (RSM) using point focused Cukα x-rays on an XRD system (Smart Lab, Rigaku) equipped with a two-dimensional detector (PILATUS 100 K/R, Rigaku). The initial growth of ZnO thin films was also observed by cross-sectional transmission electron microscope (TEM, JEM-2100F, JEOL Ltd., Japan) at 200 kV. The polarity of the ZnO films was determined by X-ray photoelectron spectrometer (XPS; AXIS Supra, Shimadzu corp.). The compositional state of the ZnO thin films and COP substrates was analyzed by a time-of-flight secondary ion mass spectrometer (TOF-SIMS) system (TOF-SIMS 5-100-AD, ION-TOF GmbH). The optical transmittance was measured using an ultraviolet-visible (UV/vis) spectrophotometer equipped with double-beam optics. (V-550, JASCO Corp., Japan). The electrical properties of the samples were evaluated at RT in air under a magnetic field of 0.4 T using a van der Pauw-type Hall effect measurement system (HEMS-MD-S-30, Seinan Industry Co., Japan).

4.3 Results and Discussion

Figure 4.1 shows (a) AFM images (3 × 3 μm^2) and (b) surface roughness profiles of untreated and VUV light irradiated COP substrates for 60 s, 300 s, and 600 s. The untreated COP substrate surface showed random unevenness, but the COP substrates irradiated with VUV light irradiation for more than 60 seconds showed flat surfaces as surface irregularities disappeared. This is thought to be due to dry etching caused by oxidation reactions such as ozone generated [11]. The root means square (RMS) roughness of the untreated COP substrate was 0.8 nm, which was reduced to approximately 0.2 nm by VUV light irradiation. The RMS roughness was decreased exposure up to 300 s of VUV-light irradiation, but increased slightly over 300 s of VUV-light irradiation. This was suggested that the COP substrate surface was degraded due to degradation into low molecular weight fragment caused by excessive irradiation [12].

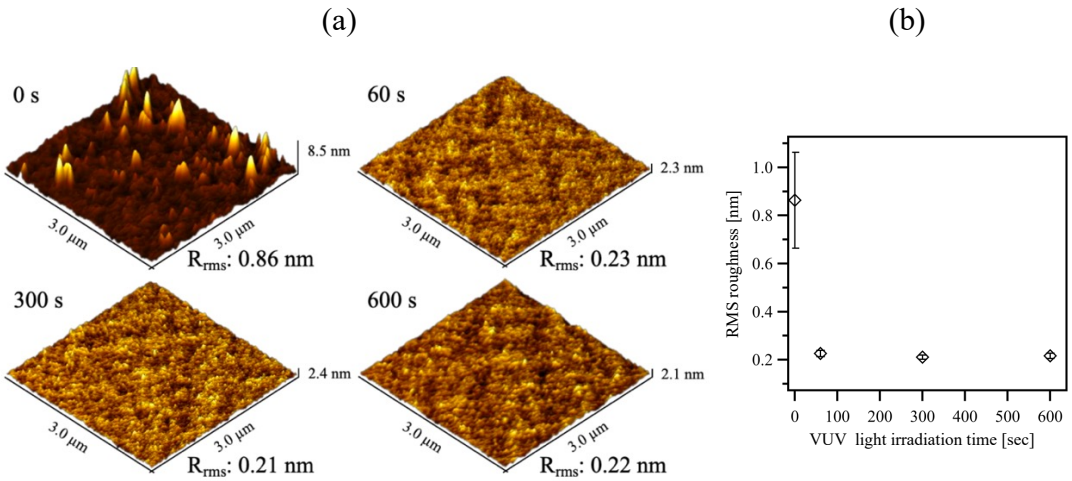

Figure 4.1 (a) AFM images and (b) surface roughness profiles of untreated and VUV light irradiated COP substrates for 60 s, 300 s, and 600 s.

Figure 4.2 shows the water contact angle between the untreated COP substrate and 60, 300, and 600 s of VUV light irradiation respectively. The untreated COP substrate surface showed a hydrophobic surface of more than 90 degrees, but the COP substrate irradiated with VUV light for more than 60 seconds reduced the contact angle to approximately 20 degrees.

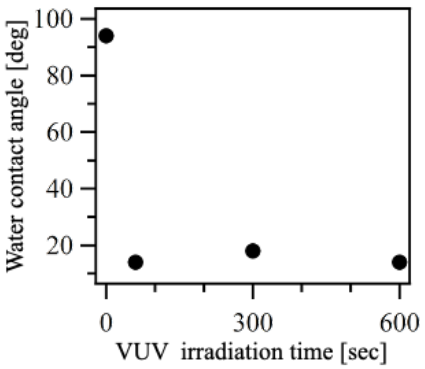

Figure 4.2 Water contact angle of untreated and VUV light irradiated COP substrates for 60 s, 300 s, and 600 s.

The contact angles to water and ethylene glycol were measured for the untreated COP substrate and the COP substrate irradiated with VUV light for 2 seconds, and the surface free energy was calculated based on Owens-Wendt theory [13].

Table 4.1. Surface free energy of COP substrate calculated by Owens–Wendt theory from contact angle.

COP substrate	Surface free energy（mJm^{-2}）		
	Dispersion	Polar	Total
Untreated	14	3	17
VUV light irradiated for 2 sec	12	43	55

Table 4.1 shows the surface free energy of the untreated COP substrate and the 2-s-VUV light-irradiated COP substrate calculated based on Owens-Wendt theory. The VUV light irradiation increased the surface free energy, which was attributed to the increase in polar components of COP surface. Based on previous reports, it was considered that polar functional groups such as hydroxy and carboxyl groups were formed on the COP substrate surface by VUV light irradiation.

Figure 4.3 shows AFM surface images (3×3 μm^2) and the surface RMS roughness of the ZnO thin films grown on the untreated and VUV-light-pretreated COP substrates. The surface RMS roughness was found to decrease from about 3.0 nm for the film grown on the untreated substrate to about 0.6 nm for the film grown on the VUV-light-pretreated substrate, suggesting reflection of the decreased surface roughness for the VUV-light-pretreated COP substrate surfaces as shown in Figure 4.1.

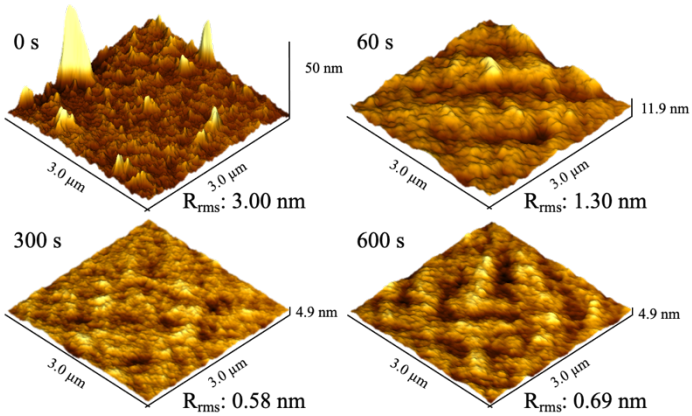

Figure 4.3 AFM images of ZnO thin films grown on untreated and VUV light pretreated COP substrates for 60 s, 300 s, and 600 s.

Figure 4.4 shows the XRD and RHEED (inset) patterns of the ZnO thin films grown on the untreated and VUV light pretreated COP substrates. The peaks attributed to ZnO (100) and ZnO (002) were observed at about 31.6º and 34.0º, respectively, on the untreated COP substrate. Polycrystalline randomly oriented ZnO thin films were grown on untreated COP substrates, as seen in the peaks attributed to multiple crystal planes of ZnO. This randomly orientation was also confirmed via the ring pattern in RHEED of the ZnO thin film on the untreated COP substrate.

On the other hand, the ZnO (100) peaks were not present in the ZnO thin films grown on the COP substrate pretreated with VUV-light for 60 to 600 s, and the only ZnO (002) peaks were observed. Furthermore, the RHEED patterns of the ZnO thin films grown on the VUV light pretreated COP substrates were seen to be not ring pattern but slightly streaky spot pattern. The c-axis oriented growth of the ZnO thin films was obtained on the VUV light pretreated COP substrates from XRD and RHEED measurement. The improvement in the crystallinity of the ZnO thin films grown on the VUV light pretreated COP substrates was thought to be caused in part by the smoothness of the surface of the VUV light pretreated COP substrates as shown in Fig. 4.1. The comparatively rough

surface of the untreated COP substrate may induce inhomogeneous nucleation and polycrystalline growth of the ZnO thin film However, the smooth surface on the VUV light pretreated COP substrates may contribute to the homogeneous nucleation of the ZnO thin films and thus promote the c-axis orientated growth [14].

The XRD integrated intensity of the ZnO (002) peak was found to increase with increasing with VUV-light pretreatment time. The XRD intensity of ZnO (002) peak on the film grown on the 300-s-VUV-pretreated COP substrate was approximately twice that of the sample grown on the untreated substrate, and its full width at half maximum (FWHM) value decreased from 0.9º to 0.6º. These XRD results indicate that the VUV-light pretreatment onto the COP substrates leads to a significant improvement of crystallinity of the ZnO thin films as well as an enhancement of c-axis oriented growth.

The crystallite sizes estimated from the Scherrer's equation were 9 nm and 15 nm on the ZnO thin film on the untreated COP substrate and on the 300-s-VUV-light-pretreated COP substrate, respectively [15]. A decrease in integrated intensity and a slight increase in FWHM value were confirmed on ZnO thin film on COP substrates pretreated for longer than 300 s. This behavior was similar to that reported previously for O_2 plasma pretreatment and would be due to degradation of the COP substrate surface into low molecular weight fragments caused by excessive surface pretreatment [4,5].

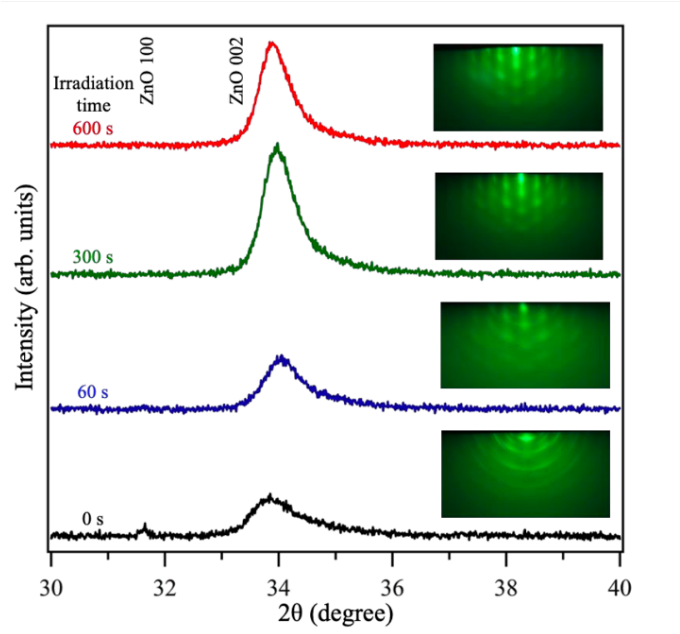

Figure 4.4 XRD 2θ/θ profiles and RHEED patterns (inset) of ZnO thin film grown on the untreated and the VUV-light-pretreated COP substrate.

Reciprocal space mapping with an XRD 2D-detector was performed to investigate the orientation of c-axis oriented ZnO thin films grown on VUV light-pretreated COP substrates. Figure 4.5 shows the reciprocal space maps (RSMs) of ZnO thin films grown on (a) untreated and (b) 300-s-VUV-light-pretreated COP substrates. Only the ZnO 002 diffraction was observed in ZnO thin films on both substrates. The not present of the peak attributed to ZnO (100) identified in Figure 4.4 may be due to differences in irradiation area of x-ray and optical system. The contrast of ZnO 002 diffraction of the ZnO thin film on the VUV-light-pretreated COP substrate was clearly strong and the dispersion is small.This was indicated the improved crystallinity and orientation.

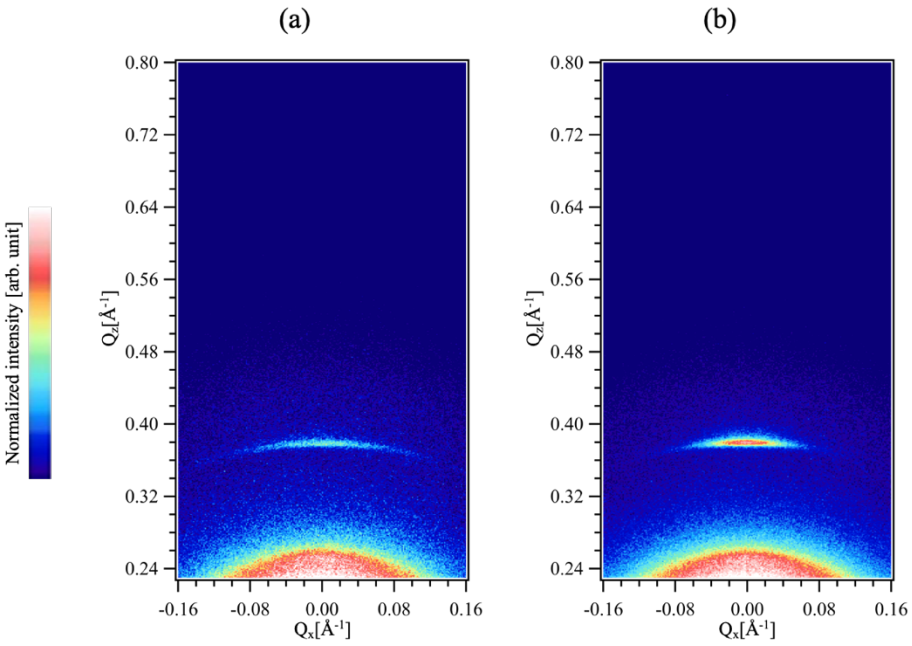

Figure 4.5 Reciprocal space maps of ZnO thin films on (a) untreated and (b) 300-s-VUV-light-pretereated COP substrates.

The χ-rocking curve of the ZnO thin film was introduced from the ZnO *0002* diffraction of the RSMs to evaluate the orientation of the film on the COP substrate. Figure 4.5 shows the χ-rocking curve results for ZnO thin films grown on untreated COP substrates and 300-s-VUV-light-pretreated COP substrates. The FWHM values were 17.9° for the ZnO thin film on the untreated COP substrate and 12.3° on the 300-s-VUV-light-pretreated COP substrate. The orientation of ZnO thin film grown on VUV-light- pretreated COP substrate was improved by about 32%. Considering that the reduction of the rocking curve FWHM of the ZnO thin film on the COP substrate with only the surface flatness improved

in Chapter 3 was about 20%, it was suggested that the VUV light pretreatment improved the orientation by about 12% by improving the crystallinity of the ZnO thin films.

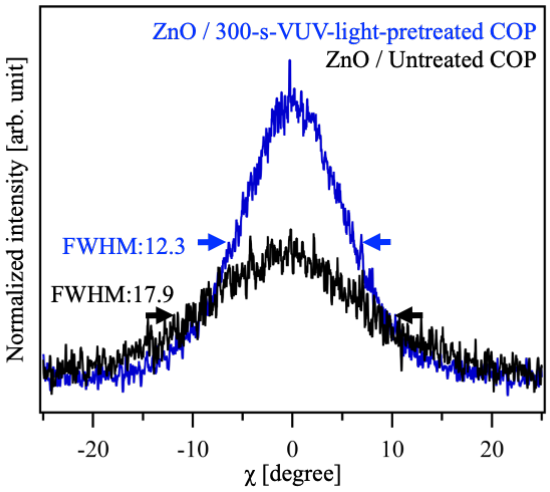

Figure 4.6 XRD rocking curves of ZnO 0002 diffraction for the films on untreated and 300-s-VUV-light-pretereated COP substrates.

Figure 4.7 shows a cross-sectional transmission electron microscope (TEM) images of ZnO thin films grown on (a) untreated COP substrate and (b) 300-s-VUV-light-pretreated COP substrate and a selected area electron diffraction (SAED) image (area with a radius of about 200 nm from the film center) in the inset. The electron diffraction spots attributed to ZnO (002) seen in the SAED images of ZnO thin films on both COP substrates of inset of Figure 4.7 indicated c-axis oriented growth of the ZnO thin film perpendicular to the COP substrate surface. This was consistent with the results of the RSMs measured by XRD. The ZnO thin film on the VUV-light-pretreated COP substrate was adhered to COP substrate during thinning with a focused ion beam, whereas the film on the untreated COP substrate was occurred peeling. This was presumably related to possible physicochemical bonds between the oxygen-containing polar functional groups and the ZnO crystal nuclei formed on the surface of the COP substrate pretreated with VUV light in air [16].

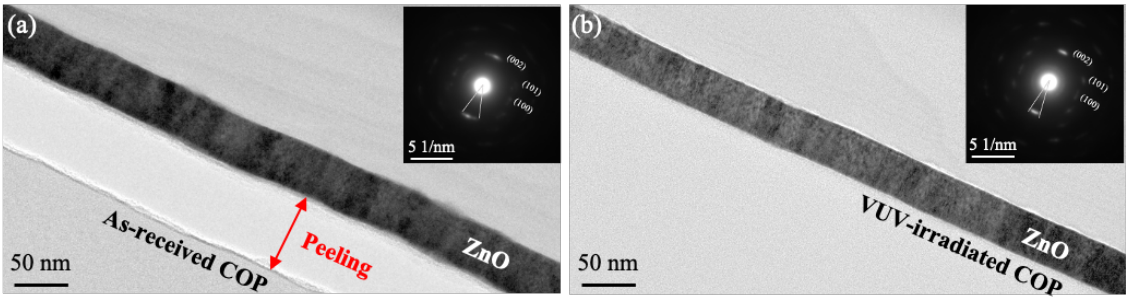

Figure 4.7 Cross-sectional TEM images of ZnO thin films grown on (a) untreated COP and (b) 300-s-VUV-light-pretreated COP substrates, inset shows a selected area electron diffraction (SAED) images (area with a radius of about 200 nm from the film center).

Figure 4.8 shows a high magnification cross sectional TEM image of a ZnO thin films grown on an untreated COP substrate and 300-s-VUV-light-pretreated COP substrate. Note that the film on the untreated COP substrate could not be thinned to the same degree as the sample of VUV-light-pretreated COP substrate due to low bonding. A regular lattice image attributed to ZnO (0001) was observed extending in the out-of-plane direction from near the interface of the COP substrate. This indicated that the ZnO thin film was grown with crystallized growth from the initial growth stage at RT. The lattice images of ZnO thin film grown on the VUV-light-pretreated COP substrate was clearly aligned, suggesting that the surface modification improved the crystal growth of the ZnO thin film from the initial growth stage.

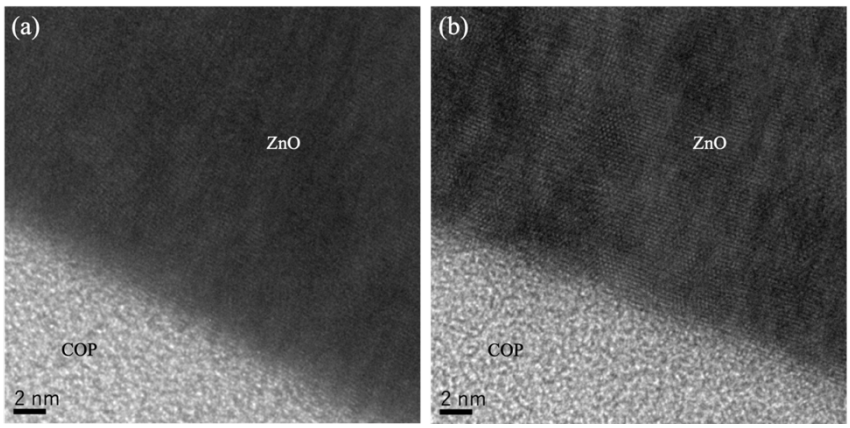

Figure 4.8 High magnification cross-sectional TEM images of ZnO thin films grown on untreated COP and 300-s-VUV-light-pretreated COP substrates.

The polar growth of ZnO thin films grown in the c-axis orientation was evaluated. Figure 4.9 shows X-ray Photoelectron Spectroscopy (XPS) spectra of around the valence band of ZnO thin films grown on untreated COP and 300-s-VUV-light-pretreated COP substrates [17-19]. The polarity of the wurtzite type including ZnO, was determined by XPS analysis of the subpeaks near the valence band. Each XPS profile was fitted with a Gaussian function. The subpeaks appearing around 4.5 eV and 7.3 eV are thought to correspond to the Zn-face: (0001) and O-face: $(000\bar{1})$, respectively. The polarity of the samples was often determined by simply comparing the intensities of these two peaks but was also complemented by comparing the areas determined by Gaussian fitting [17-19]. The subpeak around 4.5 eV was more intense and had a larger fitted area. The results indicated that under the growth conditions of this study, the Zn-face; (0001) was the dominant of growth orientation of ZnO thin films, regardless of the surface modification of the COP substrate.

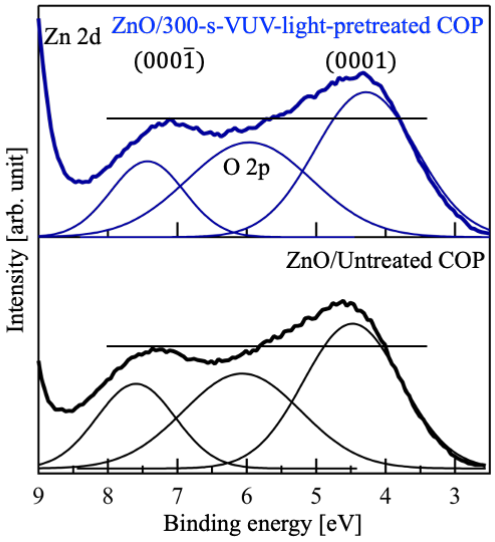

Figure 4.9 XPS spectra of around the valence band of ZnO thin films on untreated COP and 300-s-VUV-light-pretreated COP substrates.

Time-of-Flight secondary ion mass spectrometry (ToF-SIMS) depth analysis was performed to analyze the chemical state of ZnO thin films and COP substrates. Figure 4.9 shows the TOF-SIMS sputtering time profile for cations and anions, respectively, of ZnO thin films grown on untreated and VUV-light-pretreated COP substrates. Figure 4.10 shows the ToF-SIMS sputtering time profile for cations and anions, respectively, of ZnO thin films grown on untreated and 300-s-VUV-light-pretreated COP substrates. No

interdiffusion layers were confirmed between the ZnO thin films and the COP substrates for either ion on both substrates. Although there was no difference in the chemical states of the two ZnO films, the O^--counts in substrate side were clearly higher on the VUV-light-pretreated COP substrate, suggesting that oxygen-containing functional groups were formed due to VUV light irradiation in air. The counts remained higher than those of untreated COP substrates even at sputtering times longer than 150 seconds, suggesting that the oxygen-containing layer was formed to some depth [20]. This suggested that the introduction of polar functional groups near the surface of the COP substrate by VUV-light surface modification had an effect on the crystal growth of the ZnO thin film.

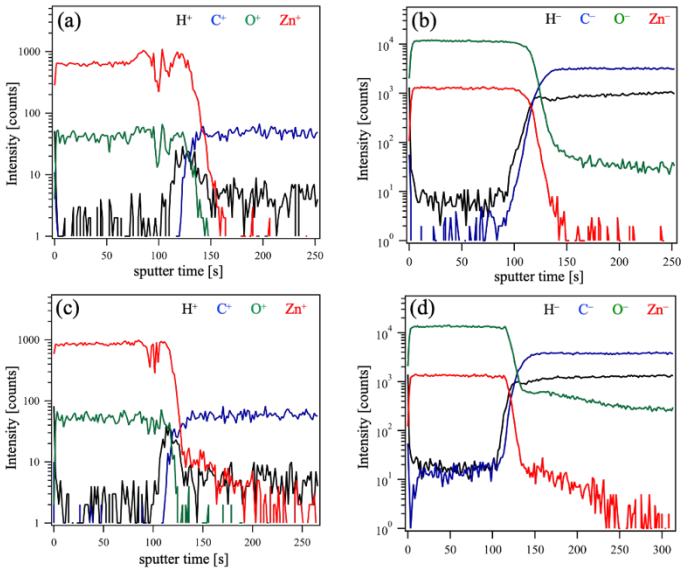

Figure 4.10 ToF-SIMS sputter time profiles of (a) cations and (b) anions of ZnO thin films grown on untreated COP substrates and (c) cations and (d) anions of ZnO thin films on 300-s-VUV-light-pretreated COP substrate.

Optical properties were characterized by UV/vis transmittance measurements. Figure 4.11 shows the optical transmittance spectra and the Tauc plot obtained from around the absorption edge of the ZnO thin films grown on the untreated and 300-s-VUV-light-pretreated COP substrate. The transmittance in the visible light region is about 70%–80 % at 400 nm and about 90% at 700 nm for the films on both substrates. Both optical bandgaps of the ZnO thin films were estimated to be about 3.3 eV, which was close to the previously reported values [21,22], although the bandgap of the ZnO thin film on the 300-s-VUV-light-pretreated substrate seems to be slightly larger. This would be related to the improved crystallinity of the ZnO thin film grown on the VUV-light-pretreated COP substrate compared with that grown on the untreated COP substrate in Figure 4.4.

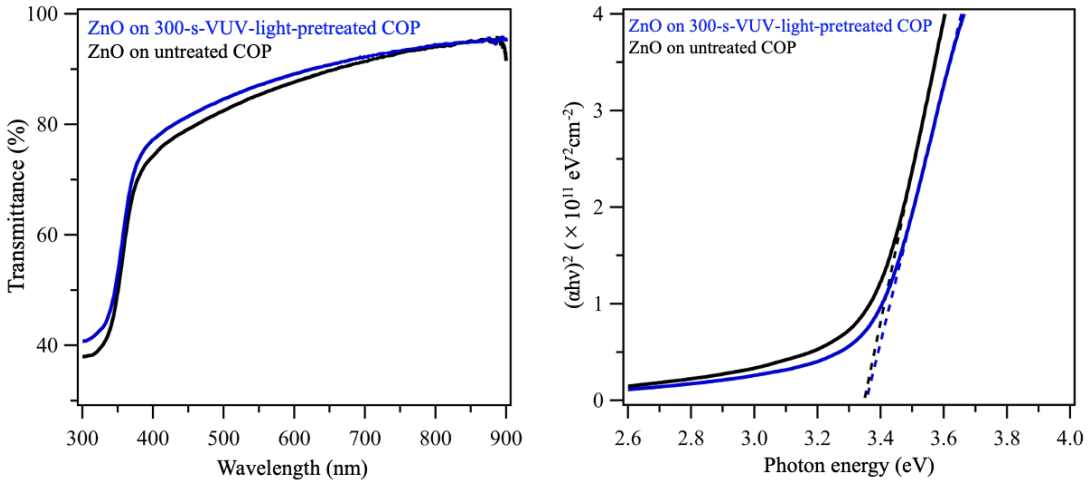

Figure 4.11 The optical transmittance spectra and the Tauc plot obtained from around the absorption edge of the ZnO thin films grown on the untreated and 300-s-VUV-light-pretreated COP substrate.

Table 4.2 shows electric properties of the ZnO thin films grown on the untreated and 300-s-VUV-light-pretreated COP substrates estimated from the van der Pauw-type Hall effect measurements at RT in air. The ZnO thin film grown on the 300-s-VUV-light-pretreated COP substrate has the about 40% reduced resistivity, about 60 % increased Hall mobility, and about 8 % increased carrier concentration compared to the ZnO thin film on untreated COP substrate. So that, the present decrease in resistivity is thought to be primarily caused by an increase in the Hall mobility, which could be induced by an increase in the crystallinity of the ZnO thin film grown on the VUV-light-pretreated COP substrate, that is, about 67% increase in the estimated crystallite size of ZnO thin film on

the 300-s-VUV-light-pretreated COP substrate, which leading to the decreased grain-boundary scattering of electron carriers, as mentioned above in the section of Fig. 4.3[23]. Thus, VUV-light pretreatment of the COP substrate resulted in the improved ZnO film crystallization with the larger crystallite size, leading to an increase of Hall mobility.

Table 4.2 Electric properties of the ZnO thin films grown on the untreated and 300-s-VUV-light-pretreated COP substrates estimated from the van der Pauw-type Hall effect measurements at RT.

Film sample	Resistivity (Ωcm)	Hall mobility ($cm^2V^{-1}s^{-1}$)	Carrier concentration (cm^{-3})
ZnO thin film on untreated COP	3.87×10^{-3}	7.54	2.14×10^{20}
ZnO thin film on 300-s-VUV-light-pretreated COP	2.27×10^{-3}	11.86	2.32×10^{20}

4.4 Summary

In this study, the effect of VUV-light irradiation onto the COP substrate for surface modification of polymer substrate on the crystal growth of the ZnO thin films via PLD at RT. The VUV-light irradiation in air modified the COP substrate surface hydrophilic and smooth. The ZnO thin films grown on the VUV-light-pretreated COP substrates exhibited an enhanced (0001) orientation growth and crystallinity improvement, as well as atomically sharp interface between the film and the substrate, from XRD, RHEED and TEM analyses. The electrical resistivity of the ZnO thin film grown on the VUV-light-pretreated COP substrate was estimated at RT from van der Pauw-type Hall effect measurements to be 2.3×10^{-3} Ωcm, this value is 40% smaller than that of the films grown on the untreated substrates, which might be related to the improvement of crystallinity of the film grown on the pretreated COP substrates, as well as the associated increase in Hall mobility of the sample.

Reference

[1] W.A. MacDonald, J. Mater. Chem.,14 (2004) 4–10.

[2] S.K. Nemani, R.K. Annavarapu, B. Mohammadian, A. Raiyan, J. Heil, M.A. Haque, A. Abdelaal, H. Sojoudi, Adv. Mater. Interfaces, 14, 1801247 (2018).

[3] B.-G. Kim, J.-Y. Kim, S.-J. Lee, J.-H. Park, D.-G> Lim, M.-G. Park, Appl. Surf. Sci., 257 (2010) 1063–1067.

[4] J.H. Heo, H. Ryu, W.-J. Lee, J. Ind. Eng. Chem., 19, (2013) 1638–1641.

[5] C.-C. Chen, F.-H. Wang, S.-C. Chang, C.-F. Yang, Materials, 11, 1501 (2018).

[6] J-S. Park, H. Chae, H. K. Chung, S.I. Lee, Semicond. Sci. Technol. 26, 034001 (2011).

[7] H. Shinohara, J. Mizuno, S. Shoji, Sens. Actuator. A Phys., 165 (2011) 124–131.

[8] Y.-J. Kim, Y. Taniguchi, K. Murase, Y. Taguchi, H. Sugimura, Appl. Surf. Sci., 255 (2009) 3648–3654.

[9] K. Watanabe, M. Zelikoff, J. Opt. Soc. Am., 43 (1953) 753755.

[10] E.A. Sosnin T. Oppenländer, V.F. Tarasenko, J. Photochem. Photobiol. C, 7 (2006) 145–163.

[11] A.C. Fozza, J.E. Klemberg-Sapieha, M.R. Wertheimer, Plasmas. Polym., 2, (1999) 183–206.

[12] M. Gonda, T. Utsunomiya, T. Ichii, H. Sugimura, Int. J. Adhes. Adhes., 100, 102604 (2020).

[13] D.K. Owens, R.C. Wendt, J. Appl. Polym. Sci., 13, (1969) 1741–1747.

[14] T. Oga, S. Yamada, N. Kaneko, S. Kaneko, A. Matsuda, M. Yoshimoto, Jpn. J. Appl. Phys. 59, 128001 (2020).

[15] B.D. Cullity, Elements of X-ray Diffraction, 2nd ed., Addison Wesley, Reading, MA, (1978) pp. 102.

[16] C. Wang, X. Qi, Y. Wang, B. Wu, Y. Tian, J. Electrochem. Soc., 165 (2018) B3091–B3097.

[17] J.R. Williams, H. Furukawa, Y. Adachi, S. Grachev, E. Søndergård, N. Ohashi, Appl. Phys. Lett., 103, 042107 (2013).

[18] R. Heinhold, M.W. Allen, J. Mater. Res., 27 (2012) 2214–2219.

[19] M.W. Allen, D.Y. Zemlyanov, G.I.N. Waterhouse, J.B. Metson, T.D. Veal, C.F. McConville, S.M. Durbin, Appl. Phys. Lett., 98, 101906 (2011).

[20] S. Horiuchi, H. Hakukawa, Y.J. Kim, H. Nagata H. Sugimura, Polym. J., 48 (2016) 473–479.

[21] S.-M. Park, T. Ikegami, K. Ebihara, Thin Solid Films 513 (2006) 90–94.

[22] V. Srikant, D.R. Clarke, 5448 J. Appl. Phys., 83 (1998) 5447–5451.
[23] T. Minami, Semicond. Sci. Technol., 20 (2005) S35–S44.

Chapter 5

Effect of insertion of oxide buffer layer onto polymer substrates on crystal growth and properties of ZnO thin films

5.1 Introduction

Amorphous oxide buffer layers were introduced as buffers to improve adhesion to the polymer substrate and prevent inter-diffusion, when forming crystal oxide thin films on polymer substrates [1,2]. On the other hand, there are not many reports on the effect of the formation of such oxide buffer layers on the crystal growth of oxide thin films. In general, oxides have higher surface free energies than polymer materials, which may affect thin film growth during the nucleation process [3]. Although ZnO thin films are known to preferentially grow in the c-axis orientation even on amorphous substrates, their crystallinity and electrical and optical properties are inferior compared to growth on oxide substrates [4-6]. The crystallinity and orientation of ZnO thin films could be improved by forming an appropriate oxide buffer layer.

5.2 Experiment

The following two techniques were used in the formation of the oxide buffer layer in this study. The amorphous and polycrystal oxide buffer layers were formed on the cyclo-olefin polymer (COP) substrates by PLD using KrF excimer laser (λ= 248 nm, laser fluence= 1.2 Jcm^{-2}) with a sintered and single crystal target at RT without intentionally heating. The O_2 gas pressure was fixed at 1.0×10^{-3} Pa, and target-substrate distance was located at 5 cm.

The β-Ga_2O_3 single crystal was selected as the single-crystal buffer formation. β-Ga_2O_3 is monoclinic structure and has cleavage planes in the crystal [7]. β-Ga_2O_3 single crystal buffers were simply exfoliated from a commercial β-Ga_2O_3 (100) single crystal substrate (Adamant Namiki Precision Jewel Co., Ltd. / Novell Crystal Technology Co.) by the tape-method using commercial Scotch-tape and bonded in air to a COP substrate that was surface modified by VUV light irradiation (λ=172 nm, E~65 mW/cm^2, d~2 mm, EX-mini, HAMAMATSU PHOTONICS K.K.).

Subsequently, the ZnO thin films were grown on the COP substrates with or without oxide buffers by PLD using KrF excimer laser (λ = 248 nm, laser fluence = 1.2 Jcm^{-2}) with a sintered ZnO target (99.99%) at RT without intentionally heating. The O_2 gas pressure was fixed at 1.0×10^{-3} Pa, and target-substrate distance was located at 5 cm.

The surface morphology of the samples was observed by atomic force microscopy (AFM; Nanocute/Nanonavi, Hitachi High-Tech Science Corp.) operated in the contact mode. The crystal structure of the thin films was characterized by X-ray diffraction (XRD; Smart lab and RINT-2100V, Rigaku Corp.) and reflection high energy electron diffraction (RHEED; Pascal Corp.). The orientation of ZnO thin films was evaluated by reciprocal space mapping using point focused x-rays with Cu target on an XRD system (Smart Lab, Rigaku) equipped with a two-dimensional detector (PILATUS 100 K/R, Rigaku). The polarity of the ZnO films was determined by X-ray photoelectron spectrometer (XPS; AXIS Supra, Shimadzu corp.). The optical transmittance of ZnO thin film on the COP sheet was measured using a UV/vis spectrophotometer (V-550, JASCO Corp.). The electrical properties of the ZnO thin film grown on amorphous buffer layer was evaluated at RT in air under a magnetic field of 0.4 T using a van der Pauw-type Hall effect measurement system (HEMS-MD-S-30, Seinan Industry Co., Japan), and measured using the conventional four terminal method (Model 2750 Multimeter/Switch System, Keithley) of the film grown on single-crystal buffer layer.

5.3 Results and discussion

5.3.1 Effect of insertion of amorphous and polycrystal buffer layer

Figure 5.1 shows XRD 2θ/θ profiles of ZnO thin films on untreated and oxide buffered COP substrates. The integrated intensity of ZnO *0002* diffraction was clearly increased when AlO_x, GaO_x, and TiO_x were used as buffers, but decreased when MgO_x and CeO_x were used, compared to the film on without buffer layer. The formation of oxide buffers was suggested to have both positive and negative effects on the crystal growth of ZnO thin films on polymer substrate. Among the buffer layers with enhanced integrated intensity of diffraction of ZnO *0002*, AlO_x and GaO_x were more effective than TiO_x. The larger surface free energy of the buffer layer, estimated from the surface free energy of each crystalline layer, although the actual value is different because the buffer layer is amorphous, or the introduction of a cation with a small difference in electronegativity from Zn as ZnO, a strongly ionic crystal, may have carried the effect on crystal growth of ZnO thin films [8-12].

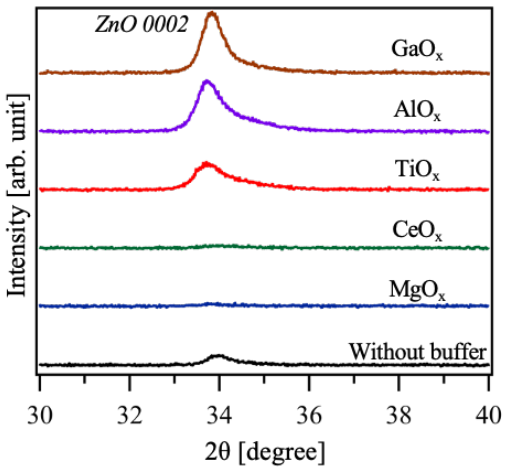

Figure 5.1 XRD 2θ/θ profiles of ZnO thin film grown on COP substrates with or without oxide buffers.

The effect of the oxide buffer layer on the crystal growth of the ZnO thin film was identified by XRD reciprocal space mapping. Figure 5.2 shows the reciprocal space maps (RSMs) of ZnO thin films on the GaO_x buffer layers of thicknesses of 1, 10, and 100 nm, respectively, which showed effects to improve the crystal growth of ZnO thin film in Figure 5.1. The GaO_x buffer was found to be amorphous since no diffraction peaks

attributed to gallium oxide were identified at any film thickness. The ZnO *0002* peaks on the amorphous GaO_x buffer show stronger contrast and smaller dispersion as the thickness increases. The same results of effect on crystal growth of ZnO thin films were obtained when AlO_x was used as a buffer. This was suggested the certain thickness of the amorphous oxide buffer was necessary for improved crystallinity and orientation of the ZnO thin film.

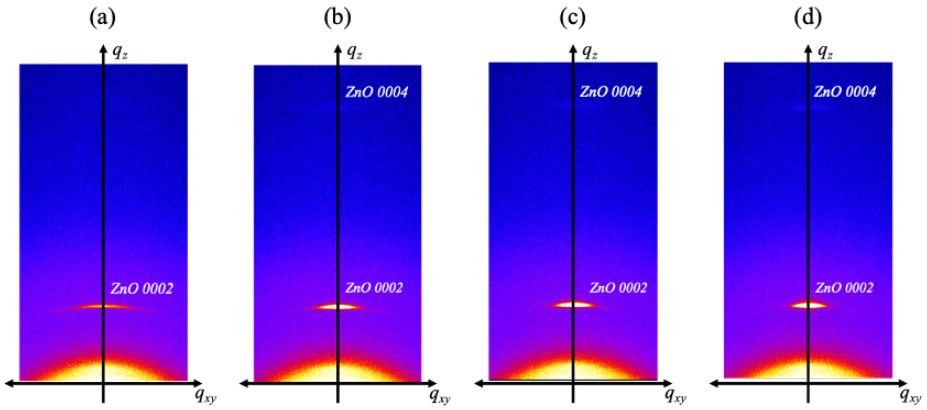

Figure 5.2 Reciprocal space maps of ZnO thin films on COP substrates with (a) no buffer, (b) 1 nm (c) 10 nm, and (d) 100 nm thick GaO_x buffer layer.

Figure 5.3 shows the RSMs of ZnO thin films on the CeO_x buffer layers of thicknesses of 1, 10, and 100 nm, respectively, which showed effects to inhibite the crystal growth of ZnO thin film in Figure 5.1. The peak intensity of the ZnO *0002* film was enhanced on a 1 nm thick cerium oxide buffer, but it was dispersed on the buffers that thickness was more than 10 nm. The non-oriented diffraction peak attributed to CeO_2 was also observed when the cerium oxide buffer thickness was more than 10 nm. The c-axis orientation of the ZnO thin film was decreased with the appearance of the crystalline layer of the CeO_2 buffer. The similar degree of dispersion in the orientation of the CeO_2 *111* diffraction of buffer and the ZnO 0002 diffraction of film was suggested that the ZnO thin film inherited the crystal growth of non-oriented crystalized cerium oxide buffer.

In the case where MgO was investigated for the buffer layer, a clear ring pattern due to the non-oriented crystallized layer was observed in the RHEED observation for a MgO film of about 50 nm as well, although it could not be observed for a 10 nm film due to charging of the sample.

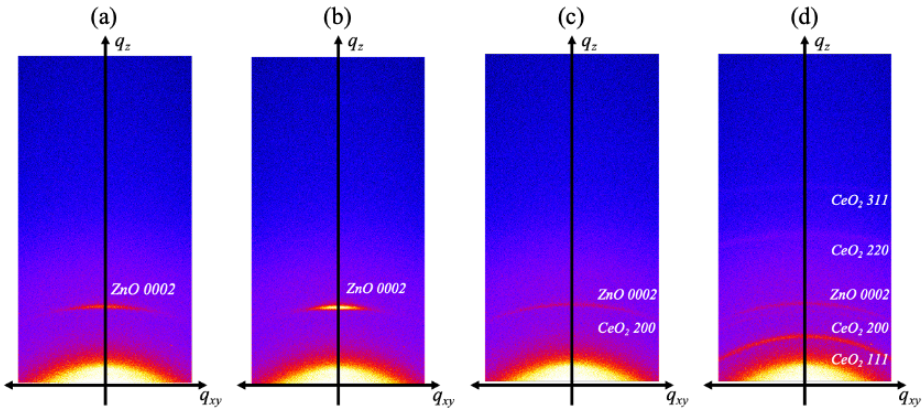

Figure 5.3 Reciprocal space maps of ZnO thin films on COP substrates with (a) no buffer, (b) 1 nm (c) 10 nm, and (d) 100 nm thick CeO_x buffer layer.

The effect of 100 nm thick GaO_x and AlO_x buffers on the crystallinity of ZnO thin films, which are considered to be most effective in improving the crystal growth of ZnO thin films from the results of Figures 5.1 and 5.2 was examined. Figure 5.4 shows the XRD 2θ/θ profile of the ZnO thin film with AlO_x or GaO_x buffer layers of 100 nm and without buffer layers. The integrated intensity of the ZnO *0002* peak increased about 7 times compared with the case of not inserting the buffer layer. The full width at half maximum (FWHM) is also reduced to 0.71° without the buffer layer and 0.56° and 0.53° with the GaO_x and AlO_x buffer layers, respectively. These XRD results indicated that the insertion of an amorphous buffer layer on the COP substrate significantly improved the crystallinity of the ZnO thin film and promoted the c-axis oriented growth. In addition, the formation of the AlO_x buffer layer was advantageous for the oriented crystal growth of the ZnO thin film, although it was slight. Since both buffer layers are amorphous from the XRD results, it was thought that the difference in surface chemical state slightly affects the crystallinity of the ZnO thin film as mentioned in the results of Figure 5.1.

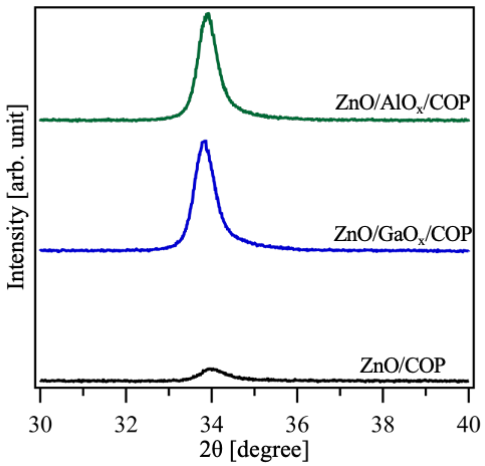

Figure 5.4 XRD 2θ/θ profiles of ZnO thin films grown on COP substrates with AlO_x or GaO_x buffer layers of 100 nm and without buffer layers.

Reciprocal space mapping was performed to investigate the effect of amorphous oxide buffer on orientation of ZnO thin films. Figure 5.5 shows the RSMs of ZnO thin films grown on (a) untreated and (b) AlO_x (t~100 nm) buffered COP substrates. The only diffraction of ZnO *0002* was observed in the ZnO thin films on both substrates, but it was clearly different with respect to its spread. As you can see, the crystal growth of the ZnO thin film was clearly improved.

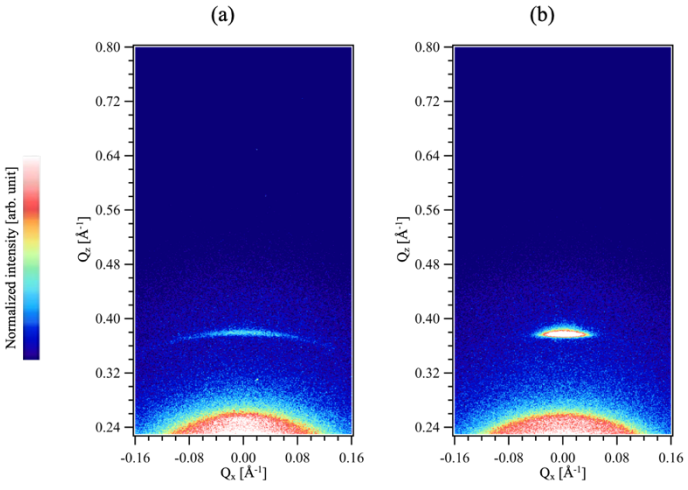

Figure 5.5 Reciprocal space maps of ZnO thin films grown on (a) untreated and (b) AlO_x buffered COP substrates.

The χ-rocking curve of the ZnO thin film was introduced from the ZnO *0002* diffraction of the RSMs to evaluate the orientation of the film on the COP substrate. Figure 5.6 shows the χ-rocking curve results for ZnO thin films grown on untreated and AlO_x buffered COP substrates. The FWHM values were 17.9° for the ZnO thin film on the untreated COP substrate and 6.7° on the AlO_x buffered COP substrate. The effect of AlO_x buffer formation on the orientation of ZnO thin films grown on COP substrates was shown to be more effective than the direct surface modification of COP substrates by the surface flattening and formation of polar functional groups in Chapters 3 and 4. This might be occurred due to surface free energy, oxygen content, or affinity between oxides [2].

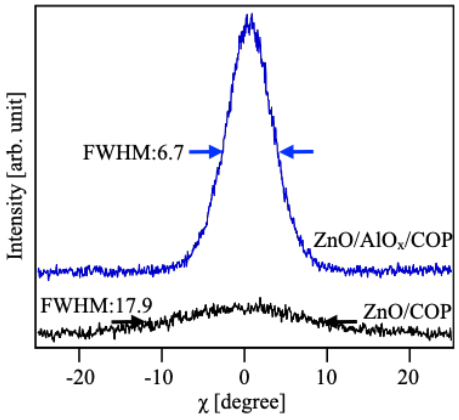

Figure 5.6 XRD rocking curves of ZnO *0002* diffraction for the films on untreated and AlO_x buffered COP substrates.

The polar growth of ZnO thin films grown in the c-axis orientation was evaluated. Figure 5.7 shows x-ray Photoelectron Spectroscopy (XPS) spectra of around the valence band of ZnO thin films grown on untreated COP and AlO_x buffered COP substrates. The subpeak presented around 4.5 eV was correspond to the Zn-face (0001) [13,14]. Even with AlO_x buffer insertion, the crystal growth of ZnO thin film deposited these conditions was a Zn-face (0001) orientation.

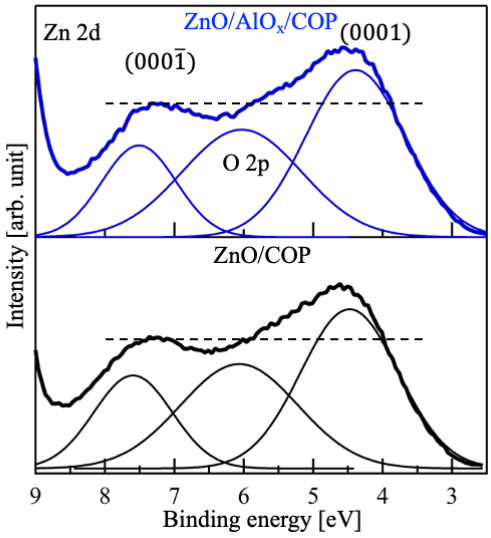

Figure 5.7 XPS spectra of around the valence band of ZnO thin films on untreated COP and AlO_x buffered COP substrates.

Figure 5.8 shows AFM surface images (3×3 μm^2) and the root-means-square (RMS) surface roughness of the ZnO thin films grown on the untreated and AlO_x buffered COP substrates. The surface roughness was found to decrease from about 3.0 nm in the case of the sample grown on the untreated substrate to about 0.7 nm for the sample grown on the alumina buffered substrate. The alumina buffer onto the COP substrates was thought to promote nucleation of the ZnO thin film, resulting in high-density nucleation and improved surface flatness [15].

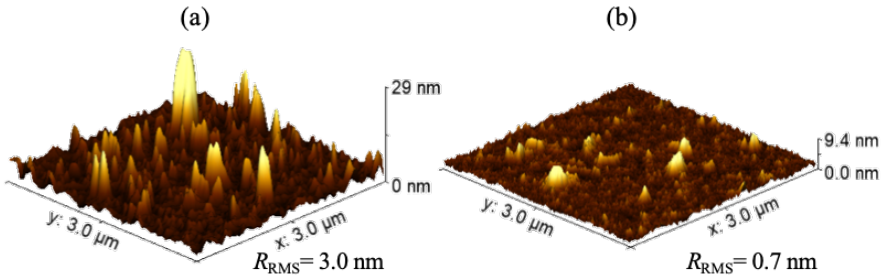

Figure 5.8 AFM images of ZnO thin films grown on untreated and AlO_x buffered COP substrates.

Table 5.1 shows electric properties of the ZnO thin films grown on the untreated and AlO_x buffered COP substrates estimated from the van der Pauw-type Hall effect measurements at RT. The ZnO thin film grown on the AlO_x buffered COP substrate has the about 34% reduced resistivity, about 29 % increased Hall mobility, and about 80 % increased carrier concentration compared to that on untreated COP substrate. The increased crystallinity of the ZnO thin film grown on AlO_x buffered COP substrate shown in Figure 5.4 was thought to have contributed to the increase in Hall mobility by reducing the scattering of electron carriers at grain boundaries. On the other hand, considering that the diffusion of buffer elements into the film was unlikely to occur at RT deposition, the improvement of carrier concentration of ZnO thin film might be due to improved orientation. This phenomenon was required further investigation.

Table 5.1 Electric properties of the ZnO thin films grown on the untreated and AlO_x buffered COP substrates estimated from the van der Pauw-type Hall effect measurements at RT.

Film sample	Resistivity (Ωcm)	Hall mobility ($cm^2V^{-1}s^{-1}$)	Carrier concentration (cm^{-3})
ZnO thin film on untreated COP	3.87×10^{-3}	7.54	2.14×10^{20}
ZnO thin film on AlO_x buffered COP	2.57×10^{-3}	9.75	3.87×10^{20}

5.3.2 Effect of insertion of single crystal buffer layer

The introduction of a flexible single-crystal oxide buffer layer on polymer substrate, and the effect of a single-crystal oxide buffer layer on the crystal growth of ZnO thin films were investigated. β-Ga_2O_3 sheets were employed as a single crystal oxide buffer layer on a polymer substrate in this study. Figure 5.9 shows AFM images of the surface of (a) cleaved β-Ga_2O_3 (100) single crystal buffer layer on COP substrate and cross-sectional profile along atomic steps and terrace structures, and (b) ZnO thin film grown on COP substrate with β-Ga_2O_3 (100) single crystal buffer layer. The cleavage plane was found to have a flat terrace on the (100) plane and a stepped shape facing the other (001) cleavage plane in figure 5.9 (a) [16]. The ultra-flat surface morphology was obtained with cleavage plane. The minimum height of that step was about 0.6 nm from the cross-sectional profile shown in the white line, which corresponds to a half-unit of β-Ga_2O_3 (100) [7]. These show that a buffer layer of β-Ga_2O_3 with a cleaved flat surface has been formed on the COP substrate. The cleavage surfaces are atomically ordered in alignment which would promote unified polar orientation growth and homogeneous nucleation in initial stage of ZnO thin films. The ZnO thin film grown on the β-Ga_2O_3 buffer layer had an ultra-flat surface, clearly reflecting the atomic step pattern of the buffer of β-Ga_2O_3 (100) shown in figure 5.9 (a).

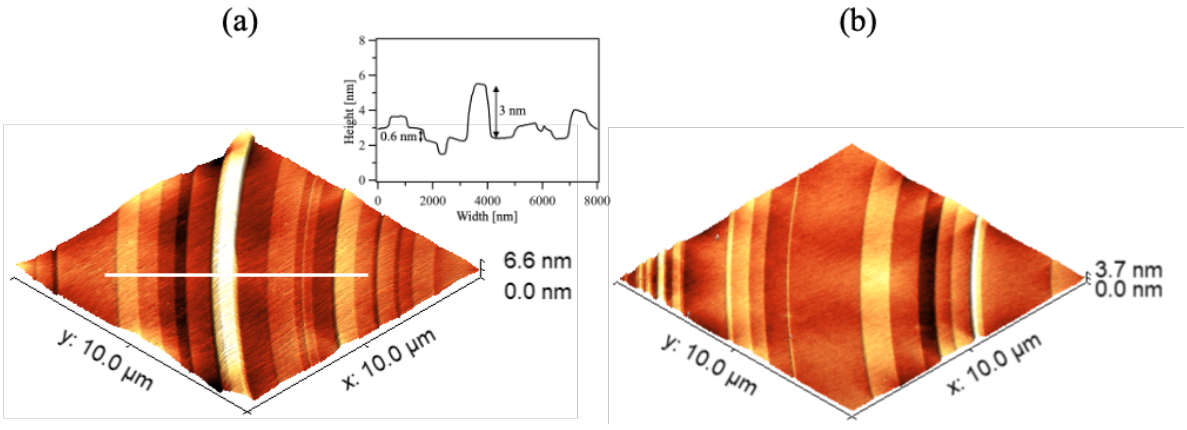

Figure 5.9 AFM images of the surface of (a) cleaved β-Ga_2O_3 (100) single crystal buffer layer on COP substrate and cross-sectional profile along atomic steps and terrace structures, and (b) ZnO thin film grown on COP substrate with β-Ga_2O_3 (100) single crystal buffer layer.

Figure 5.10 shows the XRD 2θ/ω profile and of the ZnO thin film grown on the β-Ga_2O_3 single crystal buffered COP substrates. The peak seen around 20 degrees was the peak attributed to the COP substrate. Only the peak attributed to (100) was observed as the buffer layer of β-Ga_2O_3, that was indicated only the cleaved (100) surface was formed on the substrate surface for β-Ga_2O_3 single crystal buffer prepared by the tape method. The diffraction peaks *0002* and *0004* of the ZnO thin film on the β-Ga_2O_3 single crystal buffer are clearly identified, that was indicated highly c-axis oriented growth. Although the β-Ga_2O_3 buffer layer and ZnO (0001) have different crystalline symmetries, the deposition at RT probably favors c-axis growth, the most stable plane of the wurtzite type. This is similar to the previously reported results for wurtzite-type thin films [17].

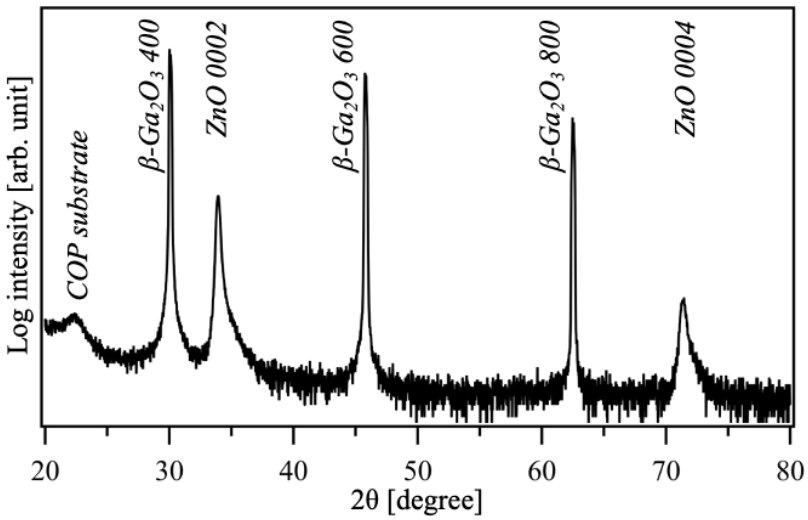

Figure 5.10 XRD 2θ/ω profile of the ZnO thin film grown on COP substrate with β-Ga_2O_3 single crystal buffer layer.

Figure 5.11 shows the XRD phi-scan of the ZnO thin films and β-Ga_2O_3 single crystal buffer layer respectively. The six peaks of the ZnO ($1\bar{1}01$) plane presented every 60°. These XRD patterns indicated that the ZnO thin film grown on β-Ga_2O_3 single crystal buffered COP substrate was epitaxial grown at RT. The two peaks of the β-Ga_2O_3 (420) plane were also shown to be present every 180°. From these results, the epitaxial relationship between the two was ZnO (0001) / β-Ga_2O_3 (100) with ZnO [$11\bar{2}0$] ∥ β-Ga_2O_3 [010] and ZnO [$1\bar{1}00$] ∥ β-Ga_2O_3 [001]. This is due to the alignment of the Ga or O on the top surface of the cleaved β-Ga_2O_3 in rows relative to the opposite sides of a

regular hexagon, which is in good agreement with the (0001) atomic arrangement of ZnO. This is consistent with the results also reported for wurtzite-type film on β-Ga_2O_3 (100) [18].

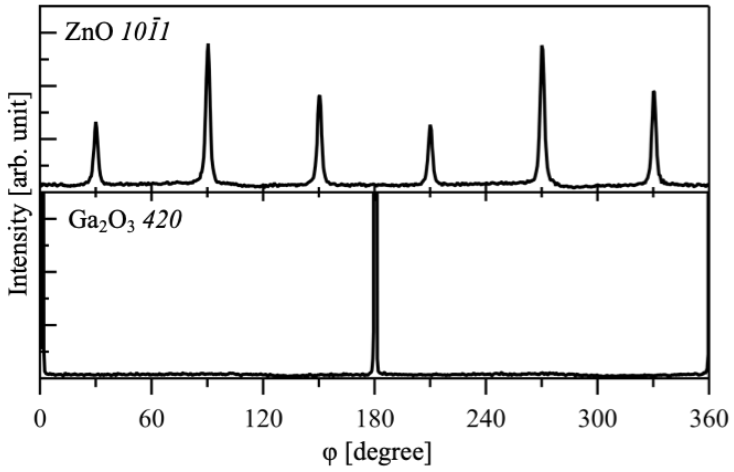

Figure 5.11 XRD phi-scan of the ZnO 1$\bar{1}$01 and β-Ga_2O_3 420 diffractions.

Figure 5.12 shows (a) RSMs of ZnO thin films grown on β-Ga_2O_3 single crystal buffered COP substrates measured by 2D-detector, and (b) rocking curves of ZnO *0002* diffraction. Only diffraction peaks in the out-of-plane direction are present that are attributed to ZnO (0001) and β-Ga_2O_3 (100), consistent with the 2θ/ω scan profile in Fig. 5.10. The arc-like broadening of the peaks in the ZnO *0002* corresponds to dispersion of texture of ZnO thin film. Figure 5.12 (b) shows the χ-rocking-curve profile extracted in arc form from ZnO *0002* diffraction. The FWHM was about 1.7° for the ZnO thin film on COP substrates with the β-Ga_2O_3 single crystal buffer layer. This value was quite small for that on a polymer substrate, which can only be fabricated at low temperatures, and was evident when compared to Figure 5.6. This was also indicated that the texture of the ZnO thin film is highly oriented. The FWHM values comparable to previously reported ZnO thin films on β-Ga_2O_3 at deposited high-temperature was suggested that homogeneous nucleation of ZnO might be occurred due to growth on the ultra-flat surface obtained at the cleavage β-Ga_2O_3 (100) plane shown in Fig. 5.9 [19,20].

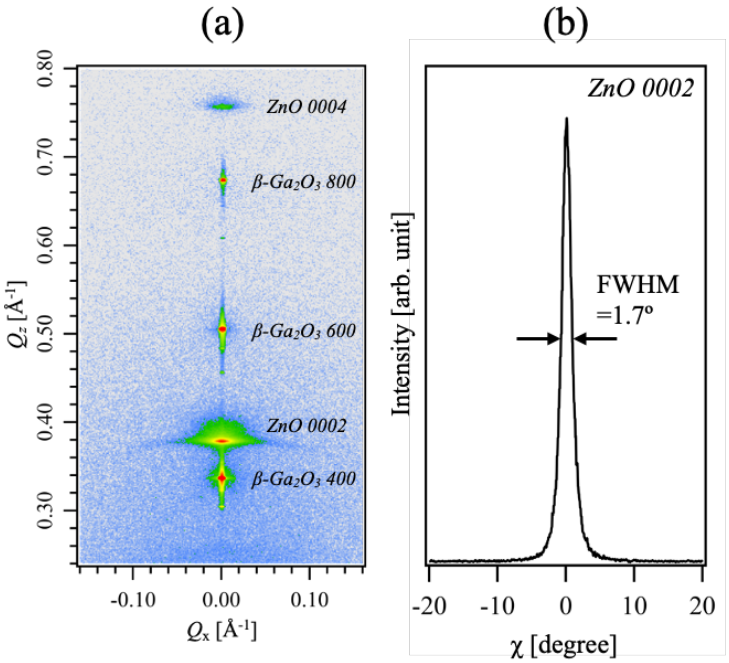

Figure 5.12 (a) RSMs of ZnO thin films grown on β-Ga_2O_3 single crystal buffered COP substrate and (b) rocking curves of ZnO *0002* diffraction.

Figure 5.13 shows the optical transmittance and the Tauc plot obtained from transmittance measurements around the absorption edge of ZnO thin film grown on β-Ga_2O_3 buffered COP substrate. The transmittance of the thin film including the seed layer was more than 80% in the visible light range. The absorption seen from around 400 nm and 280 nm corresponds to the ZnO thin film and β-Ga_2O_3 seed, respectively. The optical band gap of the ZnO thin film is estimated to be about 3.4 eV, close to the bulk value, which is due to the high crystallinity of the ZnO thin film [21,22].

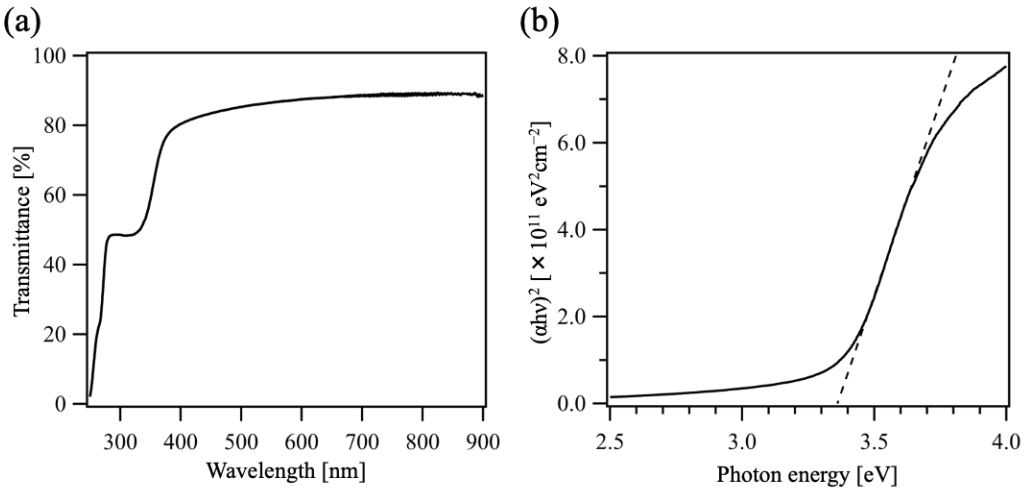

Figure 5.13 (a) optical transmittance spectra and (b) the tauc plot obtained from transmittance measurements around the absorption edge of the ZnO thin films grown on β-Ga_2O_3 single crystal buffered COP substrate.

Figure 5.14 shows the temperature dependence of the resistivity of ZnO thin film grown on β-Ga_2O_3 single crystal buffered COP substrate. The resistivity at RT was about 2.1×10^{-3} Ωcm. The increase in resistance with increasing temperature is semiconducting behavior, indicating that the ZnO thin film on the β-Ga_2O_3 seed layer did not have high carrier concentration to degenerate [23].

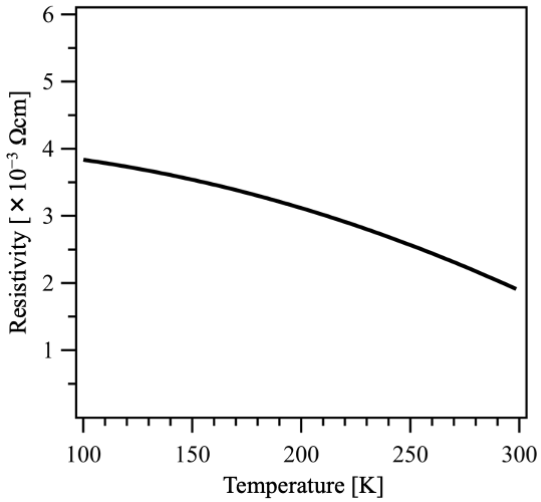

Figure 5.14 Temperature dependence of the resistivity of the ZnO thin film grown on β-Ga_2O_3 single crystal buffered COP substrate.

5.4 Summary

In this study, the effect of oxide buffer layer formation as a surface modification of polymer substrates on the crystal growth of ZnO thin films by PLD at RT was investigated. The crystal growth of c-axis oriented ZnO thin films enhanced on amorphous oxide buffers such as AlO_x and GaO_x, while scattered on randomly oriented and crystallized oxide buffers such as MgO and CeO_2. In particular, the orientation and crystallinity of ZnO films on polymer substrates were clearly improved by the formation of amorphous AlO_x buffer layers. The electrical resistivity of ZnO films grown on AlO_x buffered COP substrates was estimated from van der Pauw-type Hall effect measurements to be 2.6×10^{-3} Ω cm at RT, which was 34% smaller than that of films grown on untreated substrates. This is thought to be related to the improved crystallinity and orientation of the films grown on the pretreated COP substrates.

Epitaxial growth of ZnO thin films was obtained on β-Ga_2O_3 single-crystal buffered COP substrates. The epitaxial relationship between the ZnO thin film and the β-Ga_2O_3 single crystal buffer was estimated to be ZnO (0001) / β-Ga_2O_3 (100) with ZnO $[11\bar{2}0]$ ∥ β-Ga_2O_3 [010] and ZnO $[1\bar{1}00]$ ∥ β-Ga_2O_3 [001] from the phi-scan results of XRD. The FWHM value of the rocking-curve was about 1.7º, which was quite low despite grown on a polymer substrate. The resistivity near RT measured by the four-terminal method was 2.1×10^{-3} Ωcm, which is the lowest value on polymer substrate in this study.

Reference

[1] Z.L. Pei, X.B. Zhang, G.P. Zhang, J. Gong, C. Sun, R.F. Huang, L.S. Wen, Thin Solid Films, 497 (2006) 20–23.

[2] E. Fortunato, A. Gonçalves, V. Assunção, A. Marques, H. Águas, L. Pereira, I. Ferreira, R. Martins, Thin Solid Films, 442 (2003) 121–126.

[3] A. Bonbi, Chem. Rev., 52 (1953) 417–458.

[4] A. Miyake, T. Yamada, H. Makino, N. Yamamoto, T. Yamamoto, Thin Solid Films, 517 (2009) 3130–3133.

[5] A.N. Banerjee, C.K. Ghosh, K.K. Chattopadhyay, H. Minoura, A.K. Sarkar, A. Akiba, A. Kamiya, T. Endo, Thin Solid Films, 496 (2006) 112–116.

[6] H.-l. Shen, H. Zhang, L.-F. Lu, F. Jiang, C. Yang, Prog. Mater. Sci., 20 (2010) 44−48.

[7] E.G. Víllora, K. Shimamura, Y. Yoshikawa, K. Aoki, N. Ichinose, J. Cryst. Growth, 270 (2004) 420–426.

[8] A.H. Tavakoli, P.S. Maram, S.J. Widgeon, J. Rufner, K.v. Benthem, S. Ushakov, S. Sen, A. Navrotsky, J. Phys. Chem. C, 117 (2013) 17123−17130.

[9] A.A. Levchenko, G. Li, J. Boerio-Goates, B.F. Woodfield, A. Navrotsky, Chem. Mater., 18, (2006) 6324−6332.

[10] S. Mu, M. Wang, H. Peelaers, C.G.V.d. Walle, APL Mater. 8, (2020) 091105.

[11] A.L. Allred, J. Inorg. Nucl. Chem., 17 (1961) 215−221.

[12] A.L. Allred, E.G. Rochow, J. Inorg. Nucl. Chem., 5 (1958) 264−268.

[13] J.R. Williams, H. Furukawa, Y. Adachi, S. Grachev, E. Søndergård, N. Ohashi, Appl. Phys. Lett., 103, 042107 (2013).

[14] R. Heinholda, M.W. Allen, J. Mater. Res., 27 (2012) 2214-2219.

[15] K.-H. Bang, D.-K. Hwang, J.-M. Myoung, Appl. Surf. Sci., 207 (2003) 359–364.

[16] T. Matsumoto, M. Aoki, A. Kinoshita, T. Aono, Jpn. J. Appl. Phys. 13 (1974) 1578–1582.

[17] K. Shimamura, E.G. Víllora, K. Domen, K. Yui, K. Aoki, N. Ichinose, Jpn. J. Appl. Phys., 44, (2005) L7–L8.

[18] E.G. Víllora, K. Shimamura, K. Kitamura, K. Aoki T. Ujiie, Appl. Phys. Lett. 90, 234102 (2007).

[19] J. Zhang, B. Li, C. Xia, Q. Deng, J. Xu, G. Pei, F. Wu, Y. Wu, H. Shi, W. Xu, Z. Yang, J. Cryst. Growth, 296 (2006) 186–190.

[20] M. Yoshimoto, T. Maeda, T. Ohnishi, and H. Koinuma, O. Ishiyama, M. Shinohara, M. Kubo, R. Miura, A. Miyamoto, Appl. Phys. Lett. 67, (1995) 2615–2617.

[21] S.-M. Park, T. Ikegami, K. Ebihara, Thin Solid Films, 513 (2006) 90–94.

[22] V. Srikant, D. R. Clarke, J. Appl. Phys., 83 (1998) 5447–5451.
[23] S. Tricot, M. Nistor, E. Millon, C. Boulmer-Leborgne, N.B. Mandache, J. Perrière, W. Seiler, Surf. Sci. 604 (2010) 2024–2030.

Chapter 6

Effect of combinations of physical and chemical surface modifications of polymer substrates on crystal growth and properties of ZnO thin films

6.1 Introduction

The development of flexible devices will be advanced by synthesizing oxide thin films on polymer substrates with performance and quality equivalent to those of traditional oxide substrates [1]. From the viewpoint of device formation, the flatness of the substrate surface is an issue that directly affects not only performance improvement but also reliability [2]. In addition, the properties of oxide thin films are controlled by their orientation and crystallinity. Therefore, various techniques have been developed to obtain high orientation and crystallinity on polymer substrates for the purpose of producing high-performance oxide thin films. One is to increase the energy of the precursor or introduction of directional energy while maintaining the low temperature of the substrate, which has resulted in more highly crystalline thin films [3-5]. However, the most widely used technique is probably the cleaning and modification of the substrate surface and the formation of a buffer layer prior to the deposition of the oxide thin film [6-8]. Much work has been used epitaxial growth in case of film deposition on single crystal substrate and optimizing the matching of the crystal lattice by the introduction of buffers has lowered the temperature to obtain crystalline layers of oxide thin films [9]. However, this approach is not expected on amorphous substrates. Therefore, it would be desirable to adjust the flatness, uniformity, and chemical state of the substrate surface [10,11]. Temperature and effect on bulk performance must also be considered for polymer substrates [12]. There have been seldom reports on optimizing the morphology and chemical state of polymer substrate surfaces. It is possible that the much performance of oxide thin films on polymer substrates has not been realized. In this study, the effect of combination of surface modification techniques to obtain ZnO thin films with improved surface flatness, orientation, and crystallinity with the purpose of preparing high performance and quality oxide thin films on polymer substrates was investigated.

6.2 Experiment

In this study, the following two surface modification techniques were carried out as substrate surface modifications. cyclo-olefin polymer (COP) sheets (10 mm × 10 mm, 188 μm thick, ZF16-188, Zeon Corp.) were used as polymer substrates in this experiment. Firstly, The COP substrate was surface morphology modified by thermal nanoimprinting (X-300S, SCIVAX Corp.) using an atomically stepped sapphire mold at 180 °C for 5 min under 2.0 MPa pressure in vacuum purged four times with Ar (99.9999%) gas of 3×10^3 Pa. A glassy carbon susceptor (Tokai Carbon Co., Ltd.) with a low thermal conductivity was used to prevent rapid temperature changes [13]. In addition, an aluminum foil was inserted to improve the adhesion between the susceptor and the sample. The thermal nanoimprinting procedure consisted of pressurizing to 2.0 MPa at room temperature, raising and holding the temperature, cooling to room temperature, and finally removing the pressure [14].

Next, the oxide buffer layers were formed on the COP substrates by PLD using KrF excimer laser (λ= 248 nm, laser fluence= 1.2 Jcm^{-2}) with a sintered and single crystal target at RT without intentionally heating. The O_2 gas pressure was fixed at 1.0×10^{-3} Pa, and target-substrate distance was located at 5 cm.

Subsequently, The ZnO and Al-doped ZnO thin films were deposited on the untreated and surface-pretreated COP substrates via PLD using KrF excimer laser (λ = 248 nm, laser fluence = 1.0 Jcm^{-2} (pure-ZnO), 0.3 Jcm^{-2} (AZO)) with a sintered ZnO and Al (2 wt%) doped ZnO target at RT without intentionally heating. The O_2 gas pressure was fixed at 1.0×10^{-3} Pa, and target-substrate distance was located at 5 cm.

The surface morphology of the samples was observed by atomic force microscopy (AFM; Nanocute/Nanonavi, Hitachi High-Tech Science Corp.) operated in the contact mode. The crystal structure of the thin films was characterized by X-ray diffraction (XRD; RINT-2100V, Rigaku Corp.), and reciprocal space mapping using point focused Cukα x-rays on an XRD system (Smart Lab, Rigaku) equipped with a two-dimensional detector (PILATUS 100 K/R, Rigaku), reflection high energy electron diffraction (RHEED; Pascal Corp.). The optical transmittance of ZnO thin film on the COP sheet was measured using a UV/vis spectrophotometer (V-550, JASCO Corp.). The electrical properties of the samples were evaluated at RT in air under a magnetic field of 0.4 T using a van der Pauw-type Hall effect measurement system (HEMS-MD-S-30, Seinan Industry Co., Japan).

6.3 Results and discussion

6.3.1 Effect of nanoimprinting and oxide buffer insertion of polymer substrates on crystal growth of ZnO thin films

Figure 6.1 shows AFM images of ZnO films (*t*~40 nm) grown on stepped COP substrates (a) without buffer layer and (b) AlO_x buffer layer. The atomic step pattern reflecting the nanoimprinted COP substrate can be seen in both ZnO thin films. However, the ZnO thin film grown on the inserted AlO_x buffer layer shows a clear atomic step shape, while the only slight shapes can be seen in case of without oxide buffer layer.

The root-mean-square (RMS) surface roughness was 0.6 nm without the oxide buffer layer but was greatly reduced to about 0.2 nm on the AlO_x buffer layer. This RMS roughness value remained the same as that of the stepped COP substrate before ZnO thin film formation. This was thought to be due to the amorphous oxide buffer layer increased the surface free energy, resulting in dense nucleation and more accurately reflecting the COP substrate surface pattern [15].

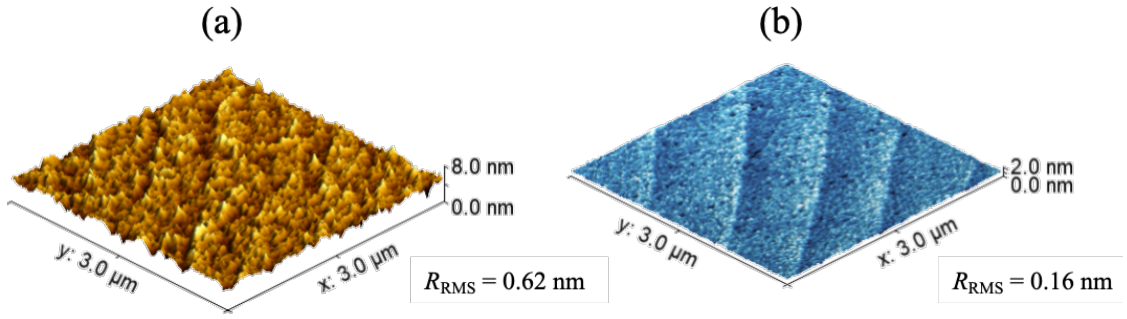

Figure 6.1 AFM images of ZnO films (*t*~40 nm) grown on on stepped COP substrates (a) without buffer layer and (b) with AlO_x buffer layer.

Figure 6.2 shows XRD 2θ/θ profiles and RHEED images of ZnO thin films grown on stepped COP substrates (a) without buffer layer and (b) with AlO_x buffer layer. ZnO *0002* diffraction was shown in both ZnO thin films, confirming c-axis oriented growth. However, the ZnO thin film grown on the AlO_x buffer layer showed a significant increase in the integrated intensity of the *0002* peak of the ZnO thin film and improved crystallinity, as in the case of simply AlO_x buffered film. The RHEED images also showed that the streak spots of the film on stepped COP without the buffer layer, but with the amorphous AlO_x buffer, the streak pattern, which indicates orientation, was more clearly defined. this

confirmed that the film was highly oriented. Maintain a distinct atomic step pattern of the COP substrate surface probably further improved mosaicism in the crystal growth of the ZnO thin film as shown in Figure 6.1. It was shown that ZnO thin films with high crystallinity and orientation as well as improved flatness can be obtained.

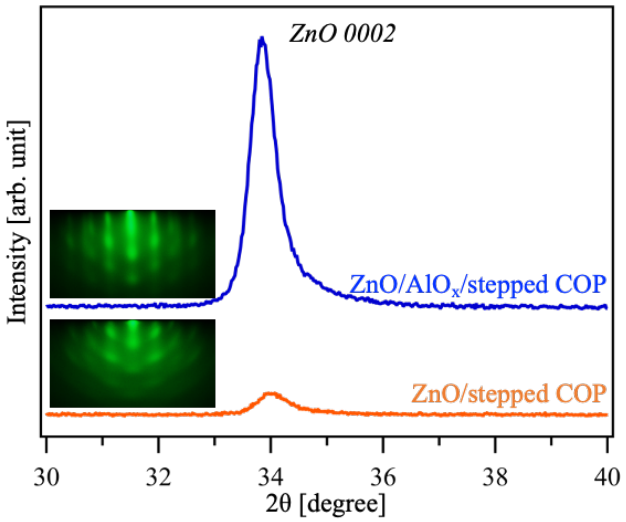

Figure 6.2 XRD 2θ/θ profiles of ZnO films grown on stepped COP substrates without buffer layer and with AlO_x buffer layer.

6.3.2 Effect of nanoimprinting and oxide buffer insertion of polymer substrates on crystal growth and propertied of Al-doped ZnO thin films

Figure 6.3 shows AFM images of Al-doped ZnO (AZO) thin films on (a) untreated and (b) stepped and AlO_x buffered COP substrates. As seen in Figure 6.3 (b), a slight atomic step pattern was observed even after about 200 nm thick of AZO thin film deposition. The RMS surface roughness was 1.3 nm for the AZO thin film on the untreated COP substrate, but decreased to about 0.5 nm for the AZO thin film on the stepped and AlO_x buffered COP substrate. This value is reduced to about 50% of that of a ZnO thin film with comparable conductivity [16].

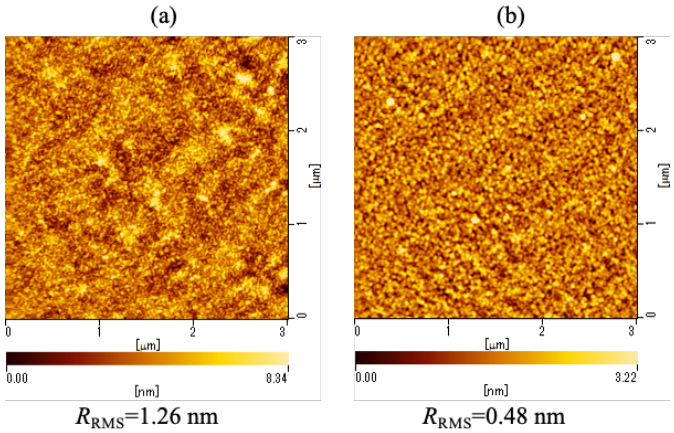

Figure 6.3 AFM images of AZO thin films (*t*~200 nm) grown on (a) untreated and (b) stepped and AlO_x buffered COP substrates.

Figure 6.4 shows the reciprocal space maps (RSMs) results of AZO thin films grown on (a) untreated, stepped and (b) MgO, (c) GaO_x, (d) SiO_x, and (e) AlO_x buffered COP substrates. Only diffraction peaks attributed to ZnO (0001) were observed in both AZO films, confirming c-axis oriented growth. However, as shown in chapter 5, only the insertion of random-oriented polycrystalline MgO buffer scattered AZO *0002* diffraction, while the GaO_x, SiO_x, and AlO_x buffers were amorphous with no respective peaks and improved mosaicism of AZO thin films. This is consistent with the result of the effect of crystallinity of the oxide buffer layer obtained in the pure-ZnO thin film.

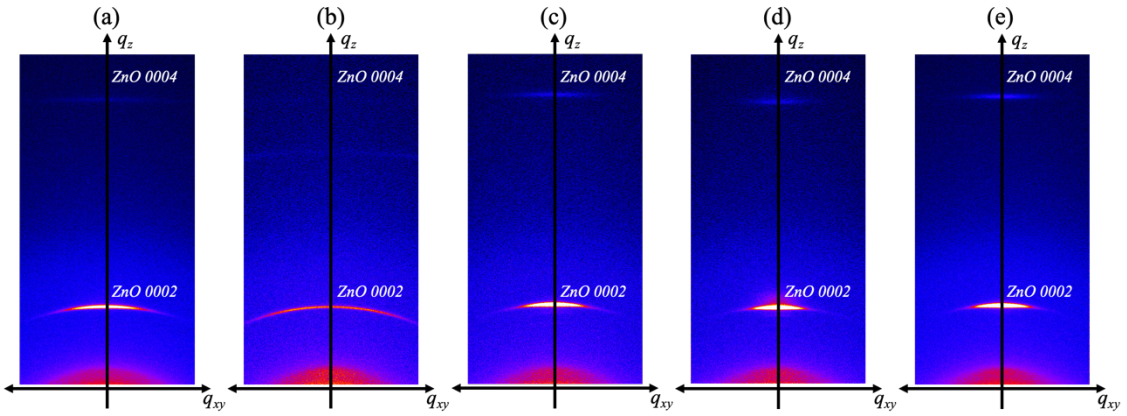

Figure 6.4 XRD reciprocal space maps of AZO thin films grown on (a) untreated, stepped and (b) MgO, (c) GaO_x, (d) SiO_x, and (e) AlO_x buffered COP substrates.

Table 6.1 shows analysis of XRD RSM results for *0002* diffraction of AZO thin films on untreated and respective combined surface-modified COP substrates of Figure 6.4. The FWHM of 2θ/ω-scan and the crystallite size derived from its results by Scherrer's formula were obtained [17]. The FWHM of rocking-curve was also obtained from the analysis of RSMs. The FWHM of the 2θ/ω-scan of the AZO thin film on the untreated COP substrate was 0.32º and the FWHM of the locking curve was 15.3º, and in case of oxide buffer layer insertion, the FWHM of the 2θ/ω-scan and rocking-curve were, 0.33º and 28.6º for MgO, 0.31º and 9.2º for GaO_x, 0.30º and 28.4º for SiO_x, and 0.29º and 7.7º for AlO_x, respectively. For AZO thin films at 200 nm thickness, the improvement of orientation of the AZO thin film was associated with improved crystallinity. This result was also confirmed by the degree of dispersion and contrast of AZO *0002* in each of the RSMs in Fig. 6.4. The crystallinity and orientation of the AZO thin film were most improved when AlO_x was used as a buffer layer.

The 2θ/ω-scan and rocking-curve FWHM values of combined surface-modified AZO thin film show the lowest level for a ZnO thin film on a polymer substrate. The FWHM value of the highly crystalline ZnO thin film grown on glass substrate at high temperature reported so far is about 0.1~0.2º, which is lower than the AZO thin films grown on surface-modified COP substrate in this study [18,19]. However, considering that the previous reported FWHM value of the highly crystalline ZnO thin film grown on the polymer substrate was about 0.35°, a thin film with sufficiently high crystallinity as an AZO thin film grown at room temperature was produced [20,21]. The previous reported

minimum FWHM value of the rocking curve reported on polymer substrates is less than 5° when 2D nanosheets are inserted, which is the next highest orientation [22].

Table 6.1 Results of XRD for *0002* diffraction of AZO thin films on untreated and respective surface-modified COP substrates.

Sample	2θ/ω FWHM [º]	Crystallite size [nm]	Rocking-curve FWHM [º]
On untreated COP	0.32	22.0	15.3
On stepped and MgO buffered COP	0.33	24.9	28.6
On stepped and GaO_x buffered COP	0.31	26.7	9.2
On stepped and SiO_x buffered COP	0.30	27.3	8.4
On stepped and AlO_x buffered COP	0.29	28.3	7.7

Table 6.2 shows electric properties of the ZnO thin films grown on untreated, stepped and MgO, GaO_x, SiO_x, and AlO_x buffered COP substrates estimated from the van der Pauw-type Hall effect measurements at RT. Resistivity was 4.0×10^{-4} Ωcm of AZO thin film grown on untreated COP substrates, increasing to 4.8×10^{-4} Ωcm with insertion of MgO buffers, but decreased to 4.0×10^{-4} Ωcm, 3.4×10^{-4} Ωcm, and 2.8×10^{-4} Ωcm, for insertion of GaO_x, SiO_x, and AlO_x buffers, respectively. This change in resistivity corresponded to the results of crystallinity and orientation shown in Fig. 6.4 and table 6.1. In particular, the AZO thin film on the stepped and AlOx-buffered COP substrate was about 30% lower than the film on the untreated COP substrate. The change in Hall mobility was about 10% less with the introduction of oxide buffer from the AZO thin film on the untreated COP substrate from the Hall effect measurements. On the other hand, the carrier concentration increased by about 60%, in case of the AlO_x buffer insertion from the AZO thin film on the untreated substrate, indicating that the change in resistivity is largely due to the effect of carrier concentration. The degree of Hall mobility decreases for films with larger carrier concentrations was suggested that the low Hall mobility despite the improved crystallinity in Table 6.1 was due to the increased effect of ion scattering caused by the increased carriers concentration. This resistivity was quite low level for a ZnO-based transparent conductive film on a polymer substrate. On the other

hand, since the lowest resistivity was not obtained despite the highest level of crystallinity as a ZnO-based thin film reported so far, further investigation of the amount of impurity doping and the oxygen atmosphere during film deposition [16,23,24].

Table 6.2 Electric properties of the ZnO thin films grown on untreated, stepped and MgO, GaO_x, SiO_x, and AlO_x buffered COP substrates estimated from the van der Pauw-type Hall effect measurements at RT.

Film sample	Resistivity [Ωcm]	Hall mobility [$cm^2V^{-1}s^{-1}$]	Carrier concentration [cm^{-3}]
On untreated COP	4.0×10^{-4}	22	6.9×10^{20}
On stepped and MgO buffered COP	4.8×10^{-4}	18	7.1×10^{20}
On stepped and GaO_x buffered COP	4.0×10^{-4}	22	8.6×10^{20}
On stepped and SiO_x buffered COP	3.4×10^{-4}	20	9.2×10^{20}
On stepped and AlO_x buffered COP	2.8×10^{-4}	20	1.1×10^{21}

The correlation between Hall mobility, crystallite size, rocking-curve FWHM, and carrier concentration was investigated to the relationship between crystal growth and electrical properties of AZO thin films on polymer substrate. Figure 6.5 shows relationship between XRD measurements (Table 6.1) and Hall effect measurements (Table 6.2). An increase in carrier concentration was observed as the degree of rocking curve of the AZO thin film decreased. This suggests that the improvement in the orientation of the AZO film improves the carrier concentration. No clear correlation to Hall mobility was found for the increase in crystallite size. This is thought to be due to the effect of ion scattering caused by the increase in carrier concentration in the AZO thin film on Hall mobility [25]. It is known that increased crystallinity improves Hall mobility, but the AZO thin film on the surface-modified COP substrate fabricated in this experiment shows significant changes in orientation and carrier concentration in addition to increased crystallinity. This suggested that the electrical resistivity may be mainly dominated by changes in carrier concentration.

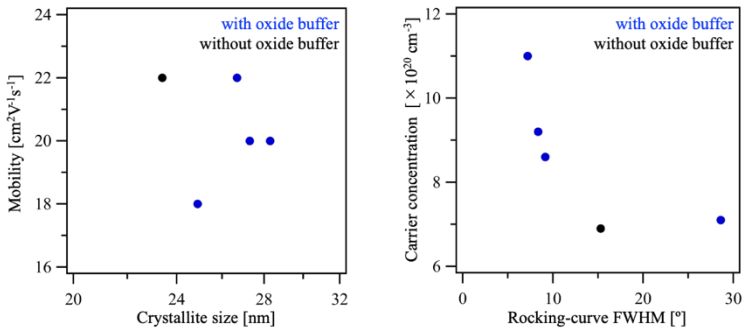

Figure 6.5 Relationship between results of XRD measurements and Hall effect measurements

Optical transmittance was measured in the UV and visible light range. Figure 6.6 shows the transmittance of ZnO thin films on stepped and AlO_x buffered COP substrates; the transmittance of the AZO thin film with AlO_x buffer was about 90% or higher in the visible light region. The high transmittance might be obtained due to the improved high crystallinity and orientation of the AZO thin film shown in Figure 6.4.

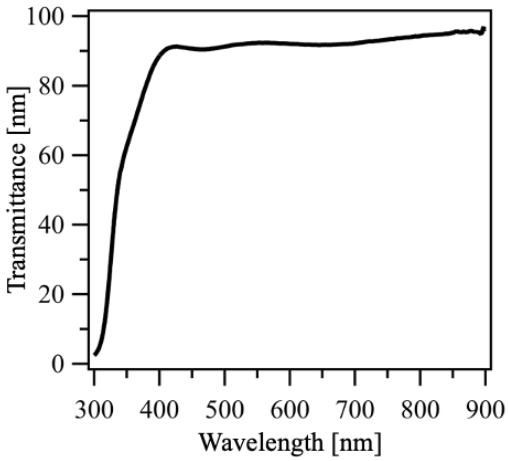

Figure 6.6 Transmittance of AZO thin films on stepped and AlO_x buffered COP substrate.

6.4 Summary

In this study, the effects of a combination of physical and chemical surface modifications as surface modification of polymer substrates on the crystal growth of ZnO thin films by PLD at RT was investigated. Nanoimprinting of atomic step pattern and deposition of oxide buffer were used as surface modifications. Atomic step pattern (t~40 nm) in the ZnO thin film were shown to be slight when no amorphous oxide buffer was inserted; when the AlO_x buffer was inserted, the patterns were clearly shown, and the flatness was improved. The insertion of the AlO_x buffer layer more clearly reflected the surface morphology of the COP substrate in the ZnO thin film. XRD measurements also showed that the AlO_x buffer had the same effect of promoting oriented crystal growth as the insertion of AlO_x buffer onto untreated COP substrate. An appropriate combination of physical and chemical surface modifications had a greater synergistic effect than if they were used alone.

Al-doped ZnO thin films (t~200 nm) were prepared for highly conductive ZnO films on polymer substrate. AZO thin film on stepped and AlO_x buffered COP substrate showed a slight atomic-step pattern and had improved flatness with a surface RMS roughness of about 0.5 nm in 3 μm^2. The crystallinity and orientation of the AZO films varied depending on the oxide buffer layer materials, with the AlO_x buffer showing the most improvement in crystal growth. The obtained resistivity was 2.8×10^{-4} Ωcm, which is low even on polymer substrates. The improvement in orientation corresponds to an increase in carrier concentration was suggested resulted by XRD and Hall-effect measurement. The transmittance of the AZO thin film was approximately 90% or higher in the visible light region.

Reference

[1] Y. Sun, J.A. Rogers, Adv. Mater., 19 (2007) 1897–1916.

[2] Y.-H. Tak, K.-B. Kim, H.-G. Park, K.-H. Lee, J.-R. Lee., Thin Solid Films 411 (2002) 12–16.

[3] T. Tsuchiya, T. Nakajima, Y. Uzawa, Chem. Eur. J., 26 (2020) 9261–9276.

[4] D. Kim, J.-Y. Leem, Sci. Rep., 11, 382 (2021).

[5] S. Yata, Y. Nakashima, T. Kobayashi, Thin Solid Films 445 (2003) 259–262.

[6] T. Liu, X. Fei, L. Hu, H. Zhang, Y. Li, S. Duo, Superlattices Microstruct., 83 (2015) 604–617.

[7] Y. Imanishi, M. Taguchi, K. Onisawa, Thin Solid Films, 518 (2010) 2945–2948.

[8] J. Nomoto, J. Oda, T. Miyata, T. Minami, Thin Solid Films, 519 (2010) 1587–1593.

[9] A. Sasaki, W. Hara, A. Matsuda, N. Tateda, S. Otaka, S. Akiba, K. Saito, T. Yodo, M. Yoshimoto, Appl. Phys. Lett., 86, 231911 (2005).

[10] J.Y. Lee, C.M. Shin, J.H. Heo, C.R. Kim, J.H. Park, T.M. Lee, H. Ryu, C.S. Son, B.C. Shin, W.J. Lee, Curr. Appl. Phys., 10 (2010) S290–S293.

[11] K. Hamada, T. Ogawa, H. Okumura, K.N. Ishihara, MRS Commun., 9 (2019) 697–701.

[12] C.-M. Chan, T.-M. Ko, H. Hiraoka, Surf. Sci. Rep., 24 (1996) 1–54.

[13] S. Yamada, H. Sato, Nature, 193 (1962) 261–262.

[14] T. Oga, S. Yamada, N. Kaneko, S. Kaneko, A. Matsuda, M. Yoshimoto, Jpn. J. Appl. Phys. 59, 128001 (2020).

[15] K.-H. Bang, D.-K. Hwang, J.-M. Myoung, Appl. Surf. Sci., 207 (2003) 359–364.

[16] J.-P. Kim, S.-A Lee, J.S. Bae, S.-K. Park, U.-C. Choi, C.-R. Cho, Thin Solid Films, 516 (2008) 5223–5226.

[17] B.D. Cullity, Elements of X-ray Diffraction, 2nd ed., Addison Wesley, Reading, MA, (1978) pp. 102.

[18] S.L. King, J.G.E. Gardeniers, I.W. Boyd, Appl. Surf. Sci., 96–98 (1996) 811–818.

[19] T. Yamada, A. Miyake, S. Kishimoto, H. Makino, N. Yamamoto, T. Yamamoto, Surf. Coat. Technol., 202 (2007) 973–976.

[20] M. Kim, J.-Y. Leem, J.-S. Son, J. Korean Phys. Soc., 68, (2016) 705–709.

[21] A. Miyake, T. Yamada, H. Makino, N. Yamamoto, T. Yamamoto, Thin Solid Films 517 (2009) 3130–3133.

[22] T. Shibata, T. Ohnishi, I. Sakaguchi, M. Osada, K. Takada, T. Kogure, T. Sasaki, J. Phys. Chem. C, 113 (2009) 19096–19101.

[23] J. Nomoto, H. Makino, T. Tsuchiya, T. Yamamoto, J. Appl. Phys., 128, 145303 (2020).
[24] V. Kumar, H C Swart, S Som, V. Kumar, A Yousif, A. Pandey, S K K Shaat, O M Ntwaeaborwa, Laser Phys., 24, 105704 (2014).
[25] T. Minami, Semicond. Sci. Technol., 20 (2005) S35–S44.

Chapter 7
General conclusions

In this thesis, the crystal growth and properties of ZnO thin films on surface-modified polymer substrates has been studied.

The objective of this thesis is to clarify the effect of physical and chemical surface modification of polymer substrates on the crystal growth of ZnO thin films on polymer substrates, which affects the crystallinity and orientation, and to verify the surface modifying conditions for the preparation of highly crystalline and oriented ZnO thin films to achieve high electrical and optical properties. The control of crystal growth of ZnO thin films grown by room temperature pulsed laser deposition using morphological and chemical surface pretreatment as a modification of polymer surfaces was investigated. In addition, crystal growth of ZnO thin films on polymer substrates pretreated with a combination of physical and chemical surface modification techniques was clarified, and methods for fabricating high-quality ZnO thin films on composite surface-modified polymer substrates were discussed. The results of this study can be summarized as follows.

In chapter 3, the crystal growth and properties of ZnO thin films grown on surface morphology improved polymer substrates was investigated. The ZnO thin films were grown by PLD at RT on a COP substrate with an ultra-flat surface on which an atomic step pattern of approximately 0.3 nm height was transcribed by thermal nanoimprinting (stepped COP substrate). The surface morphology of the ZnO thin film on the stepped COP substrate was flat with a root-means-square (RMS) roughness of 0.6 nm on a 3 μm square. The ZnO thin film grown on stepped COP substrates was (0001) oriented growth, with a slight crystallinity improvement and a clear orientation improvement. The growth of ZnO thin films on COP substrates was suggested c-axis oriented growth perpendicular to the substrate surface direction. A slight improvement in visible light transmittance and a decrease in resistivity of the ZnO thin film grown on stepped COP substrate was obtained.

In chapter 4, the crystal growth and properties of ZnO thin films grown on morphology-improved and chemical-changed COP substrates was investigated. The ZnO thin films were grown by PLD at RT on a COP substrate pretreated with a VUV-light irradiation. The surface morphology of the ZnO thin film on the VUV-light pretreated COP substrate was smooth with an RMS roughness of 0.6 nm on a 3 μm square. The ZnO thin film

grown on VUV-light-pretreated COP substrates was (0001) oriented growth, with a clear crystallinity and orientation improvement. The electrical resistivity of the ZnO thin film grown on the VUV-light-pretreated COP substrate was 40% smaller than that of the films grown on the untreated substrates, which might be related to the improvement of crystallinity of the film grown on the pretreated COP substrates.

In chapter 5, the crystal growth and properties of ZnO thin films grown on oxide buffered COP substrates was investigated. The ZnO thin films were grown by PLD at RT on a COP substrate with amorphous, polycrystal and single crystal buffer layer insertion. The surface morphology of the ZnO thin film on the amorphous AlO_x buffered COP substrate was slight unevenness with an RMS roughness of 0.7 nm on a 3 μm square. The crystal growth of c-axis oriented ZnO thin films enhanced on amorphous oxide buffers, while scattered on randomly oriented and crystallized oxide buffers. The ZnO thin film on β-Ga_2O_3 single-crystal buffered COP substrates was epitaxially grown. The electrical resistivity of the ZnO thin film grown on the AlO_x buffered COP substrate was 34% smaller than that of the films grown on the untreated substrates, and the resistivity of ZnO thin film grown on β-Ga_2O_3 single-crystal buffered COP substrate was 2.1×10^{-3} Ωcm, which is the lowest value on polymer substrate in this study.

In chapter 6, the crystal growth and properties of ZnO thin films grown on surface modified COP substrates with a combination of physical and chemical surface pretreatment was investigated. The ZnO thin films were grown by PLD at RT on a COP substrate with atomic step pattern formation and oxide buffer insertion. The surface morphology of the ZnO thin film on the stepped and AlO_x buffered COP substrate was a clear atomic step pattern with an RMS roughness of 0.2 nm on a 3 μm square. The ZnO thin film grown on stepped and AlO_x buffered COP substrates was (0001) oriented growth, with clear orientation and crystallinity improvement. The combination of physical and chemical surface modification has resulted in more effective crystal growth and planarity of ZnO thin films.

Highly conductive Al-doped ZnO (AZO) thin films were prepared to investigate their application to devices using the surface modification technique resulted in this study. The AZO thin films on stepped and AlO_x buffered COP substrates exhibited a slight atomic step pattern, with a surface RMS roughness of about 0.5 nm at 3 μm^2, a resistivity of 2.8×10^{-4} Ωcm, and a transmittance in the visible light region of about 90% or more. These were achieved by the growth of highly crystalline and oriented ZnO thin films on the surface-modified polymer substrate.

Through the results of the above chapters, the effects of various surface modifications of on polymer substrates on the crystal growth of ZnO thin films were clarified. As a result, the modification of the surface morphology of the polymer substrates contributes to the improvement of surface flatness and orientated crystal growth of ZnO thin films, and modification of the surface chemical state of the polymer substrate contributes to the improvement of crystallinity as well as orientation of the ZnO thin films were identified. It was also revealed that the crystallinity of the oxide buffer layer insertion onto the polymer substrate effects the oriented crystal growth and properties of the ZnO thin films. In addition, it was found that the combination of the surface modification technics of polymer substrate has a higher effect on the ZnO thin film and leads to prepare a high-quality ZnO thin films. This knowledge of the effect of surface modification of polymer substrates on the crystal growth and properties of ZnO thin films in this study provides an effective preparation method for the formation of devices using ZnO thin films on polymer substrates. The surface modification technique and the high quality ZnO thin films grown on it are expected to improve the of device performance on polymer substrate and contribute to further flexible device development.

This knowledge of the effect of surface modification of polymer substrates on the crystal growth and properties of ZnO thin films in this study are expected to improve the of device performance using ZnO thin films on polymer substrate and contribute to further flexible device development.

Accomplishments

Original Articles

[1] Original Articles directly related to Dr. thesis study

1. **T. Oga,** S. Yamada, N. Kaneko, S. Kaneko, A. Matsuda, M. Yoshimoto, “Fabrication of ultra-flat c-axis oriented ZnO thin films on atomically stepped cyclo-olefin polymer (COP) substrates by pulsed laser deposition at RT”, Jpn. J. Appl. Phys., **59**, 128001 (2020).
2. **T. Oga,** R. Kai, N. Kaneko, H. Miyazaki, S. Kaneko, A. Matsuda, M. Yoshimoto, “Crystallinity improvement of room-temperature PLD-deposited ZnO thin films on cyclo-olefin polymer substrates subject to surface-pretreatment with vacuum-UV-light irradiation”, J. Cryst. Growth, **603**, 127012 (2023).
3. **T. Oga**, S. Kaneko, A. Matsuda, M. Yoshimoto “Room-temperature fabrication of epitaxial ZnO thin films on polymer substrates coated with a seed layer of exfoliated β-Ga_2O_3 single-crystal thin sheets by pulsed laser deposition”. (Accepted for publication in J. Ceram. Soc, Japan, (2023)).

[2] Original Articles partly related to Dr. thesis study

4. H. Fukuta, G. Tan, **T. Oga**, A. Matsuda, M. Yoshimoto, K. Umezawa, "Surface structural analysis of CaF_2(111) using low-energy atom scattering spectroscopy". (Under review, submitted to J. Vac. Sci. Technol. A, (2022)).
5. Y. Maeda, N. Kaneko, **T. Oga**, S. Kaneko, A. Matsuda, M. Yoshimoto, “Formation of 0.3 nm-high atomic step and ultra-smooth terrace on PEDOT:PSS conducting polymer thin film surface by thermal nanoimprinting". (Under review, submitted to Microelectron. Eng., (2023)).
6. R. Kai, **T. Oga**, K. Watanabe, S. Kaneko, A. Matsuda, M. Yoshimoto, “Fabrication of highly-oriented β-Ga_2O_3 thin film on ZnO/AlO_x-buffered cyclo-olefin polymer substrate by excimer laser annealing at room temperature”. (Under review, submitted to Jpn. J. Appl. Phys., (2022)).

Presentation at international conference

1 **T. Oga**, K. Iwasa, S. Yamada, H. Morita, S. Kaneko, A. Matsuda, M. Yoshimoto, “Fabrication of UV-sensitive semiconductor thin films on ultra-flat polymer sheets with 0.3 nm-high atomic step-and-terrace surface”, 2019 Material Research Society Spring Meeting, Phoenix, Apr. 23, 2019.

2 **T. Oga**, H. Morita, S. Kaneko, A. Matsuda, M. Yoshimoto, “Orientation controlled room-temperature growth of ZnO (0001) thin films on atomic-step patterned flexible polymer substrates” Materials Research Meeting 2019, Yokohama. Dec. 13, 2019.

3 **T. Oga**, N, Kaneko, K. Kaneko, S. Kaneko, A. Matsuda, M. Yoshimoto, “Room-Temperature Growth of Ultra-Flat Transparent Conducting ZnO Thin Films on the Morphologically and Chemically Surface-Modified Polymer Substrates for Flexible Optoelectronics Devices” 2021 Material Research Society Fall Meeting, Virtual, Dec. 7, 2021.

4 **T. Oga**, N, Kaneko, S. Kaneko, A. Matsuda, M. Yoshimoto, “Room-temperature highly-oriented growth of ZnO thin films on surface modified cyclic olefin polymer substrates”, Materials Research Meeting 2021, Online, Dec. 14, 2021.

5 **T. Oga**, R. Kai, N. Kaneko, K. Kaneko, H. Miyazaki, S. Kaneko, A. Matsuda, M. Yoshimoto, 2022 Material Research Society Spring Meeting, “Fabrication of Highly-Oriented Wide-Bandgap Oxide Thin Films on the Surface-Modified Polymer Substrates by Room-Temperature UV Laser/Light Processes”, Virtual, May 23, 2022.

6 **T. Oga**, H. Miyazaki, S. Kaneko, A. Matsuda, M. Yoshimoto, “Influence of atomic-scale thermal-nanoimprint patterning and surface modification of the polymer substrate on growth of functional oxide thin films”, The 22nd International Conference on Nanoimprint and Nanoprint Technology (NNT 2022), Toyama, Oct. 6, 2022.

7 **T. Oga**, R. Kai, H. Miyazaki, S. Kaneko, A. Matsuda, M. Yoshimoto, “Lowering in resistivity and ultra-flattening of AZO thin films on cyclo-olefin polymer substrates via substrate-surface modification for flexible optoelectronics”, 2022 Material Research Society Fall Meeting, Virtual, Dec. 7, 2022.

Presentation at domestic conference

1 **大賀友瑛**, 森田公之, 池谷侑紀, 土嶺信男, 金子 智, 松田晃史, 吉本 護, 「紫外エキシマ光／レーザー照射による β-Ga_2O_3 薄膜の室温固相結晶化プロセスの検討」, 第 79 回 応用物理学会 秋季学術講演会 (The 79th JSAP Autumn Meeting), 名古屋国際会議場, 2018 年 9 月 18 日.

2 **大賀友瑛**, 岩佐健,山田志織,金子智, 松田 晃史, 吉本護,「酸化物半導体薄膜の成長および特性に及ぼすポリマー基板表面における原子レベルパターンの影響」, 第 66 回 応用物理学会 春季学術講演会 (The 66th JSAP Spring Meeting,), 東京工業大学大岡山キャンパス, 2019 年 3 月 11 日.

3 **大賀友瑛**, 大島淳史, 金子奈帆, 金子智, 松田晃史, 吉本護, 「エキシマ光プロセスを用いた超平坦ポリマー基板上での ZnO 薄膜の低温合成と高結晶配

向化」, 第 80 回 応用物理学会 秋季学術講演会(The 80th JSAP Autumn Meeting), 北海道大学札幌キャンパス, 2019 年 9 月 20 日.

4 **大賀友瑛**, 大島淳史, 金子奈帆, 金子智, 松田晃史, 吉本護, 「COP 基板におけるリピート熱ナノインプリントによる表面平坦化と導電性酸化物薄膜の堆積」, 第 67 回 応用物理学会 春季学術講演会 (The 67th JSAP Spring Meeting), 上智大学 四谷キャンパス, 2020 年 3 月.

5 **大賀友瑛**, 大島淳史, 金子奈帆, 金子智, 松田晃史, 吉本護, 「エキシマ光照射とナノインプリントによるポリマー基板表面の原子レベル超平坦化と ZnO 薄膜の結晶成長制御」, 日本セラミックス協会 2020 年年会 (The Ceramic Society of Japan Annual Meeting 2020), 2020 年 3 月.

6 **大賀友瑛**, 大島淳史, 金子奈帆, 金子智, 松田晃史, 吉本護, 「環状オレフィンポリマー基板表面への 172nm 真空紫外光照射が及ぼす ZnO 薄膜配向成長への影響」, 第 81 回 応用物理学会 秋季学術講演会 (The 81st JSAP Autumn Meeting), オンライン,2020 年 9 月 10 日.

7 **大賀友瑛**, 金子奈帆, 大島淳史, 金子智, 松田晃史, 吉本護, 「シクロオレフィンポリマー基板の真空紫外光処理による ZnO 薄膜結晶成長への影響」, MRM Forum 2020, オンライン, 2020 年 12 月 8 日.

8 **大賀友瑛**, 金子奈帆, 金子智, 松田晃史, 吉本護, 「環状オレフィンポリマー基板への種々の表面修飾が及ぼす ZnO 薄膜の配向結晶成長への影響」, 第 68 回 応用物理学会 春季学術講演会 (The 68th JSAP Spring Meeting), オンライン, 2021 年 3 月 19 日.

9 **大賀友瑛**, 金子奈帆, 金子智, 松田晃史, 吉本護, 「真空紫外光照射したシクロオレフィンポリマー基板上における酸化物薄膜の室温結晶成長」, 日本セラミックス協会 第 34 回秋季シンポジウム (The Ceramic Society of Japan The 34th Fall Meeting), オンライン, 2021 年 9 月 1 日.

10 **大賀友瑛**, 金子奈帆, 金子智, 松田晃史, 吉本護, 「表面修飾したシクロオレフィンポリマー基板上における ZnO 薄膜の高配向成長と特性評価」, 第 82 回 応用物理学会 秋季学術講演会 (The 82nd JSAP Autumn Meeting), オンライン, 2021 年 9 月 12 日.

11 **大賀友瑛**, 宮﨑尚, 金子智, 松田晃史, 吉本護, 「へき開した β-Ga_2O_3 (100)をシード層としたポリマー基板上での機能性酸化物薄膜のエピタキシャル成長”, 日本セラミックス協会 2022 年年会 (The Ceramic Society of Japan Annual Meeting 2022), オンライン, 2022 年 3 月 10 日.

12 **大賀友瑛**, 宮﨑尚, 金子智, 松田晃史, 吉本護, 「β-Ga_2O_3 単結晶へき開シード層を用いたポリマー基板上 ZnO 薄膜のエピタキシャル成長」, 第 69 回 応用物理学会 春季学術講演会 (The 69th JSAP Spring Meeting, 2022), オンライ

ン, 2022 年 3 月 25 日.

13 **大賀友瑛**, 宮﨑尚, 金子智, 松田晃史, 吉本護, 「シクロオレフィンポリマー基板上 ZnO 薄膜の低温 PLD 結晶成長に与える物理・化学的な基板表面修飾の効果」, 日本セラミックス協会 第 35 回秋季シンポジウム (The Ceramic Society of Japan The 35th Fall Meeting), 徳島大学常三島キャンパス, 2022 年 9 月 14 日.

14 **大賀友瑛**, 宮﨑尚, 金子智, 松田晃史, 吉本護, 「シクロオレフィンポリマー基板への表面修飾が AZO 薄膜の電気特性に与える影響」, 第 83 回 応用物理学会 秋季学術講演会(The 83rd JSAP Autumn Meeting), 東北大学川内キャンパス, 2022 年 9 月 23 日.

Award

1. 日本セラミックス協会 2022 年年会
   優秀ポスター発表賞 優秀賞
   大賀友瑛, 宮﨑尚, 金子智, 松田晃史, 吉本護,「へき開した β-Ga_2O_3 (100)をシード層としたポリマー基板上での機能性酸化物薄膜のエピタキシャル成長」

Acknowledgements

The present thesis has been carried out at the Department of Materials Science and Engineering, School of Materials and Chemical Technology, at Tokyo Institute of Technology under the direction of Prof. Mamoru Yoshimoto. I would like to express my gratitude for the many knowledgeable and attentive advice I received at all times. I would like to express my sincere gratitude to Associate Professor Akifumi Matsuda for not only his guidance on materials science but also his detailed technical training and advice, which enabled me to steadily advance my research.

I would also like to acknowledge with appreciation to Prof. Hiroshi Funakubo, Prof. Yutaka Majima, and Associate Prof. Hiroyuki Wada for not only serving as judging this thesis but also for their thoughtful guidance and support.

I would like to appreciate Dr. Satoru Kaneko of Kanagawa Institute of Industrial Science and Technology, Assistant Prof. Hisashi Miyazaki of National Defense Academy for their collaboration and helpful advice and support.

I would like to thank my co-workers of Yoshimoto-Matsuda laboratory, Ms. Naho Kaneko, Ms. Shiori Yamada, and Mr. Ryoya Kai, Mr. Yuki Ikea, Mr. Ken Iwasa, Mr. Shoyo Ito, Mr. Hiroyuki Morita, Mr. Subaru Nakanishi, Mr. Yoshiki Horimatsu, Mr. Atsushi Oshima, Mr. Yoshiharu Shinozaki, Mr. Takumi Matsushima, Mr. Takahiro Ikuta, Mr. Kenta Kaneko, Mr. Kazuki Watanabe, Mr. Shohei Hisatomi, Mr. Yuki Goto, Mr. Hiroki Shoji, Mr. Yuto Maeda, Ms. Ruka Umemoto, Mr, Itsuki Osawa, Mr. Reo, Kato, Ms. Yuka Shimada, Mr. Takumi Numata, Mr. Kazuya Kawamura, Mr. Yuchi Qiao, for their collaboration and many helpful suggestions and support in this thesis.

Finally, I would like to express my gratitude to my wife, Sayaka and sons, Takuma and Shoya for their warm support.

March 2023

Tomoaki Oga